Studies of superfluid ^{3}He confined to a submicron slab geometry

Antonio D. Córcoles

A Thesis submitted for the degree of Doctor of Philosophy

Royal Holloway

University of London

February 2006

To Nairi, for she likes to write half of my dedicatories.

...And to the beloved memory of my mother.

Abstract

The phase diagram of superfluid ^{3}He is predicted to be modified when confined to a regular geometry of size comparable to the superfluid coherence length. This thesis addresses the problem of the effect of such a small geometry on the order parameter of the superfluid. The samples are probed by two methods: Nuclear Magnetic Resonance and a Torsional Oscillator.

Nuclear Magnetic Resonance provides information about the spin dynamics of the system. This information can be used to identify the superfluid phases. The damping and frequency change of the torsion pendulum determine the hydrodynamic response of the fluid and they can be used to identify superfluidity and measure the superfluid density. The bulk anisotropy of the superfluid density could potentially help to identify the A-phase, although information sufficient to unambiguously determine the particular superfluid phase from the torsional oscillator is probably not possible in our experiment.

The NMR experiment involved the construction of a high sensitivity SQUID spectrometer which allowed the observation of samples of the order of 1×10^{17} spins. We observed superfluidity in a variety of samples. The superfluid phases were identified as A- and B-phases in small droplets distributed over the experimental cell. These droplets were formed due to imperfect annealing of the samples. For a 3 μm thick slab we observed a strongly supercooled A-phase at temperatures as low as

0.38 mK. This A-phase suddenly underwent a transition into B-phase after a period of ∼20 hours independently of the temperature to which it had been supercooled.

With the torsional oscillator we could see superfluidity in a film of nominal thickness of 143 nm. The dependence of the superfluid density on temperature agreed with most of the previous work, theoretical and experimental alike. It also showed remarkable similarities with other disordered systems like superfluid ^{3}He in aerogel, although these similarities were not quantitative.

Acknowledgements

I am indebted in one way or another to all of the following persons.

Professor John Saunders, the best supervisor one could probably get at this side of the Orion Nebula, a paradigm of researcher, a physicists' physicist. Dr. Andrew Casey, who worked with me all along this research and enlightened me with his wisdom about the nitty-gritty of low temperature techniques. Professor Brian Cowan, whose love for Physics was certainly inspirational. Professor Jeevak Parpia, who designed the torsional oscillator described in this thesis. I benefited enormously from the discussions with him. Dr. Chris Lusher, who shared a big part of the work on the NMR spectrometer and a little part of Schubert's Fantasy Op. 103 in f minor for piano four hands. Dr. Jan Nyéki, always ready to help, always full of experience, always interested in my athletic performances. Dr. Phil Glasson, who admires Richard Feynman almost as much as me, enjoys Physics almost as much as me and whose laughing is almost as contagious as mine. Dr. Tom Crane possesses all the knowledge a man could get about computers and then some. That has been a lifesaver on more than one occasion. Dr. Roch Schanen is probably the only human being I would perform an experiment on. He is also the best of the friends. Dr. Manuel Brando dared to jog with me on a couple of occasions and, obviously, outperformed me. Alan Betts, a man capable of fixing any device in this world which has anything to do with Ohm's Law. Francis Greenough supplied liquid ^{4}He with

outstanding competence. Howard Moore kept informing me about piano recitals on campus and, although I never attended one, I am grateful to him for such a first hand information. Dave Bosworth machined the pieces of the experimental cells and gave me a reason to smile every morning. Sheila Wilson is surely the definition of an effective secretary and her ability to manage bureaucracy is sometimes beyond my understanding. On a more personal level I have to mention Dennis Moroni, very close to me during my postgraduate years. Too close sometimes, actually. Dr. Rainer Körber, the perfect flatmate, the perfect workmate. Michael Neumann not only has the fastest metabolism known to man, but also the rare ability of discerning when his words are not as beautiful as silence, a virtue I urgently need to master myself. Alfonso Gracia, who knows everything about me and still loves me. Consuelo Sedano, my stepmother, who provided me with an education performing miracles every other day. Antonio Córcoles, Sr, the gene donor. Ana Fe González, my beloved mother. The light that shines with double intensity lasts half the time. She gave me enough love in five years to fill several lifetimes. And, finally, Nairi Grigorian, a Venus come to earth, my dreams turned reality, the best piano player since Franz Liszt and the only woman crazy enough to agree to marry me. Her love, understanding and support are, without a trace of doubt, my most valued treasured in this life. I love you, sweetheart.

Contents

List of Figures

List of Tables

Prelude

Motivations for this experiment

Physics is like sex: sure, it may give some practical results, but that's not why we do it.

Richard P. Feynman

Following the formulation of the BCS theory by Bardeen, Cooper and Schrieffer [1] in 1957, it was first suggested by Lev Pitaevski [2] that a BCS-like pairing into an ordered state could take place in liquid ^{3}He in the same way it happened in superconductors. The predicted temperature at which the transition should take place was of the order of 100 mK. Nothing was observed once that temperature was reached. From then on, theoreticians kept discovering new reasons by which the transition should be found at lower temperatures and the experimentalists kept seeing "nothing" when going that cold. Of course, the main benefit low temperature

physics got out of this race was a dramatic improvement in the cooling techniques of the time.

Then, in 1964, Vasily Peshkov [3] observed an anomaly in the heat capacity of ^{3}He at 5 mK and claimed to have seen the so yearned-for superfluid transition. It was at the Eighth International Low Temperature Physics Symposium in Columbus, Ohio, where Peshkov presented the previously announced "discovery". Following his presentation, John Wheatley stood up and pointed out several fatal flaws in the experiment. He had good reasons to disbelieve Peshkov's results: he had done experiments down to lower temperatures, he was sure of his temperature scale and he knew he had not seen superfluidity in ^{3}He at those temperatures. Although Wheatley was right about Peshkov's mistakes, he failed to identify the superfluid signature while making measurements below the actual transition temperature.

Finally, early in 1972, Osheroff, Richardson and Lee [4] discovered the transition while doing compressional adiabatic cooling in a Pomeranchuk cell at Cornell. That discovery constituted a major milestone in the theoretical and experimental development of low temperature physics. It opened a plethora of hitherto unexpected possibilities and incentives to deeply explore the new system. Nearly all branches of physics were dramatically affected by the discovery. Suddenly, numerous laboratories around the world turned their attention and efforts towards the new system. The phase diagram of superfluid ^{3}He was rapidly mapped out and soon physicists were looking for new properties of superfluid ^{3}He.

As it usually happens in low temperature physics, theories were ahead of experiments and there were theoretical studies about superfluid ^{3}He in confined geometries already in the mid seventies [5]. The study of vortices in ^{3}He or, more recently, the effect of disordered environments like aerogel on superfluidity also attracted the attention of the scientific community towards the light isotope of helium.

What is superfluid ^{3}He good for? A very embarrassing question. Because the answer is, at least in first order approximation, "Nothing". This only means that ^{3}He is not good for anything *directly*, but it is extremely good for many things indirectly. Apart from being an impressively remarkable system itself, ^{3}He is the most sophisticated physical system of which we can claim detailed quantitative understanding (i.e. textures, orientational dynamics, topological singularities...). It is useful in the study of turbulence, it has interesting analogies with particle physics and cosmology and, probably most important, it offers the possibility of displaying parity violation for the first time in a macroscopic state.

Regarding ^{3}He in confined geometries, size effects give rise to very interesting questions. The relevant length for superfluid ^{3}He is its coherence length (or, roughly speaking, the smallest distance over which the superfluid wave function is allowed to vary). We can regard the (pressure dependent) size of a Cooper pair (see Chapter 2) as the zero temperature value of the coherence length. This size (72 nm at zero temperature and zero pressure) is extremely large compared with the coherence length of superfluid ^{4}He (1 Å). This makes any ^{4}He sample of these dimensions essentially bulk-like[1] , whereas there is the potential of experimentally reaching these length scales in ^{3}He.

A sufficiently confined ^{3}He sample could provide a model for two dimensional superfluidity with an unconventional p-wave symmetry. Amongst the potential physics suggested for such systems we could highlight the possibility of a 2-D Kosterlitz-Thouless transition [6], the relationship with d-wave superconductors [7], [8] and ^{3}He in aerogel [9].

Recently, the question has arisen about the role that superfluid ^{3}He films could

[1] Although a monolayer of ^{4}He could exhibit superfluidity in a transition described by the Kosterlitz-Thouless theory [6]

have in understanding charged rotating black holes [10], event horizons for relativistic fermionic quasiparticles and Hawking radiation [11] and black hole formation models [12].

Chapter 1

Introduction

Discovery consists of seeing what everybody has seen and thinking what nobody has thought.

Albert von Szent-Györgyi.

^{3}He is, undoubtedly, one of the richest systems with which to do experimental physics. Not only is it the most complex material we can approach with the support of a successful theory, but also it has connections with almost any branch of modern theoretical physics. ^{3}He combines the complexities of liquid-crystal anisotropy and superfluid behaviour and it is also the first magnetic superfluid known to science. As shown in Figure 1.1, ^{3}He in bulk can exhibit superfluidity below 3 mK. The complex structure of the order parameter makes the superfluid phase diagram extremely rich, with two main superfluid states at zero magnetic field in bulk and several other phases which are stable in non-zero magnetic field or under conditions of confinement.

At low pressures and low temperatures, superfluid ^{3}He is found in the Balian-

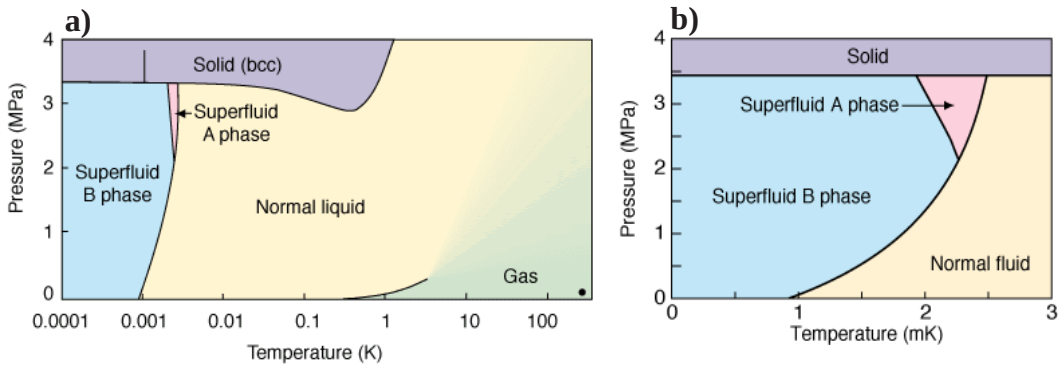

Figure 1.1: The phase diagram of bulk ^{3}He in absence of a magnetic field. Figures from the Low Temperature Group at Helsinki University of Technology.

Werthamer (BW) state [13] and is called ^{3}He-B. At high enough pressures or in the presence of a magnetic field, a different superfluid state can be stabilized over a narrow region of the phase diagram through strong coupling effects. This state corresponds to the Anderson, Brinkman and Morel state (ABM) [14], [15] and is called ^{3}He-A.

Although the bulk phase diagram of ^{3}He has been known for a number of years [16], [17] there is still a great deal of knowledge to be acquired about the effects of confinement and low dimensionality in this system.

The purpose of this thesis is to provide new insights into the understanding of the physics of confined anisotropic superfluids in general and of confined superfluid ^{3}He in particular by using two powerful and technically demanding experimental tech-

niques: Nuclear Magnetic Resonance, which explores the magnetic properties of the superfluid and the Torsional Oscillator, which probes its hydrodynamic properties.

The work is organized as follows:

Chapter 2 discusses the physics of superfluid ^{3}He from the point of view of both the BCS and the Ginzburg-Landau theories and gives an account of previous experiments and theories on superfluid ^{3}He in restricted geometries.

Chapter 3 introduces the principles of Nuclear Magnetic Resonance and DC SQUIDs. This is followed by a description of the experimental setup and method of operation and a review of the design, construction and assembly of the experimental cell. Finally, we present our results and compare them with previous experiments and theoretical predictions.

Chapter 4 is devoted to the Torsional Oscillator experiment. The design of the oscillator is presented, followed by details of the experimental cell. We show results from the normal liquid which help to understand the path that finally led to the design of our current cell. Then we present the superfluid results, again contrasting them with other flow experiments in similar systems and previous theories.

Chapter 5 summarizes the work and provides possible directions for future experiments on confined superfluid ^{3}He.

The cryogenic apparatus is described in Appendix A, along with the thermometry. Appendix B provides a brief guide to the data analysis techniques used in these experiments.

Chapter 2

Confined superfluid ^{3}He

Your theory is crazy, but it's not crazy enough to be true.

Niels Bohr.

Liquid ^{3}He above 1 K can be described nearly in terms of a dense classical gas, with significant corrections to the ideal gas behaviour arising from the quantum virial coefficients. Between about 100 mK and 3 mK, however, it behaves very like a weakly interacting degenerate Fermi gas (specific heat proportional to T, spin susceptibility temperature independent and viscosity proportional to T^{-2}, for instance). This is at first sight rather puzzling, since one would expect the atoms to be strongly interacting due to the large hard-core radius, comparable to the mean interatomic spacing. Landau's Fermi liquid theory [18] takes this into account, describing the system in terms of weakly interacting quasiparticles, and also reproduces the experimental observations. Below about 3 mK, and depending on pressure, ^{3}He exhibits superfluidity. The superfluid phases of ^{3}He are usually described in terms of the microscopic "weak coupling" BCS theory [1] applied to anisotropic supercon-

ductors and the Ginzburg-Landau phenomenological theory of second order phase transitions [19]. In this Chapter, we give a brief account of both approaches. An extensive study of these theories and their application to ^{3}He can be found elsewhere [20]. The second part of the Chapter deals with ^{3}He in confined planar geometries. We discuss the most important theoretical studies on the subject and present the experiments that have been done in the system up to this date.

2.1 The microscopic BCS theory applied to superfluid ^{3}He

2.1.1 Spin singlet pairing

The core of the BCS theory of superconductivity states that two identical Fermi particles with momentum $\hbar k$ and $\hbar k'$ near the Fermi surface and in the presence of a filled Fermi sea can interact through some potential in such a way that the total energy of the final state for these two particles would be less than twice the Fermi energy. The bound state formed by the two particles as a result of that interaction is called a *Cooper pair*. The potential used by Bardeen *et al.* to describe the formation of Cooper pairs is the following:

$$V_{\mathrm{kk}'} = \begin{cases} -V & \text{for } k_{\mathrm{F}} - \Delta k \leq k, k' \leq k_{\mathrm{F}} + \Delta k, \\ 0 & \text{otherwise} \end{cases} \tag{2.1}$$

where $\Delta k \ll k_{\mathrm{F}}$ is assumed. Only particles within a narrow shell near the Fermi surface would be affected by this interaction, since particles well inside the Fermi sphere would not have, within a small range of energies, empty levels available

to scatter into. The other fundamental ingredient in the BCS theory, apart from Equation 2.1, is the assumption that the Fermi surface is spherical in shape.

Now, one could construct the system wave function not by referring to *pair of particles*, but to *pairs of single-particle states* ($\mathbf{k}\uparrow, -\mathbf{k}\downarrow$) corresponding to spin singlet pairing. At zero temperature each state ($\mathbf{k}\uparrow, -\mathbf{k}\downarrow$) is either full or empty. We will use $|0,0>$ to refer to an unoccupied pair and $|1,1>$ to refer to an occupied one. The system wave function can be written as

$$\Phi = \prod_{\mathrm{k}} \Psi_{\mathrm{k}} \tag{2.2}$$

where

$$\Psi_{\mathrm{k}} = u_{\mathrm{k}}^{*}|0,0> + v_{\mathrm{k}}|1,1> \tag{2.3}$$

$|u_{\mathrm{k}}|^2$ is the probability that the pair ($\mathbf{k}\uparrow, -\mathbf{k}\downarrow$)is unoccupied and $|v_{\mathrm{k}}|^2$ is the probability that it is occupied. At $T = 0$ all the energy level below the Fermi surface are occupied and, therefore,

$$u_{\mathrm{k}} = 0 \quad \text{and} \quad v_{\mathrm{k}} = 1 \quad \text{for} \quad |\mathbf{k}| < k_{\mathrm{F}}$$

$$u_{\mathrm{k}} = 1 \quad \text{and} \quad v_{\mathrm{k}} = 0 \quad \text{for} \quad |\mathbf{k}| > k_{\mathrm{F}}$$

Plus, normalization requires

$$|u_{\mathrm{k}}|^2 + |v_{\mathrm{k}}|^2 = 1$$

The solutions of this system can be obtained by using a variational method. It is necessary, first, to write an expression for the Hamiltonian. For the kinetic energy we simply have

$$< \Phi|K - \mu N|\Phi >= \sum_{\mathrm{k}} 2\epsilon_{\mathrm{k}}|v_{\mathrm{k}}|^2 \tag{2.4}$$

where K is the kinetic energy operator, N is the number of particles, μ is the chemical potential and ϵ_{k} is the energy of *one* particle (hence the factor 2). The term μN is a constraint introduced due to the fact that we are not working under a constant number of particles. A superposition of states containing different numbers of particles might seem unrealistic, but one needs to bear in mind that the number of particles and the phase of the wave function are conjugate variables and, therefore, there exists an uncertainty relationship.

Now we account for the potential energy part of the Hamiltonian. The required expression is:

$$< \Phi|V|\Phi >= \sum_{\mathrm{k,k'}} V_{\mathrm{k,k'}} u_{\mathrm{k}} v^*_{\mathrm{k'}} u^*_{\mathrm{k'}} v_{\mathrm{k}} \tag{2.5}$$

because when the pair $(\mathbf{k}\uparrow, -\mathbf{k}\downarrow)$ scatters into $(\mathbf{k'}\uparrow, -\mathbf{k'}\downarrow)$, not only the state $(\mathbf{k}\uparrow, -\mathbf{k}\downarrow)$ has to be initially full (amplitude v_{k}) but also the state $(\mathrm{k'}\uparrow, -\mathbf{k'}\downarrow)$ has to be empty (amplitude $u^*_{\mathrm{k'}}$).

The next step is to minimize the complete expectation value with respect to variations in the occupation probabilities. Defining

$$\Delta_{\mathrm{k}} = \sum_{\mathrm{k'}} V_{\mathrm{k,k'}} u_{\mathrm{k'}} v_{\mathrm{k'}} \tag{2.6}$$

we obtain after some algebra the well-known expression for the ground state BCS energy gap:

$$\Delta_{\mathrm{k}} = -\sum_{\mathrm{k'}} V_{\mathrm{k,k'}} \frac{\Delta_{\mathrm{k'}}}{2E_{\mathrm{k'}}} \tag{2.7}$$

where $E^2_{\mathrm{k}} = \epsilon^2_{\mathrm{k}} + |\Delta_{\mathrm{k}}|^2$.

If we want to extend the present treatment to finite temperatures, we must allow some other states into the wave function, namely, the "broken pair" states $|1,0>$ and $|0,1>$ (which account for $(\mathbf{k}\uparrow)$ occupied and $(-\mathbf{k}\downarrow)$ unoccupied, etc.). We

obtain then the final general expression for the BCS gap equation:

$$\Delta_{\mathrm{k}} = -\sum_{\mathrm{k}'} V_{\mathrm{k},\mathrm{k}'} \frac{\Delta_{\mathrm{k}'}}{2E_{\mathrm{k}'}} \tanh \frac{E_{\mathrm{k}'}}{2k_{\mathrm{B}}T} \tag{2.8}$$

One should note here that the gap equation defines only an extremum of the free energy. In the case of superconductors this is not a problem since there is only one extremum which is also a minimum. But for $l \neq 0$ the gap equation provides several solutions, some of them not even an extremum but a saddle point. The energy E_{k} can be shown to be the energy of an elementary excitation [20].

2.1.2 Spin triplet pairing

The effective interaction in liquid ^{3}He is rather complicated due to the range of the hard-core repulsion potential, which is comparable to the interatomic distance. The s-wave pairing that takes place in superconductors, with the electrons forming pairs with relative angular momentum zero, is not possible in ^{3}He due to the strong hard-core repulsion. The spatial wave function of a Cooper pair in ^{3}He has the structure of a p-orbital, with total angular momentum $L = 1$, and it is, consequently, antisymmetric under the interchange of the atoms. Due to the fermionic nature of the ^{3}He quasiparticles, the total wave function needs to be antisymmetric, which implies a symmetric spin part of the total wave function. Thus, ^{3}He shows spin triplet ($S = 1$) pairing in the superfluid phases, the spin subspaces being $|\uparrow\uparrow>$, $|\downarrow\downarrow>$ and $|\uparrow\downarrow + \downarrow\uparrow>$. Whereas for the $L = 0$ case we had a wave function of the form

$$\Psi(k) = \Psi_{\uparrow\downarrow}(k)(|\uparrow\downarrow - \downarrow\uparrow>) \tag{2.9}$$

we have to write now

$$\Psi(k) = \Psi_{\uparrow\uparrow}(k)|\uparrow\uparrow> + \Psi_{\downarrow\downarrow}(k)|\downarrow\downarrow> + \Psi_{\uparrow\downarrow}(k)(|\uparrow\downarrow + \downarrow\uparrow>) \tag{2.10}$$

Note that these wave functions have not been normalized. The BCS gap could now have different values for different spin subspaces. We have to define

$$\Delta(k) = \begin{pmatrix} \Psi_{\uparrow\uparrow}(k) & \Psi_{\uparrow\downarrow}(k) \\ \Psi_{\downarrow\uparrow}(k) & \Psi_{\downarrow\downarrow}(k) \end{pmatrix} \tag{2.11}$$

Each of the above matrix elements follows the gap Equation 2.8. This is not, however, the most convenient way to express the pairing. We can introduce [13] a vector representation with Leggett's notation

$$\mathbf{d}(k) = \frac{1}{2} \quad i\sum_{\alpha\beta}(\sigma_{\mathrm{y}}\boldsymbol{\sigma})_{\alpha\beta}\Psi_{\alpha\beta}(k) \tag{2.12}$$

where σ's are the Pauli matrices and the subindexes run over the spin states $\uparrow$ and $\downarrow$. We can invert the above expression and obtain

$$\Delta(k) = \begin{pmatrix} -d_{\mathrm{x}}(k) + id_{\mathrm{y}}(k) & d_{\mathrm{z}}(k) \\ d_{\mathrm{z}}(k) & d_{\mathrm{x}}(k) + id_{\mathrm{y}}(k) \end{pmatrix} \tag{2.13}$$

It is possible to obtain further insight into the physical interpretation of the $\mathbf{d}$ vector by calculating the value of the square of the gap $\Delta\Delta^+$.

$$\Delta\Delta^+ = (\mathbf{d}\cdot\mathbf{d}^*)I + i\boldsymbol{\sigma}\cdot(\mathbf{d}\times\mathbf{d}^*) \tag{2.14}$$

Let us define a *unitary state* as one for which $\Delta\Delta^+$ is proportional to the unit matrix. It follows that, for a unitary state, $\mathbf{d} \times \mathbf{d}^* = \mathbf{0}$ or, in other words, $\mathbf{d}$ is a real vector and the excitation energy E_k is a number rather than a matrix. It can also be shown [21] that $\mathbf{d} \cdot \mathbf{S} = 0$, so the modulus of $\mathbf{d}$ tells us the magnitude of the gap for an unitary state and its direction is the direction of zero spin projection.

We will define yet another quantity. If we express the $\mathbf{d}$ vector as a function of the $\mathbf{k}$ vector,

$$d_\mathrm{i}(\mathbf{k}) = \sum_\rho A_{\mathrm{i}\rho} k_\rho \tag{2.15}$$

we obtain a 3×3 complex matrix $A_{\mathrm{i}\rho}$ and whereas in the case of superconductors we had only two degrees of freedom (the amplitude and the phase of the wave function), we have now 18. Fortunately, they are not all independent in the stable phases, so we will not need to deal with intractable systems. The A matrix generates the $\mathbf{d}$ vector from $\mathbf{k}$, the position on the Fermi surface, and, therefore, can be used to describe the pairing in superfluid ^{3}He.

2.1.3 The B-phase

The B-phase is described by the p-wave pairing state originally proposed by Balian and Werthamer [13]. They showed that the B-phase is the most stable superfluid phase in the weak coupling limit. All three triplet spin configurations are present in this phase: $|\uparrow\uparrow>$, $|\downarrow\downarrow>$ and $|\uparrow\downarrow + \downarrow\uparrow>$. The B-phase has an isotropic energy gap, but intrinsically, it is not isotropic at all. In fact, ^{3}He is an anisotropic superfluid in all its phases. The Balian-Werthamer state is anisotropic in the following sense: in the most general state, the $\mathbf{d}$ vector, which points radially away from the centre of the Fermi sphere, is rotated about an arbitrary axis, which we will call $\hat{N}$, by an angle θ. Thus, the magnetic dipolar energy varies all over the Fermi surface as it

depends on the angle θ. The description of the B-phase is usually given in terms of $\hat{N}$, rather than **d**. The order parameter for the B-phase is

$$A_{\mathrm{B}} = \Delta e^{i\phi} \begin{pmatrix} 1 & 0 & 0 \\ 0 & \cos\theta & -\sin\theta \\ 0 & \sin\theta & \cos\theta \end{pmatrix} \tag{2.16}$$

where Δ is the magnitude of the energy gap. The **d** vector can be obtained by a rotation of angle θ about an arbitrary axis (defined by $\hat{N}$). The magnetic susceptibility is reduced with respect to the normal Fermi fluid due to the $|\uparrow\downarrow + \downarrow\uparrow>$ part of the pairing.

2.1.4 The A-phase

The A-phase is only stable at pressures higher than the pressure of the polycritical point (the point at which superfluid ^{3}He-A, superfluid ^{3}He-B and normal ^{3}He coexist in the phase diagram), which is 21.5 bars in zero magnetic field. It can also be more favorable energetically than the B-phase in a magnetic field or in a state of confinement. The stabilization mechanism for the A-phase pairing is called *spin fluctuation feedback* and it is due to the very formation of the condensate. In the case of ^{3}He there is no lattice with which the quasiparticles can interact and the onset of superfluidity changes the pairing interaction. The idea of spin fluctuation feedback was first introduced by Anderson and Brinkman [14]. The pairing states in the A-phase are only Equal Spin Pairing (EPS) states, i.e. $|\uparrow\uparrow>$ and $|\downarrow\downarrow>$, and therefore its magnetic susceptibility is the same as for the normal Fermi liquid. The **d** vector for the A-phase has the form of the Anderson-Brinkman-Morel [15] state,

which is

$$|\mathbf{d}(\mathbf{k})| = \sqrt{3/2}\Delta(k_1 + ik_2) = \sqrt{3/2}\Delta|k|\sin\theta e^{i\phi} \tag{2.17}$$

and thus

$$\mathbf{d}\cdot\mathbf{d}^* = |(\mathbf{d}(\mathbf{k}))|^2 = 3/2\Delta^2\sin^2\theta \tag{2.18}$$

The energy gap has two point nodes in the k_z direction of the k space and the vector $\mathbf{d}$ points in the same direction in spin space for all points on the Fermi sphere. The order parameter for the ABM state can be written as:

$$A_A = \Delta\begin{pmatrix} 1 & i & 0 \\ 0 & 0 & 0 \\ 0 & 0 & 0 \end{pmatrix} \tag{2.19}$$

Let us remark that in an applied magnetic field, the A-phase is no longer an unitary state, since the components $\Psi_{\uparrow\uparrow}$ and $\Psi_{\downarrow\downarrow}$ are not equal in this case and this implies that $\Delta\Delta^+$ is not an unitary matrix. This leads to a different phase, called A_1 in which only one spin population is present.

Interestingly, a suppression of the z-component of the order parameter would not affect the A-phase, since its z-component is zero. That makes the A-phase a candidate for the stable phases of superfluid ^{3}He confined to a submicron slab geometry.

2.1.5 The planar phase

If we consider the B-phase order parameter and suppress its z-component, the resulting order parameter is also a solution of the BCS gap equation [22]. Assuming, without lost of generality, that the sample lies in the x-y plane, then suppressing

the z-component of the **d** vector leads to the following A matrix:

$$A_{\text{planar}} = \Delta \begin{pmatrix} 1 & 0 & 0 \\ 0 & 1 & 0 \\ 0 & 0 & 0 \end{pmatrix} \tag{2.20}$$

This matrix represents the order parameter of the planar phase. Although it resembles the order parameter of the B-phase, the suppressed part of the superfluid wave function is the term $\Psi_{\uparrow\downarrow}(k)$. This has as a consequence an A-like character for the planar phase and it has, in fact, two nodes along the k_z axis. The difference with the A-phase is that the remaining spin states have opposite angular momentum eigenvalues, so there is not a net orbital angular momentum for the planar phase.

2.1.6 Other phases

As well as the described superfluid phases, other forms of the order parameter for the superfluid state can be stabilized under certain conditions. For example, the mentioned A_1 phase is stable under an external magnetic field. This magnetic field forces the pairing to be in only one of the EPS states with the spins aligned along the field. The order parameter for the A_1 phase is:

$$A_{A_1} = \Delta \begin{pmatrix} 1 & i & 0 \\ i & -1 & 0 \\ 0 & 0 & 0 \end{pmatrix} \tag{2.21}$$

Finally, the equivalent of the planar phase for one dimension is called the polar

phase [22]. Its order parameter has the following form:

$$A_{\text{polar}} = \Delta \begin{pmatrix} 1 & 0 & 0 \\ 0 & 0 & 0 \\ 0 & 0 & 0 \end{pmatrix} \tag{2.22}$$

In order to observe the polar phase the system should be confined to a length comparable to the coherence length in two of the three dimensions.

These two phases are not compatible with our experimental conditions and are mentioned here for completeness only.

2.2 The Ginzburg-Landau approach

The Landau theory of continuous phase transitions applies to changes in a system from a disordered state to an ordered one. A good example of this is the transition between paramagnetism and ferromagnetism at the Curie point in magnetic materials, Bose-Einstein condensation and, of course, the superfluid and superconducting transitions. Continuous phase transitions, also known as Second Order phase transitions, have no associated latent heat. They rather imply a change in the symmetry of the system. The word *continuous* refers to the fact that the *free energy* changes continuously. The symmetries are broken by the phase transition. The Ginzburg-Landau theory states that we can describe a continuous transition by an "order parameter", that is, some quantity which is zero above the transition and rises as we go into the ordered phase. In the previous examples, we could use the magnetization in the ferromagnetic transition, the condensate density in the Bose-Einstein condensation and the A matrix described above in the superfluid transition. After defining an order parameter, the next step is to express the free energy as a function

of that order parameter and minimize it. To a low order approximation, we can write down the free energy as a function of the order parameter as follows:

$$F = -\alpha|A|^2 + \beta|A|^4 + K|\nabla A|^2 \tag{2.23}$$

where the last term accounts for spacial changes on the order parameter. Only even powers of the order parameter appear in the above expression due to symmetry reasons (an easy, although not too rigorous argument would be that the free energy is a scalar quantity whereas the order parameter is a tensor in its more general form). Let us momentarily forget about the spatial variations of the order parameter. If we minimize the free energy with respect to the order parameter we find that $A = \sqrt{\alpha/2\beta}$ and $\alpha \sim (T - T_c)$ since it has to be zero at the transition point. If we now regard the order parameter as a 3×3 complex matrix (case of superfluid ^{3}He) we can express the free energy in the following way:

$$F = -\alpha(T)A^*_{\mathrm{i}\mu}A_{\mathrm{i}\mu} + \beta_1 A^*_{\mathrm{i}\mu}A^*_{\mathrm{i}\mu}A_{\mathrm{j}\nu}A_{\mathrm{j}\nu} + \beta_2 A^*_{\mathrm{i}\mu}A_{\mathrm{i}\mu}A^*_{\mathrm{j}\nu}A_{\mathrm{j}\nu} + \beta_3 A_{\mathrm{i}\mu}A^*_{\mathrm{j}\nu}A^*_{\mathrm{i}\nu}A_{\mathrm{j}\mu} +$$

$$+\beta_4 A_{\mathrm{i}\mu}A^*_{\mathrm{i}\nu}A_{\mathrm{j}\nu}A^*_{\mathrm{j}\mu} + \beta_5 A_{\mathrm{i}\mu}A^*_{\mathrm{j}\nu}A_{\mathrm{i}\nu}A^*_{\mathrm{j}\mu}$$

or

$$F = -\alpha(T)\mathrm{TrAA}^+ + \beta_1|\mathrm{TrAA}^{\mathrm{T}}|^2 + \beta_2(\mathrm{TrAA}^+)^2 + \beta_3\mathrm{Tr}(\mathrm{AA}^{\mathrm{T}})(\mathrm{AA}^{\mathrm{T}})^* +$$

$$+\beta_4\mathrm{TrAA}^+\mathrm{AA}^+ + \beta_5\mathrm{Tr}(\mathrm{AA}^+)(\mathrm{AA}^+)^* \tag{2.24}$$

where A^+ is the hermitian conjugate and A^T is the transpose matrix. The free energy, being a scalar, has to be invariant under symmetry transformations. The Gauge symmetry implies a change in phase, so each term must have as many A's

as A^*'s. Invariance under rotation in the real space (greek letters in the tensor notation) requires contracting the μ and ν indexes and similarly with the first index (latin letters). In the weak coupling limit (the limit in which the B phase is stable), the BCS theory predicts:

$$\alpha^{\mathrm{BCS}}(T) = \frac{N(0)}{3}\Big(1 - \frac{T}{T_{\mathrm{c}}}\Big) \tag{2.25}$$

$$\beta_1^{\mathrm{BCS}} = -N(0)\Big(\frac{1}{\pi k_{\mathrm{B}} T_{\mathrm{c}}}\Big)^2 \frac{1}{30}\frac{7}{8} \quad \zeta(3) \tag{2.26}$$

and

$$-\beta_5^{\mathrm{BCS}} = \beta_4^{\mathrm{BCS}} = \beta_3^{\mathrm{BCS}} = \beta_2^{\mathrm{BCS}} = -2\beta_1^{\mathrm{BCS}} \tag{2.27}$$

where $N(0) = k_{\mathrm{F}}^3/(2\pi^2 v_{\mathrm{F}} p_{\mathrm{F}})$ is the single spin quasiparticle density of states at the Fermi surface and $\zeta(x)$ is the Riemann zeta function. In the strong coupling limit, where the A phase is stable, the β_{i}'s take different values from the BCS prediction. Now we are ready to take into account spatial variations of the order parameter. In the simpler case of superconductors we could define a new variable $f = A/\sqrt{\alpha/2\beta}$ and reformulate Equation 2.23:

$$\frac{K}{\alpha}\frac{d^2 f}{dx^2} + f - f^3 = 0 \tag{2.28}$$

We now define a characteristic length $\xi_{\mathrm{s}} = \sqrt{K/\alpha} = \sqrt{K/\alpha_0}(1 - T/T_{\mathrm{c}})^{-1/2}$ where the subindex s stands for s-wave pairing in the BCS theory. α_0 is a temperature independent constant. ξ_{s} becomes infinite at T_{c} and can be regarded as the minimum length over which the wave function of the Cooper pair is allowed to vary, that is,

the coherence length. In the case of superfluid ^{3}He we could write [5]:

$$F_{\text{grad}} = \sum_{\text{p}} \{K_{\text{L}} |\nabla \cdot A_{\text{pi}}|^2 + K_{\text{T}} |\nabla \times A_{\text{pi}}|^2\} \tag{2.29}$$

for the gradient contribution to the free energy. From the above expression we can define a transversal and longitudinal correlation lengths:

$$\xi_{\text{L}}^2 = \sqrt{\frac{K_{\text{L}}}{\alpha}} = \frac{9}{5} \quad \frac{\xi_{\text{s}}^2}{1 - T/T_{\text{c}}} \tag{2.30}$$

$$\xi_{\text{T}}^2 = \sqrt{\frac{K_{\text{T}}}{\alpha}} = \frac{3}{5} \quad \frac{\xi_{\text{s}}^2}{1 - T/T_{\text{c}}} \tag{2.31}$$

The temperature dependent coherence length in superfluid ^{3}He is usually referred as the shortest one [23], that is, the transverse component

$$\xi^2(T) = \frac{3}{5} \quad \frac{\xi_{\text{s}}^2}{1 - T/T_{\text{c}}}$$

This length is also called the coherence length and is pressure dependent. Its value at zero pressure and zero temperature is 72 nm and it decreases with a pressure increase. Figure 2.1 shows the temperature dependence of the zero pressure coherence length. This is going to be the most important characteristic length in this work and we expect size effects to take place in samples confined to this length scale.

2.3 ^{3}He, a magnetic superfluid

The magnetic properties of the superfluid phases of ^{3}He were first worked out by Leggett shortly after the experimental discovery by Osheroff, Richardson and Lee. It is because of these magnetic properties that experimental tools such as Nuclear

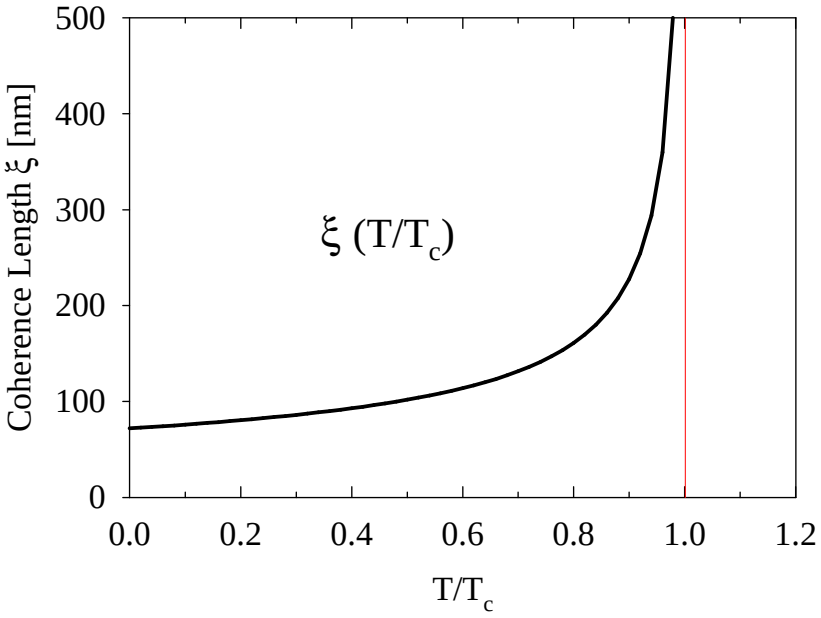

Figure 2.1: The temperature dependence of the zero pressure coherence length. It shows a divergence at the transition temperature and decreases rapidly down to 72 nm at absolute zero.

Magnetic Resonance have proven very useful in the study and recognition of the different superfluid phases.

In the presence of a magnetic field, new terms arise in the expression of the free energy given by Equation 2.24. If we write the anisotropic terms (dipolar and magnetic) of that functional we find that [20]

$$F^{\mathrm{ABM}} = \frac{1}{2}\,\alpha\chi(\mathbf{d}\cdot\mathbf{H})^2 - \frac{3}{5}\,g_{\mathrm{D}}(T)(\mathbf{d}\cdot\mathbf{l})^2 + F^{\mathrm{ABM}}_{\mathrm{grad}}$$

$$F^{\mathrm{BW}} = \frac{4}{5}\,g_{\mathrm{D}}(T)(\cos\theta + 2\cos^2\theta + \frac{3}{4}) + F^{\mathrm{BW}}_{\mathrm{grad}} \tag{2.32}$$

where $\mathbf{H}$ is the applied magnetic field, g_{D} is a measure of the contribution of the Cooper pairs to the dipole energy, χ is the bulk magnetic susceptibility and α is a

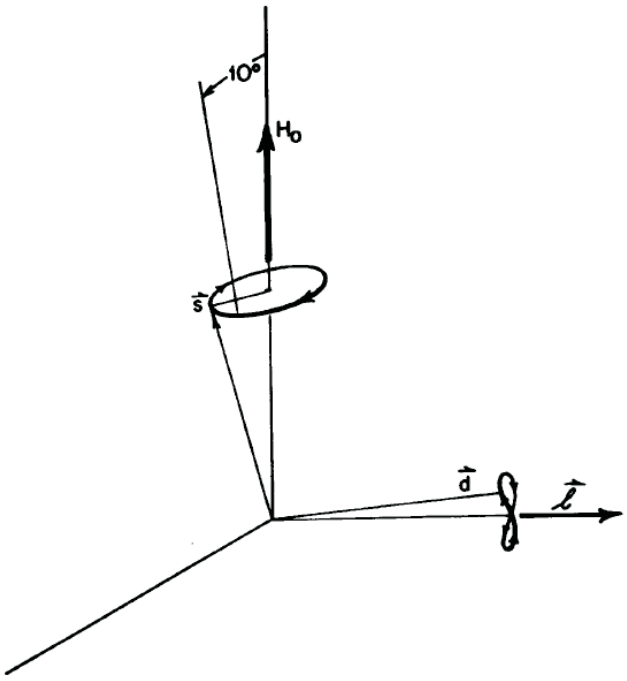

Figure 2.2: Free precession of the spin and **d** vectors after a small tipping pulse for the superfluid A-phase (from D. M. Lee [24])

measure of the susceptibility anisotropy. The angle θ in the B-phase refers to the arbitrary angle between the **d** vector and the $\hat{N}$ axis. Note that the free energy term for the B-phase is purely dipolar, since for the BW state χ is isotropic whatever the orientation of the external field and there is, therefore, no orientating effect in the **d** vector (although there is in the vector $\hat{N}$, which orients along the external magnetic field). This energy term is minimized for an angle $\theta = \cos^{-1}(-1/4) = 104^{\text{o}}$. For the ABW state the **l** and **d** vectors tend to be parallel to minimize the dipolar energy, whereas the **d** vector will try to lay perpendicular to the magnetic field in order to minimize the Zeeman or magnetic term of the free energy.

For the superfluid A-phase, following a small tipping pulse, the spin vector would precess about the total magnetic field, describing an ellipse, as shown in Figure 2.2. Meanwhile, the **d** vector would still try to align along the direction of the **l** vector in

order to minimize the dipole energy (forming what is called "dipole-locked" texture as opposed to the "dipole-unlocked" texture resultant from a $\mathbf{l}\perp\mathbf{d}$ configuration). As a result, the spin vector of the Cooper pair would "feel" an additional field due to the dipolar interaction. This additional field gives rise to a dipolar torque

$$\mathbf{R}_{\mathrm{D}} = \frac{6}{5} g_{\mathrm{D}}(T)(\mathbf{d}\times\mathbf{l})(\mathbf{d}\cdot\mathbf{l})$$

The $\mathbf{d}$ vector would describe a figure eight about the $\mathbf{l}$ vector.

For the B-phase there should not be any transverse frequency shift as long as the tipping angle is kept smaller than the critical angle 104°. The reason for this is that the dipole energy for the B-phase is changed by a small rotation around the z axis, but not by small rotations around the x or y axes. In fact, a rotation of $\mathbf{d}$ around the x or y axis is equivalent to a reorientation of the precessing axis without a change in the angle θ.

2.4 ^{3}He on a regular slab geometry

We will give here a brief review of some of the theoretical and experimental work done in the past regarding superfluid ^{3}He on a confined planar geometry.

2.4.1 Past work: Theory

Although the exact phase diagram of ^{3}He films as a function of temperature and pressure is not experimentally known in this case, there have been several theoretical studies which we will briefly comment here.

One of the first calculations of the effects of the walls on an anisotropic superfluid was done by Ambegaokar *et al.* in 1974 using Green's function methods [5]. They

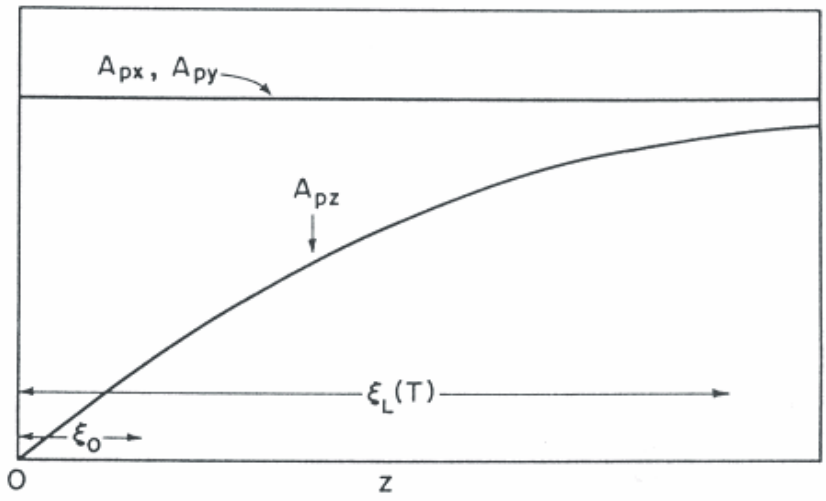

Figure 2.3: The transverse and longitudinal components of the order parameter of ^{3}He near a specularly reflecting wall after Ambegaokar *et al.* [5]. The longitudinal component decays to zero over a length scale of $\xi_{\rm L}(T)$ near the wall whereas the transverse components remain unaffected.

proved that the boundary conditions at the walls strongly affect the longitudinal and transverse components of the order parameter over a length scale given by $\xi_{\rm L}(T)$ and $\xi_{\rm T}(T)$, respectively. For a specular wall, the longitudinal component of the order parameter is zero at the walls and recovers to its bulk value over a length scale of $\xi_{\rm L}(T)$. The transverse components, on the other hand, remain unaffected. For a diffuse wall, all components are zero at the walls and recover to their bulk values over length scales of $\xi_{\rm L}(T)$ (the longitudinal component) and $\xi_{\rm T}(T)$ (the transverse components). The results for a specular wall are shown in Figure 2.3.

Based on the work of Ambegaokar *et al*, Kjäldman *et al.* calculated the transition temperature as a function of film thickness for an infinite slab enclosed between two

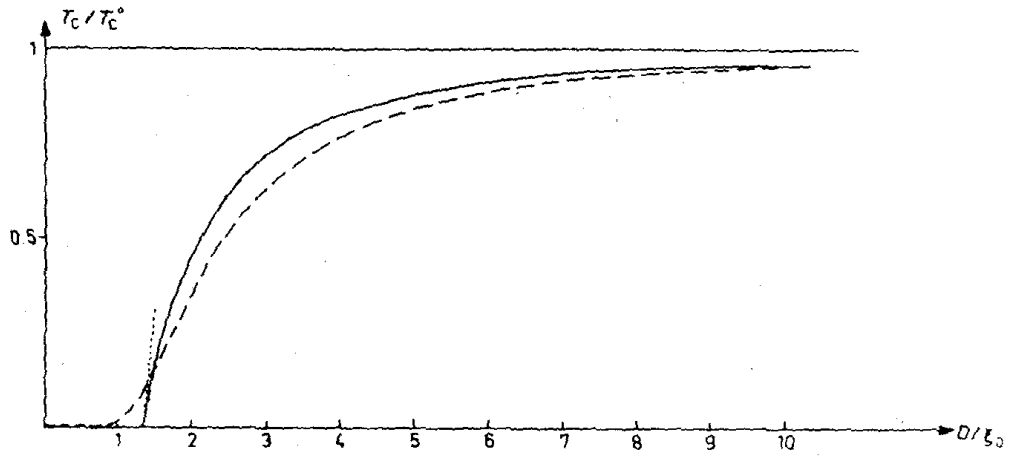

Figure 2.4: Transition temperature as a function of the thickness D in a slab between diffusely scattering planes after Kjäldman *et al* [25]. The asymptotic results in the Ginzburg-Landau range and near the critical thickness are given as a dashed line and a dotted line, the full numerical result as a solid line.

diffusive walls [25]. They found that, in the Ginzburg-Landau limit, the dependence of the transition temperature on the slab thickness (D) had the form

$$T_c^{\rm film} = T_c^{\rm bulk} \exp(-\frac{3}{5}\xi_s^2 \pi^2 / D^2)$$

Below about 0.9 T_c, numerical calculations showed that the Ginzburg-Landau prediction was underestimating the film transition temperature (see Figure 2.4), the highest discrepancy taking place at $D \sim 3\xi_o$, where the underestimation reached $\sim 10\%$ $T_c^{\rm bulk}$.

Fetter and Ullah [26] included the influence of strong coupling corrections to the Ginzburg-Landau formalism and obtained phases diagrams for specular and diffuse

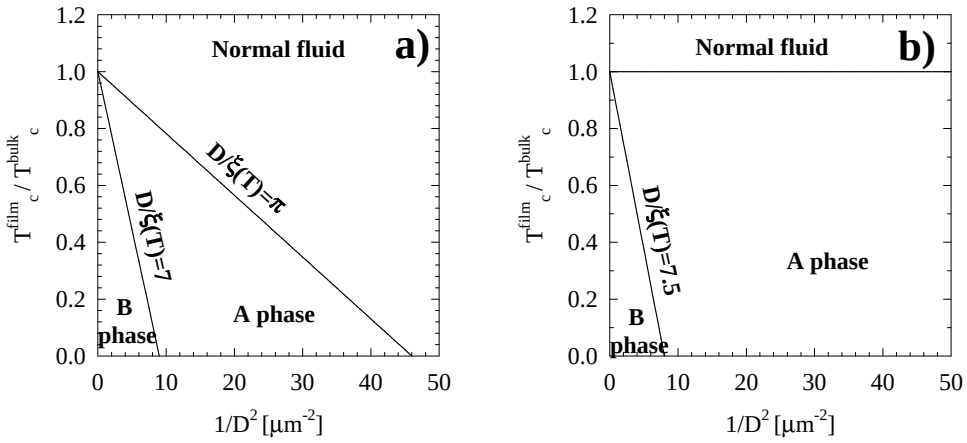

Figure 2.5: Transition temperature versus film thickness for superfluid ^{3}He at zero pressure. Both diffuse scattering (a) and specular scattering (b) are shown. After Fetter and Ullah [26].

scattering at zero pressure which included both A- and B-phases. Interestingly, specular scattering did not suppress the superfluid transition temperature, but it did stabilize the A-phase down to zero temperature for thicknesses smaller than about 5 coherence lengths. These phase diagrams are shown in Figure 2.5. Note that the boundary between the A- and B-phases depends only weakly on the surface scattering conditions.

Li and Ho [27] took into account the pressure and produced several phase diagrams (see Figure 2.6), for both diffuse and specular scattering, over a range of thicknesses from 200 nm to 500 nm. They found that the A-phase was favored by the boundaries in very narrow slabs. In particular, for diffuse scattering, it was stable for thicknesses $D \leq 7.5\ \xi(T, P)$, in good agreement with Fetter and Ullah.

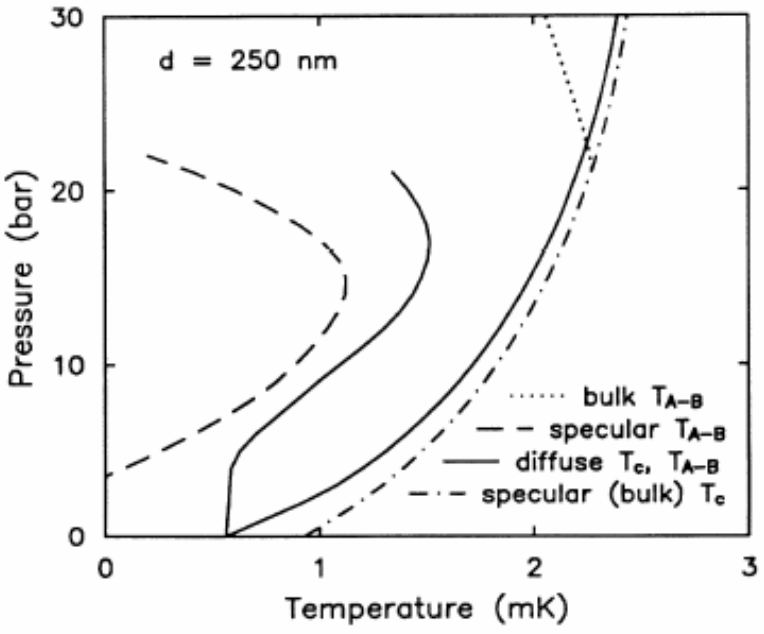

Figure 2.6: Phase diagram for a 250 nm thick superfluid ^{3}He slab with both specular and diffuse surfaces. After Li and Ho [27].

At low temperatures and high pressures, the A-phase, whose order parameter was purely transverse, was unstable against what they called a "deformed" B-phase, or B-planar, which had both, longitudinal and transverse components of the order parameter. Since the effect of the pressure is to diminish the size of the coherence length, the high pressure part of the phase diagrams from Li and Ho would be similar in nature to a thicker film at zero pressure, where the B-phase was found stable by Fetter and Ullah.

One theoretical treatment of a film confined between a diffuse and a specular boundary is that of Vorontsov and Sauls [28]. They used quasiclassical transport equations to obtain the phase diagram shown in Figure 2.7. To compare this diagram with Figure 2.4 and Figure 2.5 the x-axis should be multiplied by two to account

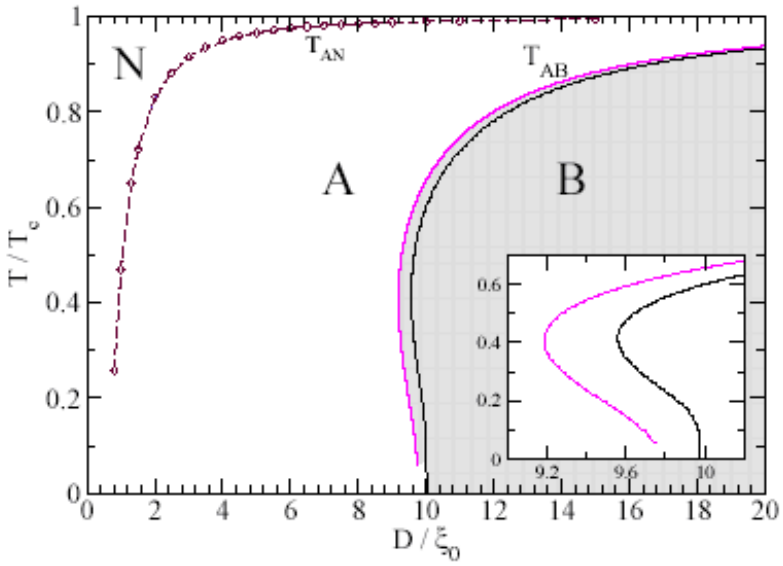

Figure 2.7: Phase diagram for superfluid ^{3}He films with one diffuse and one specular boundary. The inset shows an enlarged portion of the AB-phase boundary. After Vorontsov and Sauls [28].

for the specular boundary of the free surface. In this case, the smaller thickness for which the B-phase can be stabilized is of 10 coherence lengths at zero temperature. This shows a clear disagreement with Fetter and Ullah, who give 7 coherence lengths as the minimum thickness for which the B-phase could exist *between two diffuse walls*. The origin of this discrepancy is two-fold. On one hand, each of these two works use a different definition of the coherence length: Fetter and Ullah use 50 nm for the zero pressure, zero temperature coherence length whereas Vorontsov and Sauls use 72 nm. On the other hand, there is the problem of the effect of the boundaries. In fact, whereas the A-phase has an order parameter somehow insensitive to specular reflections, that is not the case for the B-phase. The scattering with the surface breaks the rotational symmetry of the Cooper pair. For the B-phase, with

an isotropic energy gap, this translates into sub-gap excitations (which are, actually, Andreev bound states) which eliminate the isotropy of the order parameter in momentum space. In other words, the specular scattering suppresses the component of the order parameter perpendicular to the wall. The A-phase, on the other hand, has an order parameter with only longitudinal components. The rotational symmetry is already broken by the equal spin pairing. This is why we can consider a film with one diffuse and one specular boundary equivalent to a film with two diffuse boundaries and double thickness for the A-phase, but not for the B-phase.

A remarkable feature in this phase diagram is the re-entrance A $\longrightarrow$ B $\longrightarrow$ A which takes place on cooling a film at a constant thicknesses of the order of 10 ξ_o. The actual candidate for the thin films regime is the A-like planar phase described above, also with only longitudinal components of the order parameter. The transition from A (planar) to B and then to A again is the cause of a broken *translational* symmetry along the plane of the film. This is a rather striking effect because the system seems to have a perfect planar symmetry if we consider an infinite slab. However, as we cross vertically the phase diagram over the re-entrance area, the transverse component of the order parameter appears (B-phase) and disappears (A-phase). That, coupled with the scattering at the walls, produces a broken symmetry in the plane of the film.

That broken symmetry might suggest a novel inhomogeneous phase of the superfluid with an off-diagonal term in the order parameter.

$$A_{\mathrm{Inhomog}} = \begin{pmatrix} \Delta & 0 & 0 \\ 0 & \Delta & 0 \\ \Delta_x & 0 & \Delta_z \end{pmatrix} \tag{2.33}$$

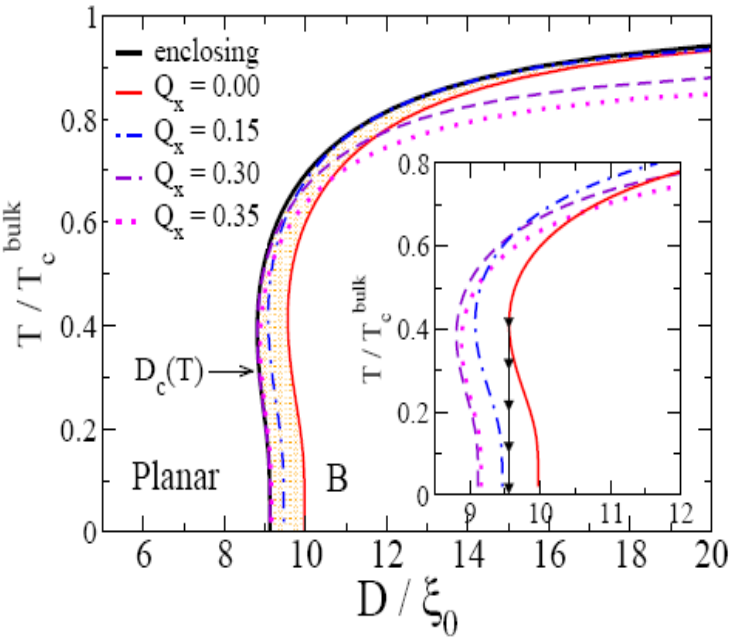

Figure 2.8: Phase diagram for superfluid ^{3}He showing the hypothetical stabilization of an inhomogeneous phase (striped phase) next to the re-entrance of the A-phase. From Vorontsov and Sauls [28]. See text for explanation.

where now Δ_x and Δ_z are the magnitudes of the energy gap along the x and z axes, respectively. Note that the x axis is on the plane of the slab and the z axis is normal to it. In Figure 2.8 we can see an hypothetical phase diagram showing the inhomogeneous phase between the A- and the B-phases. Here, Q_x is the wave vector in the x direction. For each value of the temperature and Q_x we can obtain a critical Q_z^c or, in other words, a critical thickness $D_c = \pi/Q_z^c$. The Figure shows the transition lines (critical thicknesses) for different values of Q_x. The physical transition occurs for the Q_x-mode with the lowest D_c. As we can see, for large thicknesses the transition occurs for a value of Q_x=0.15, whereas at lower thicknesses it happens at Q_x=0.30. The black line, enclosing the modes of minimum critical thickness, represents the physical transition and the red line the mode for which

Q_x=0 or, in other words, the transition to the B-phase. Finally, the inset shows a blow-up of the re-entrant region.

Another work that studied the size effects on a slab with one diffuse and one specular surface is that of Yamamoto *et al.* [29]. They used the quasi-classical Green's function method to obtain the superfluid density as a function of temperature for various film thicknesses. They found reasonable agreement with previous experimental work [30] for films thinner than 174 nm, whereas their calculations for thicker films deviated from the experimental observations.

Although not relevant to this work in particular, there have been other theoretical studies regarding much thinner films. A firm candidate in this very thin regime is a Kosterlitz-Thouless phase transition [6]. Another possible 2-D transition was suggested by Stein and Cross [31]. They proposed a two-dimensional Ising-like phase transition in the ^{3}He order parameter in which "islands of reversed $\mathbf{l}$" spontaneously nucleated as a consequence of the Z_2 symmetry of the order parameter. This Z_2 symmetry coexisted with the $U(1)$ gauge symmetry associated with the standard Kosterlitz-Thouless transition. This work was later complemented by Kawamura [32], who considered the additional internal symmetry $SO(2)$ associated with the nuclear spin degree of freedom. He predicted, for films of thicknesses of 100 nm or less with specular boundaries, two successive transitions with an intermediate non-superfluid phase. The upper transition could be identified by a logarithmically divergent anomaly in the heat capacity whereas the lower transition was characterized by the onset of standard superfluidity and could be detected by usual torsional oscillator techniques. The intermediate phase, although did not exhibit real superfluidity, was a low-dissipation state. Such a low-dissipation state has already been observed experimentally [33], [34].

The possibility of a gapless superfluid, i. e. a superfluid with zero energy gap,

taking place in ^{3}He for film thicknesses smaller than the coherence length and comparable to the interparticle separation k_{F}^{-1} was pointed out by Tešanović and Valls [35], [36], [37]. Although very demanding technically, the experimental confirmation of these theories regarding films of thicknesses of the order of hundreds of angstroms is expected to happen in some near future.

2.4.2 Past work: Experiments

Research concerning stable samples of confined superfluid ^{3}He is technically very demanding. This is the reason for which the theoretical treatments anticipated the experimental work on such systems. We discuss below the most significant experimental studies on superfluid ^{3}He slabs.

Although there had been previous works concerning superfluid ^{3}He in a confined geometry (supercurrent through a nucleopore, in particular [34]), the first observation of film flow on ^{3}He was made at Queen's University in 1985 [38]. They used a copper beaker open at the bottom to a main ^{3}He reservoir. The chamber outside the beaker contained a capacitive level detector. They filled the main reservoir with ^{3}He until the level inside the beaker was at the rim and the level outside the beaker was about 10 mm below the rim. In this state, a meniscus formed inside the beaker with ^{3}He slowly flowing over the rim of the beaker. They converted the film flow into critical current and measured the superfluid transition. Their reported T_{c} for film thicknesses comparable to the coherence length was of the order of 3 mK, higher than the bulk transition temperature at saturated vapour pressure (0.94 mK) and in disagreement with the theoretical predictions. These disagreements were attributed to a thermal gradient in the cell which caused the film flow through the thermomechanical effect (see Section 3.4). A later work by the same group [40] used

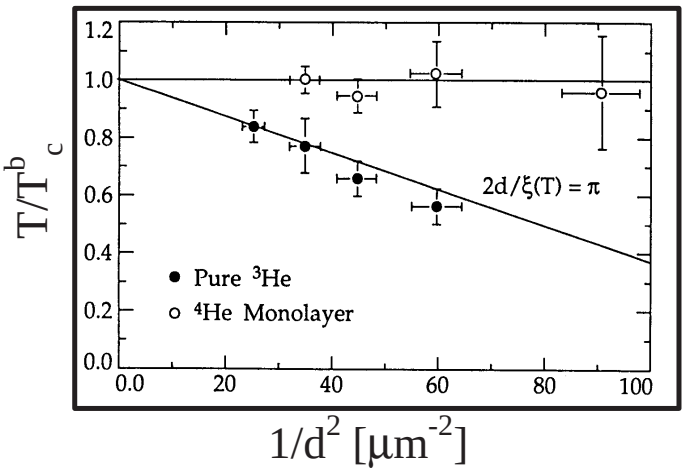

Figure 2.9: Superfluid transition temperatures as a function of film thicknesses as measured by Steel *et al.* [39]. A ^{4}He monolayer changed the boundary conditions and no suppression on T_c was observed.

an improved cell which eliminated the thermal gradient to measure the superfluid transition in films of nominal thicknesses of 90, 100, 110 and 120 nm. They observed a suppression of T_c for all their samples, but it was not in agreement with the theoretical predictions [25], [26]. The reason, as they later realized, was that the sharp corners of the beaker rim led to ambiguities in the interpretation of the results. The details of the profile of the rim were critical, since a sharp edge of the rim would cause the ^{3}He film to thin as it passed over that edge. Also, small scratches across the rim were observed in scanning electron micrographs of the beaker. That formed parallel flow paths with dimensions independent of the film thickness.

To overcome these difficulties they designed a round rim beaker with which they had a well defined curvature of the film passing over the rim [39]. This time they

observed an agreement with the Ginzburg-Landau predictions ($2D_c/\xi(T) = \pi$ with the factor of two accounting for the free surface). Their results are displayed in Figure 2.9. By coating the chamber with monolayers of ^{4}He, they did not observe a suppression of the superfluid transition at all. Their flow rate, which scaled as $(1-T/T_c^{\rm film})^{3/2}$, was one order of magnitude lower than expected. Interestingly, they found an sudden flow rate transition as they thinned their film. This was attributed to a transition from a B-like phase to an A-like phase.

Almost at the same time as this later experiment, another film flow experiment was carried out at Berkeley [41]. They used a copper cylinder partially immersed in a bath of liquid ^{3}He. The flat top surface of the cylinder protruded a distance h above the bath. Slightly above this top surface, forming a capacitive gap, was located a flat metal disk. The application of a dc voltage drove the liquid into the capacitor gap. Using this technique, they also observed a suppression of T_c as the thickness of the film decreased. The observed temperature dependence of the critical current in the Ginzburg-Landau regime was $j \sim (1-T/T_c^{\rm film})^{3/2}$, as shown in Figure 2.10. However, they did not have an accurate measure of their film thicknesses.

In 1990, Freeman and coworkers performed measurements on 300 nm thick films of ^{3}He confined between closely spaced 1.5 μm thick Mylar sheets [42]. Figure 2.11 shows one of the results of this experiment. Their experimental cell combined the Nuclear Magnetic Resonance and Torsional Oscillator techniques. They observed transition temperatures, superfluid densities and Nuclear Magnetic Resonance frequency shifts in good agreement with the theory. Pressure was applied ranging from 1.5 to 22.6 bars. Nuclear Magnetic Resonance allowed them to positively identify the superfluid phase as A-like. This phase was stable down to 0.3 mK, a region of the phase diagram where the theory would predict a B-like phase as the stable one. However, a transition into the B-phase was never observed in this experiment,

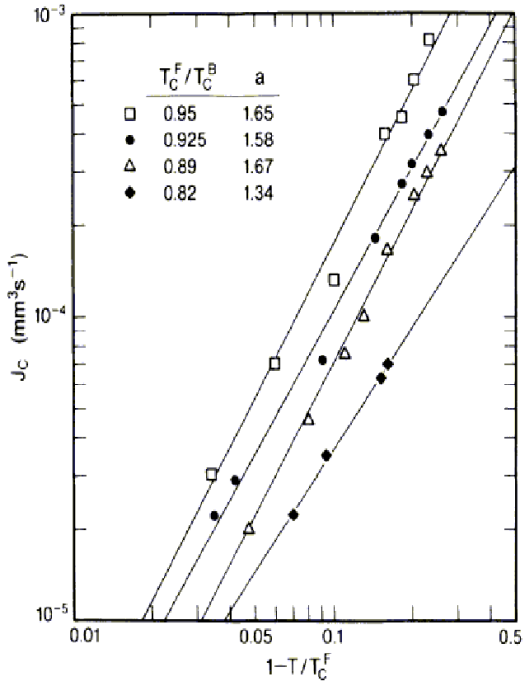

Figure 2.10: Critical currents for different values of $T_C^{\rm film}$ as a function of $(1-T/T_C^{\rm film})$ after Davis *et al.* [41].

probably due to a supercooling effect on the A-phase. Another major advance in this work was in changing the boundary conditions from diffuse to specular by pre-plating the substrate with ^{4}He. Under specular boundary conditions, the transition temperature remained the same as for bulk samples (see Figure 2.11).

Also in 1990, researchers at Purdue University [43] used a torsion pendulum to perform measurements on a broad range of film thicknesses. They developed a technique which allowed them to grow metastable unsaturated ^{3}He films on the surface of an oscillating copper plate. It consisted of heating a small ^{3}He reservoir at the base of their cell and allowing the ^{3}He atoms transferred through the vapour to condense at the bottom surface of the copper plate.

The thicknesses of the films varied between 83 and 172 nm and they found that

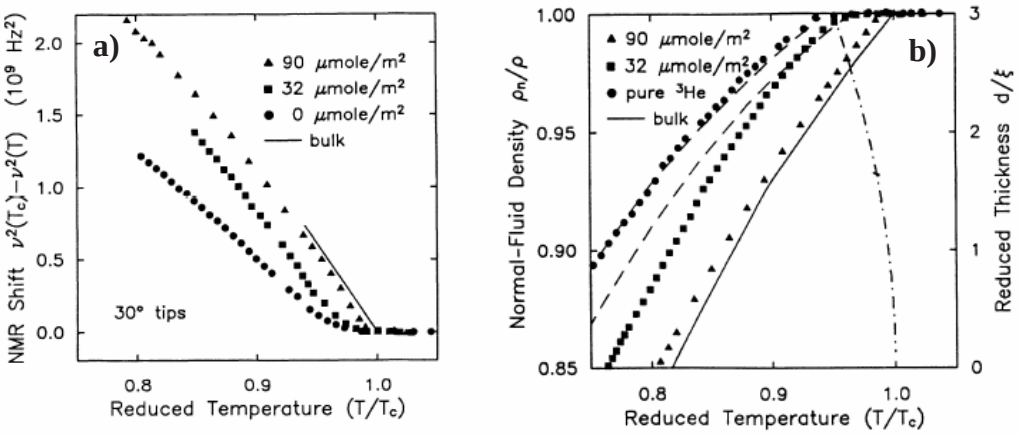

Figure 2.11: The NMR shift (a) and normal fluid density (b) for different boundary conditions after Freeman *et al.* [42]. The boundary conditions correspond to 0-, 32- and 90-μmole/m^2 ^{4}He coverages. The ^{3}He pressure is 8.5 bars. The transition temperature is suppressed as the scattering changes from specular to diffuse.

the films slowly thinned if held well below the superfluid transition temperature, the typical rate being 100 Å per day. We can see their results in Figure 2.12. The transition temperature decreased with film thickness in good agreement with the theory of Kjäldman *et al.* Also, the superfluid density was suppressed as the films got thinner. In particular, they found that the superfluid density as a function of the reduced thickness $w = d/\xi(T)$ fell onto two different curves depending on whether the films were thicker or thinner than 137 nm (see Figure 2.13). Since the B to A phase transition was expected to occur at higher thicknesses, they attributed this behaviour to a transition into a new phase.

Using a third sound technique, Schechter *et al.* [30], [44] measured in 1998 the

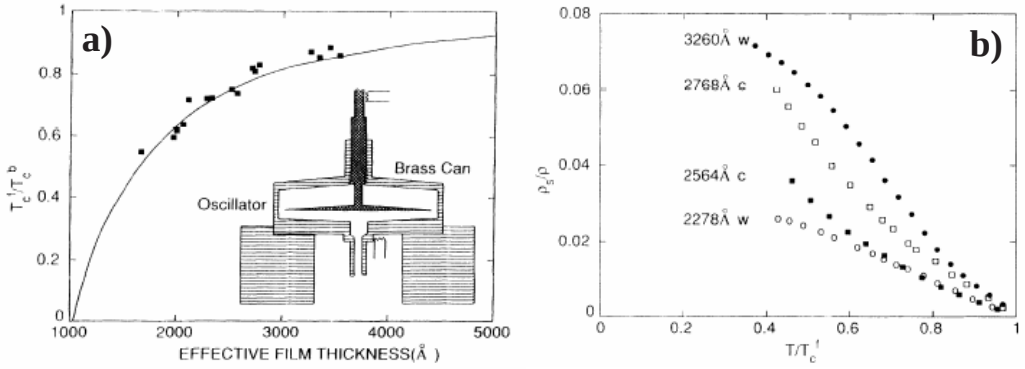

Figure 2.12: Reduced transition temperature (a) and superfluid density (b) for several effective film thicknesses after Xu and Crooker [43]. The inset on (a) shows the experimental cell.

superfluid density as a function of temperature for films of thicknesses ranging from 92 to 281 nm. In this experiment, a thick horizontal copper disk was positioned in a container of superfluid ^{3}He and its polished top surface formed the substrate for the superfluid film. The third sound waves were excited and detected capacitively and their speed gave a measure of the superfluid density. Their results agreed with the Ginzburg-Landau predictions for their thickest films, but for films thinner than $\sim$ 200 nm the slope of their observed data near T_c was smaller than the theory would have it (see Figure 2.14). They also studied the effect of ^{4}He coating of the substrate. For a given temperature and film thickness they found the superfluid density was dramatically increased with adding ^{4}He. The transition temperature, also, was found to be closer to the bulk transition temperature. A side-effect of

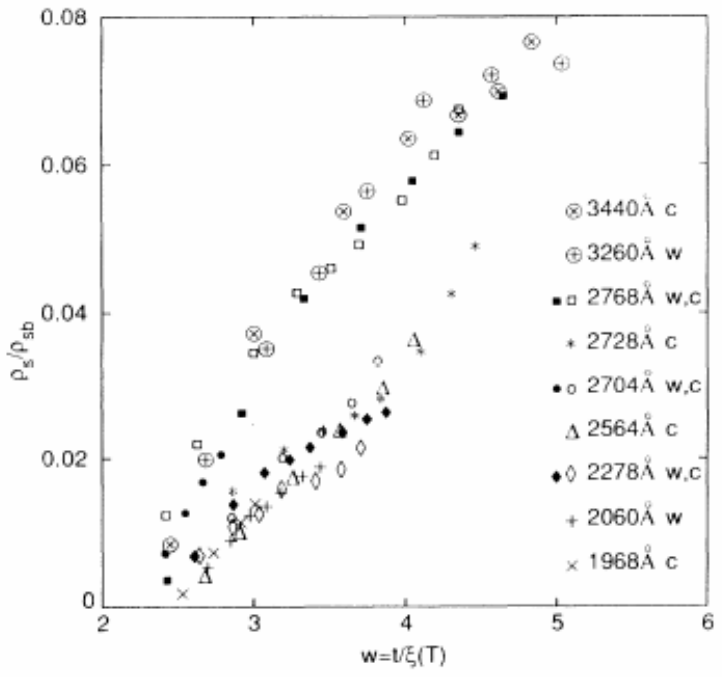

Figure 2.13: Superfluid film densities normalized to the bulk superfluid density as a function of the reduced film thickness after Xu and Crooker [43].

the ^{4}He coating was an increase in the base temperature to which ^{3}He could be cooled due to the increased Kapitza resistance between the heat exchangers and the experimental ^{3}He. This minimum temperature went from 0.38 T_c for pure ^{3}He to 0.68 T_c for 2.5 layers of ^{4}He coating the copper substrate.

Finally, in more recent times, a group in Osaka has performed continuous wave longitudinal Nuclear Magnetic Resonance on ^{3}He films with fixed thicknesses of 0.8 and 1.1 μm [45], [46], [47]. By varying the pressure, they could change the reduced slab thickness $d/\xi(T)$. They observed the A-B phase transition for a number of pressures ranging from 10 to 27 bar, the transition temperatures being suppressed by about 15 % from those of the bulk liquid. They also found that below a certain pressure-dependent value of the reduced thickness only the A-phase was stable.

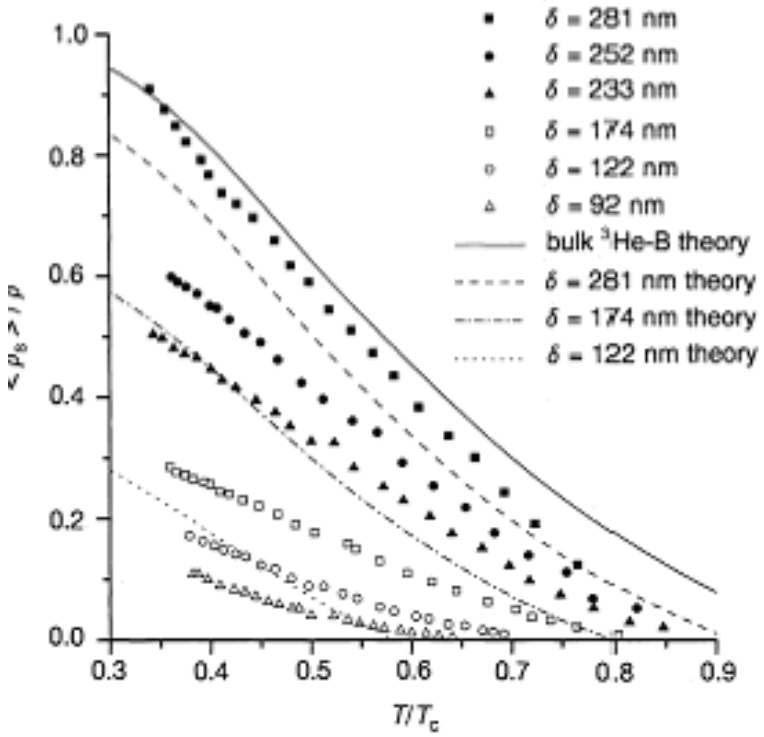

Figure 2.14: Average superfluid densities obtained from the speed of third sound as a function of reduced temperature after Schechter *et al.* [30]. The lines represent the Ginzburg-Landau predictions for a ^{3}He-B film enclosed between two diffusively scattering walls.

Reliable measurements of these features at saturated vapour pressure were, however, not reported in their work.

Although there have been a number of experiments on systems similar in nature to the one which is the object of this work, the phase diagram of confined superfluid ^{3}He is far from been mapped out. We have seen that most of the previous research observed a suppression of the transition temperature. The qualitative behavior of the superfluid, however, was not always in agreement with the existing theories, especially for very thin films. It is in that regime where the most exciting (and most technically challenging) research remains and novel physics is expected to arise from the study of these systems.

Chapter 3

The NMR experiment

In these days, a man who says a thing cannot be done
is quite apt to be interrupted by some idiot doing it.

Elbert G. Hubbard.

Rationale

Nuclear Magnetic Resonance (NMR) was the tool originally used to explore the mysteries of the new observed phases of ^{3}He, back in 1972. It was crucial in clarifying that the new features actually came from the liquid [4] and not from a magnetic ordering in the solid, as was at first believed. Since then, NMR has been used in countless experiments regarding ^{3}He. One of the beauties of doing NMR on ^{3}He is that it not only provides a clear signature of the superfluid transition, but it also shows, in the words of Leggett, the "fingerprints" of each phase.

The applications of NMR, not only in physics, but in many scientific subjects,

are numerous. They include chemical structural analysis and chemical dynamics, atomic motion in fluids and solids, 3D imaging or molecular design.

In this experiment we use pulsed NMR to study films of ^{3}He of thicknesses comparable to the superfluid coherence length. Due to the extremely small size of the required samples it is needed to design a spectrometer involving a SQUID (Superconducting QUantum Interferometer Device) to achieve the required signal sensitivity. This Chapter describes the basics of NMR and SQUIDs along with the design and characteristics of the spectrometer used. The NMR cell is also described in detail before presenting the experimental results and discussing them.

3.1 The Physics behind NMR

3.1.1 The basics

There exists an extensive literature concerning NMR [48], [49], [50] and therefore we will only give here a brief description of the underlying physics.

NMR is a phenomenon which arises from the interaction between matter and electromagnetic radiation. It is well known that if we apply a magnetic field $\mathbf{H}$ to a non-ferromagnetic material it develops a magnetisation $\mathbf{M}$ according to the relationship

$$\mathbf{M} = \chi \mathbf{H} \tag{3.1}$$

A word of caution here: the magnetic susceptibility χ is a tensor. That means that the magnetisation does not necessarily need to be aligned with the applied magnetic field. In fact, that only happens for linear isotropic materials. In an isotropic material the magnetic susceptibility tensor is a diagonal matrix. If, in addition, the material is linear, then the magnetisation is proportional to the external field. From

this point onwards we will only refer to linear and isotropic systems [1] and will treat the (now diagonal) tensor χ as a scalar.

Let us consider now a nuclear magnetic moment $\boldsymbol{\mu}$. When placed in a magnetic field $\mathbf{B}$ it will experience a torque. The rate of change of the angular momentum is proportional to this torque (in the same way as it happens with a precessing top in a gravitational field according to Newton's Second Law)

$$\boldsymbol{\mu} \times \mathbf{B} = \hbar \dot{\mathbf{L}}$$

Since the magnetic moment is related to the angular momentum itself by $\boldsymbol{\mu} = \gamma \hbar \mathbf{L}$ we can write

$$\dot{\boldsymbol{\mu}} = \gamma \boldsymbol{\mu} \times \mathbf{B}$$

where γ is called the *gyromagnetic ratio*.

We can apply the above analysis to an assembly of magnetic moments by defining the magnetic moment per unit volume, or magnetisation $\mathbf{M}$. We have, then,

$$\dot{\mathbf{M}} = \gamma \mathbf{M} \times \mathbf{B} \tag{3.2}$$

The solution of this equation of motion is a precession of the vector $\mathbf{M}$ around the magnetic field with an angular velocity $\boldsymbol{\omega} = \gamma \mathbf{B}$. This angular velocity is called the Larmor frequency. In a real material, however, not all the spins see exactly the same static field due to field inhomogeneities and the magnetic moments of the neighbour spins. As a result, the Larmor frequency varies over the sample.

[1] It might seem at first sight that superfluid ^{3}He has an anisotropic magnetic susceptibility tensor for all its phases, even for ESP states. What actually happens is that the tensor is anisotropic *for a constant* $\mathbf{d}$ *vector*. Under the influence of a magnetic field the $\mathbf{d}$ vector will tend to accommodate perpendicular to it in order to minimize the Zeeman energy of the pairs, making the system effectively isotropic

One needs to be careful and apply rigorously the relation between the fields **B** and **H**

$$\mathbf{B} = \mu_{\mathrm{o}}(\mathbf{H} + \mathbf{M})$$

where μ_{o} is the magnetic permeability of the free space. Therefore equation 3.1 becomes

$$\mathbf{M} = \frac{\chi}{(1+\chi)}\frac{\mathbf{B}}{\mu_{\mathrm{o}}}$$

Usually, for paramagnetic materials, $\chi << 1$ and we can approximate equation 3.1 by

$$\mathbf{M} = \frac{\chi}{\mu_{\mathrm{o}}}\mathbf{B}$$

It is necessary to clarify the conditions for linearity in an isotropic paramagnetic material. It can be shown from basic statistical mechanics that a sample consisting of n particles per unit volume with spin 1/2 in a magnetic field **B** has a magnetisation given by

$$M_{\mathrm{o}} = n\mu \tanh\left(\frac{\hbar\gamma B_{\mathrm{o}}}{2k_{\mathrm{B}}T}\right)$$

where μ is the magnetic moment of a single spin. For small fields and/or high temperatures (low polarization) we can approximate the hyperbolic tangent in first order and obtain

$$M_{\mathrm{o}} = \frac{n\hbar^2\gamma^2}{4k_{\mathrm{B}}T}B_{\mathrm{o}} \tag{3.3}$$

where the relation $\mu = \gamma\hbar/2$ has been used. Equation 3.3 is known as *Curie's Law*: for a paramagnetic material the magnetisation is proportional to the external field and inversely proportional to the temperature. The magnetic susceptibility in the linear region becomes then

$$\chi_{\mathrm{o}} = \frac{\mu_{\mathrm{o}}n\hbar^2\gamma^2}{4k_{\mathrm{B}}T}$$

3.1.2 Relaxation

We have said that in the ultimate equilibrium state of a linear isotropic paramagnetic system under the influence of a magnetic field the magnetisation is parallel and proportional to the field and the components perpendicular to the field are zero. That equilibrium state is reached through a process called *relaxation*. The process by which the magnetisation becomes proportional to the magnetic field is called spin-lattice relaxation and involves a change of the magnetic energy density $-\mathbf{M}\cdot\mathbf{B}$ due to interactions between the spins and the lattice. The characteristic time of the spin-lattice relaxation is called T_1. The vanishing of the transversal components of the magnetisation has to do with the slightly different field seen by each of the spins due to the presence of the neighbours and/or any possible field inhomogeneities. This process is called spin-spin relaxation and its characteristic time is called T_2.

The relaxation process was first described from a pure phenomenological approach by Felix Bloch in 1956 through the following equations:

$$\dot{M}_{\mathrm{z}} = \gamma|\mathbf{M}\times\mathbf{B}|_{\mathrm{z}} + \frac{M_{\mathrm{o}} - M_{\mathrm{z}}}{T_1}$$
$$\dot{M}_{\mathrm{x}} = \gamma|\mathbf{M}\times\mathbf{B}|_{\mathrm{x}} - \frac{M_{\mathrm{x}}}{T_2}$$
$$\dot{M}_{\mathrm{y}} = \gamma|\mathbf{M}\times\mathbf{B}|_{\mathrm{y}} - \frac{M_{\mathrm{y}}}{T_2}$$

According to Bloch equations, the components of the magnetization evolve as

$$M_{\mathrm{x,y}}(t) = M_{\mathrm{x,y}}(0)\cos(\omega_{\mathrm{o}}t)exp(-t/T_2)$$
$$M_{\mathrm{z}}(t) = M_{\mathrm{o}} - [M_{\mathrm{o}} - M(0)]exp(-t/T_1)$$

T_2 is related to differences in the local magnetic fields experienced by the spins.

Experimentally, however, the external magnetic field usually presents inhomogeneities which also affect T_2. T_2^* is the spin-spin relaxation time taking into account any potential inhomogeneity in the external field. The relationship between these is

$$\frac{1}{T_2^*} = \gamma \Delta B + \frac{1}{T_2}$$

where ΔB represents the inhomogeneity in the field.

Nuclear Magnetic Resonance can also be described in quantum mechanical terms. A static magnetic field would split the energy levels of the system according to the Zeeman effect. The splitting would have a spacing proportional to the field $\Delta E = \hbar \gamma B$. If we now use electromagnetic radiation of frequency $f = \gamma B / 2\pi$ we can induce transitions (resonance) between the levels.

3.1.3 CW and Pulsed NMR

There is not a single method for investigating nuclear resonance. We could, for example, study what happens to our system under the influence of a continuous periodic disturbance. Or, on the other hand, we could apply a temporary disturbance and observe the subsequent evolution of the system. The first method is called *continuous wave* (CW) NMR and the second Pulsed NMR. The NMR pulses are usually applied perpendicular to the static magnetic field and this method is called transverse pulsed NMR. Longitudinal pulsed NMR is a special case of performing the technique. Superfluid ^{3}He, for example, exhibits a longitudinal resonance, whereas normal ^{3}He does not. Historically, CW was almost the only method used to perform NMR for the first decade of the technique (1946-1956), but more recently Pulsed NMR has become the dominant method due to its versatility.

CW and the NMR following a single pulse are completely equivalent but the

convenience of one or the other methods highly depends upon the sort of experiment we are dealing with. CW NMR is easier from the analytical point of view, since the output does not need specialised Fourier analysis. In fact, one method is the Fourier transform of the other. In CW NMR the sample is placed inside a coil and a small RF magnetic field is continuously applied. The frequency of the RF field is slowly swept through resonance and the resonant power absorption is measured from the RF voltage induced across the coil. But not all the specimens are suitable for CW NMR. Firstly, very small systems would benefit from a better signal to noise ratio. And secondly, signals with very long T_2^* would have their spin-spin relaxation masked by field inhomogeneities. T_1 and T_2^* are much easier to measure using pulsed techniques by just Fourier transforming the time domain decay of the response to the short pulse and measuring the width of the resulting curve. Pulsed NMR also allows to repeatedly average the time domain response to a series of N pulses, thus increasing the signal to noise ratio by a factor $\sqrt{N}$.

It is for the above reasons that we choose to use Pulsed NMR in order to study our ^{3}He films.

3.2 The SQUID NMR spectrometer

The SQUID NMR spectrometer described in Section 3.3 is based in the previous work of Dyball in this same group [51]. We will start by giving a brief account of the physics and operation of DC SQUIDs in this Section before going into further details concerning the spectrometer.

3.2.1 The DC SQUID

SQUIDs are amongst the most sensitive existent devices. Any physical quantity that can be converted into a magnetic flux is susceptible to be measured by a SQUID, hence the wide spectrum of applications of these devices in science: from detecting varying magnetic fields coming from the human brain to the search of gravitational waves. A SQUID consists of a superconducting ring containing one (rf SQUIDs) or two identical (DC SQUIDs) Josephson junctions. The DC SQUID is operated with a steady current bias and the RF SQUID with a radiofrequency flux bias. Two physical phenomena constitute the basics of SQUIDs: flux quantization inside a superconducting loop and Josephson tunnelling. The difference in the phase of the electrical current across the Josephson junctions produces an output voltage across the SQUID which is periodic in magnetic flux. It is not uncommon to be able to detect changes in the magnetic flux of less than a flux quantum. We will concentrate on the physics of the DC SQUID, since that is the kind of SQUID used in these experiments.

The two Josephson junctions are shunted with an external resistance to remove any hysteretic behaviour in the I-V characteristic. Each junction has a critical current above which it becomes resistive. The SQUID is biased with a current which is greater than twice the critical current. If we now apply a magnetic flux through the loop the SQUID will generate a current to counteract the applied flux. The system shows a different I-V characteristic curve for each different flux threading the loop, as shown in Figure 3.1a. For a constant current we can plot the V-ϕ characteristic (Figure 3.1b) which is periodical in flux, the period being one flux quantum ($\phi_o = h/2e$) and whose amplitude has the value of the voltage swing between both I-V characteristics (red line in Figure 3.1a). The maximum critical

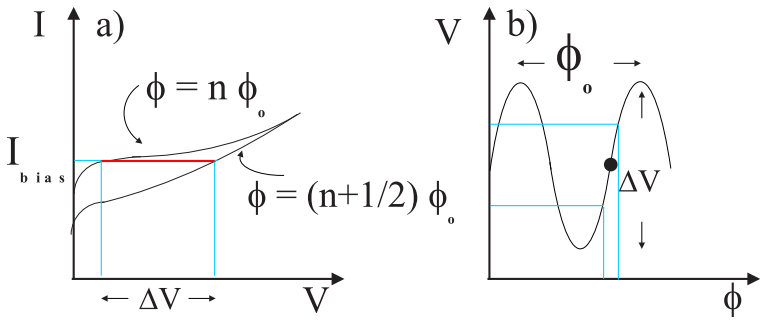

Figure 3.1: Typical SQUID I-V (a) and V-ϕ (b) characteristics. The SQUID is biased with a current greater than $2I_c$ with I_c the critical current of each Josephson junction. The dot marks the working point of the SQUID, which is desirable to be kept within the linear region of the V-ϕ characteristic.

current corresponds to an integer number of flux quanta threading the loop and the minimum critical current corresponds to a half-integer number of flux quanta. Any small change in flux would then be measured as a change in voltage across the SQUID. The flux bias can be used to set the working point in the linear region of the $V - \phi$ characteristic. In order to remain within the linear region the coupled flux signals should not surpass values of about $\phi_o/10$.

3.2.2 SQUID system overview

The SQUID system consists of three main parts, namely, the pick-up circuit, the SQUID itself and the feedback electronics (see Figure 3.2). In this experiment we use a tuned pick-up circuit. This circuit resonates at a certain frequency and provides amplification over a narrow frequency band.

Tuned and Untuned Input circuits

A tuned pick-up or input circuit is a series resonant circuit which connects the NMR receiver coil with the input coil of the SQUID. It also contains a capacitor and a resistive element, both in series. In an untuned input circuit, on the other hand,

there is no capacitor and the receiver coil is directly connected to the input coil. The circuit is entirely superconducting and the conservation of flux implies that the SQUID measures the flux through the receiver coil. In such a case, since the input circuit is simply a flux transformer and not a resonant circuit, the spectrometer is called "broadband spectrometer". In a tuned input circuit, the voltage across the input coil depends upon the frequency as ω^2, whereas in a broadband spectrometer it is simply proportional to ω. The flux coupled to the SQUID has the same frequency dependence. On the other hand, the noise signal per unit bandwidth in the input circuit, arising from the small Johnson noise voltage across the resistor, obeys

$$< i_{\mathrm{N}}^2 >= \frac{4k_{\mathrm{B}}T}{R_{\mathrm{i}}}$$

where R_{i} is the dissipative element in the input circuit and T is the temperature. R_{i} can arise from a resistive component or from dissipation in the capacitor. The noise signal is due to thermally induced Brownian motion of the electrons in the metal. On resonance, we can write

$$< i_{\mathrm{N}}^2 >= \frac{4k_{\mathrm{B}}Q_{\mathrm{ip}}T}{\omega_{\mathrm{o}}L_{\mathrm{T}}} \tag{3.4}$$

where Q_{ip} is the quality factor of the input circuit and L_{T} the total inductance. The flux noise coupled to the SQUID will therefore be proportional to $\omega^{-1/2}$ and the SNR (Signal to Noise Ratio) will vary with the frequency as $\omega^{3/2}$. The signal current in the input circuit is proportional to the resonant frequency, as shown in Equation 3.17. In a broadband input circuit there is no resistor and, therefore, no Johnson white noise voltage across it. It follows that, since the SNR is linear for a broadband circuit and depends upon the frequency as $\omega^{3/2}$ for a tuned circuit, there will exist a frequency, ω_{c}, above which the SNR will be higher for a tuned spectrometer than

for an untuned one. This cut-off frequency depends on the lineshape of the sample and on the temperature of the input circuit. It also depends on the SQUID noise. For samples of $T_2^* = 1$ ms at 4.2 K it has been found that $f_c = \omega_c/2\pi \sim 1$ MHz and as the temperature of the input circuit is lowered ω_c decreases [52]. Since we will be working at relatively high fields (the Larmor frequency being about 1 MHz) the decision was to use a tuned input circuit to improve our sensitivity. Additional advantages of using a tuned input circuit are the de-emphasizing of white noise, the extra amplification factor $\sqrt{Q_{ip}}$ and the negligible response to low-frequency motion in the static magnetic field. On the other hand, in pulsed NMR, a tuned input circuit it is not the best choice for samples with very short T_2^*, since the ring down after a transmitter pulse would completely mask the sample decay. In the case of ^{3}He, T_2^* is of the order of ms and the tuned circuit is a safe choice provided the ring down time is of the order of μs. In our case, the ring down time constant was about 33 μs.

Flux-Locked Loop operation

The flux coupled to the SQUID through the input coil can take the working point out of the linear region if the flux signal is larger than $\phi_0/10$. Another issue is the existence of shifts in the operating point arising, for example, from the transient associated with the transmitter pulse. A Q-spoiler (see Section 3.3.1) can be used to overcome this problem. In order to avoid saturation caused by large signals the output is sent to a feedback coil via a series resistor R_f (see Figure 3.2). The feedback coil produces a flux equal and of opposite sign to the flux coupled to the SQUID, therefore keeping the working point unaltered. In this fashion the SQUID works as a null detector of flux. This operating method is called Flux-Locked Loop (FLL) and allows to measure changes in flux up to many flux quanta.

Noise in DC SQUID systems

Along with the NMR signal, an undesired amount of noise is detected when performing measurements. The noise in the DC SQUID comes from two sources: the Johnson white noise coming from thermal excitations of the electrons in the shunt resistors of the Josephson junctions and a frequency dependent noise which goes as $1/f$ and is due to fluctuations in the critical current of the Josephson junctions and to motion of the flux lines inside the SQUID ring. Generally the white noise dominates above just a few kHz and therefore we will not be concerned about the $1/f$ noise in these experiments.

The noise produces a rounding of the I-V characteristic due to a suppression of the critical current. That reduces the transfer coefficient V_ϕ (which is the slope of the $V - \phi$ characteristic at the working point). This should not be a serious issue unless the SQUID is subjected to a large external noise. The voltage noise spectral density and the flux noise spectral density are related by

$$< \phi_{\mathrm{N}}^2 >= \frac{< v_{\mathrm{N}}^2 >}{V_\phi^2}$$

where V_ϕ^2 is the SQUID transfer coefficient. If we add the preamplifier to the above equation we can get an expression for the total flux spectral noise density of the SQUID system

$$< \phi_{\mathrm{N}}^2 >=< \phi_{\mathrm{N,i}}^2 > + \frac{< V_{\mathrm{N}}^2 >}{V_\phi^2} \tag{3.5}$$

where $< \phi_{\mathrm{N,i}}^2 >$ is the intrinsic flux noise density of the SQUID and $< V_{\mathrm{N}}^2 >$ is the intrinsic voltage noise density of the preamplifier.

Noise temperature

The noise level of the SQUID system would ideally be dominated by the intrinsic noise of the SQUID. In practice, however, that only occurs below certain temperature, at which the Johnson noise of the resistor in the tuned input circuit becomes equal to the intrinsic noise of the SQUID. That temperature is called the *noise temperature* of the system. It is desired for the noise temperature to be as low as possible in order to obtain the better SNR. Certain parameters can be chosen in the input circuit to optimize the noise temperature.

In the input circuit of Figure 3.2 we can write for the current noise circulating in the SQUID

$$\phi_{\mathrm{N}} = I_{\mathrm{N}} L_{\mathrm{s}}$$

where L_{s} is the SQUID self-inductance. For the total flux in the SQUID we have then

$$\phi_{\mathrm{T}} = \phi_{\mathrm{N}} + M_{\mathrm{i}} I_{\mathrm{i}} = \phi_{\mathrm{N}} + M_{\mathrm{i}} \Big(\frac{V_{\mathrm{i}} - j\omega_0 M_{\mathrm{i}} I_{\mathrm{N}}}{Z_{\mathrm{i}}} \Big)$$

where ω_0 is the resonance frequency of the input coil, M_{i} is the mutual inductance between the SQUID and the input coil, V_{i} and I_{i} are the voltage across the input coil and the current through it, respectively, and Z_{i} is the total impedance of the input circuit. The input circuit resonance frequency is given by

$$\omega_0 = \left(\frac{1}{C_{\mathrm{i}}(L_{\mathrm{p}} + L_{\mathrm{i}})} \right)^{1/2}$$

where C_{i} is the capacitance of the input circuit, L_i is the self-inductance of the input coil and L_{p} the self-inductance of the receiver coil. And the quality factor is defined

by

$$Q_{\mathrm{ip}} = \frac{\omega_0(L_\mathrm{p} + L_\mathrm{i})}{R_\mathrm{i}} = \frac{1}{R_\mathrm{i}}\left(\frac{(L_\mathrm{p} + L_\mathrm{i})}{C_\mathrm{i}}\right)^{1/2}$$

We can define now the quantities

$$\alpha^2 = \frac{M_\mathrm{i}^2}{L_\mathrm{i}L_\mathrm{p}} \tag{3.6}$$

and

$$\alpha_{\mathrm{eff}}^2 = \frac{M_\mathrm{i}^2}{(L_\mathrm{p} + L_\mathrm{i})L_\mathrm{s}} = \alpha^2\Big(\frac{L_\mathrm{i}}{L_\mathrm{p} + L_\mathrm{i}}\Big)$$

where α is the coupling coefficient of the SQUID and input coil. Let us now separate the total flux into the signal flux and the effective noise flux:

$$\phi_\mathrm{s} = \frac{M_\mathrm{i}V_\mathrm{i}}{Z_\mathrm{i}} \quad \text{and} \quad \phi_{\mathrm{N,eff}} = \phi_\mathrm{N}\Big(1 - \frac{j\omega_\mathrm{o}M_\mathrm{i}^2}{Z_\mathrm{i}L_\mathrm{s}}\Big)$$

By comparing the effective noise flux with the noise at the resistor we can get an estimate of the relative importance of both noises. A resistor R_i at temperature T generates a noise current

$$< I_\mathrm{N}^2 >= \frac{4k_\mathrm{B}T}{R_\mathrm{i}}$$

which gives a voltage noise power of $(4k_\mathrm{B}T/R_\mathrm{i})M_\mathrm{i}^2V_\phi^2$. On the other hand, the mean square output noise voltage power on resonance per unit bandwidth can be obtained from the effective flux noise

$$< V_\mathrm{N}^2 >= V_\phi^2\Big(1 + \frac{\omega_\mathrm{o}^2M_\mathrm{i}^4}{R_\mathrm{i}^2L_\mathrm{s}^2}\Big) < \phi_\mathrm{N}^2 >$$

By applying the definition of noise temperature, we can now finally obtain an ex-

pression for it:

$$T_{\rm N} = \Big(\frac{R_{\rm i}}{4k_{\rm B}M_{\rm i}^2}\Big)\Big(1 + \frac{\omega_0^2 M_{\rm i}^4}{R_{\rm i}^2 L_{\rm s}^2}\Big) < \phi_{\rm N}^2 > \tag{3.7}$$

if we minimize $T_{\rm N}$ with respect to $(\omega_0 M_{\rm i}^2)/(R_{\rm i}L_{\rm s}) = x$, we find that the minimum noise temperature corresponds to $x = 1$. In other words, the optimum resistance is

$$(R_{\rm i})_{\rm opt} = \frac{\omega_0 M_{\rm i}^2}{L_{\rm s}}$$

Or, in other terms,

$$Q_{\rm ip}\,\alpha^2 \frac{L_{\rm i}}{L_{\rm i} + L_{\rm p}} = 1 \tag{3.8}$$

The optimum noise temperature is, therefore,

$$T_{\rm N} = \frac{< \phi_{\rm N}^2 > \omega_{\rm o}(L_{\rm i} + L_{\rm p})}{2k_{\rm B}M_{\rm i}^2 Q_{\rm ip}}$$

The parameters of the input circuit can be chosen, therefore, to optimize the noise temperature, making it as low as possible. In order to make an estimate of the optimum noise temperature for our SQUID, we could use Equations 3.6 and 3.8 and write

$$\frac{L_{\rm i} + L_{\rm p}}{M_{\rm i}^2 Q_{\rm ip}} = \frac{1}{L_{\rm s}}$$

which gives

$$T_{\rm N} = \frac{< \phi_{\rm N}^2 > \omega_{\rm o}}{2k_{\rm B}L_{\rm s}}$$

The intrinsic mean square flux noise per unit bandwidth for this SQUID is, at 1 kHz, $< \phi_{\rm N}^2 >= 1.14\mu\phi_{\rm o}^2{\rm Hz}^{-1}$ and the SQUID self-inductance $L_{\rm s} = 210$ pH. Those values give an optimum noise temperature of 6 mK at 1 MHz.

If we now consider the effect of the preamplifier, which has a voltage noise am-

plitude of $< V_N^2 >^{1/2} = 0.45\text{nV}/\sqrt{\text{Hz}}$ and a transfer coefficient of $V_\phi = 540.8\mu\text{V}/\phi_o$ and use Equation 3.5, we find an optimum noise temperature of 9.24 mK at 1 MHz.

Additional Positive Feedback

One major difficulty is the satisfactory matching of the SQUID to the room-temperature read-out electronics. A matching transformer could be used to equal the SQUID output impedance with the electronics input impedance, but this would significantly reduce the bandwidth of the system. One way to avoid the impedance matching circuit is to use a second SQUID as a preamplifier. This has the disadvantage of the additional wiring needed between the cryogenic environment and room temperature. Alternative read-out schemes which do not require cooled impedance matching circuits are a frequency modulated scheme and a directly coupled one [53].

Much simpler is to directly couple the output of the SQUID to the room temperature preamplifier. This is called the Direct Offset Integration Technique (DOIT) and it offers the possibility of achieving much higher bandwidths than matching transformers. However, the electronics could significantly reduce the SNR of the system if its noise is larger than the SQUID intrinsic noise. There are several solutions for this [54]. For this experiment we used a SQUID with Additional Positive Feedback (APF). The APF circuit consists of a resistor, R_a, and an inductance, L_a, coupled to the SQUID (see Figure 3.2) in such a way that the slope of the $V - \phi$ characteristic is increased at the working point with positive feedback. The net effect of this is that the noise *and* the signal coming from the SQUID are amplified by the same factor (the SNR from the SQUID is unchanged) and the noise from the SQUID does match more closely the noise produced by the output amplifier. This allows the SQUID output to be directly connected to a room temperature amplifier without the use of a matching transformer which would degrade the bandwidth of

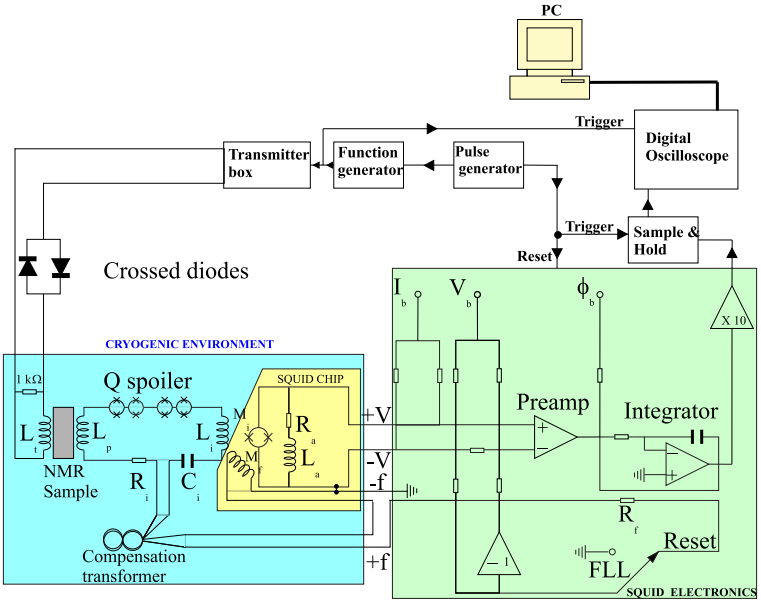

Figure 3.2: Schematics of the SQUID NMR spectrometer

the system.

For our spectrometer, the APF SQUID has an intrinsic white noise (at 1 kHz) of $< \phi^2_{N,i} >^{1/2} = 1.14\ \mu\phi_o/\sqrt{\text{Hz}}$ and a transfer coefficient at the working point of $V_\phi = 540.8\ \mu\phi_o/\sqrt{\text{Hz}}$ (see Table 3.3.2) and our room temperature output amplifier has an intrinsic voltage noise density of $< V^2_N >^{1/2} = 0.45\ \text{nV}/\sqrt{\text{Hz}}$. Using Equation 3.5 we find that the amplifier has an intrinsic flux noise density of $6.92 \times 10^{-13}\ \phi^2_o/\text{Hz}$ whereas the SQUID intrinsic flux noise is $1.3 \times 10^{-12}\ \phi^2_o/\text{Hz}$. Therefore, the amplifier does not significantly degrade the SNR.

3.3 Experimental setup

Figure 3.2 shows a setup of the SQUID NMR system used for this experiment. The SQUID, APF circuit and the feedback coil are integrated in a SQUID chip. The static field is provided by a superconducting NMR magnet located in the helium bath (see Appendix A), not shown in the Figure. The transmitter coil and the receiver coil

have their axes perpendicular to each other and both of them perpendicular to the axis of the NMR magnet to minimize any potential cross-coupling. The transmitter coil, along with the sample, the input circuit and the SQUID chip are in a cryogenic environment. The rest of the spectrometer operates at room temperature.

3.3.1 The input circuit and transmitter coil

The input circuit was tuned at a frequency of 963 kHz inside the cryostat. A single surface-mount 470 pF capacitor was used to resonate at a frequency somewhat near 970 kHz, a quiet place as far as magnetoacoustic noise was concerned (see Section 3.4.6). The Q of the input circuit, $Q_{\rm ip}$, was measured to be 100 ± 5. The copper receiver coil acted as the resistive element $R_{\rm i}$ of the input circuit. We can estimate the value of this resistance by

$$R_{\rm i} = \frac{\omega_0 L_{\rm t}}{Q_{\rm ip}} \sim 2.6\Omega$$

where $L_{\rm t}$ is the total inductance of the input circuit (42.68 μH). The rest of the components of the input circuit were the input coil, the Q-spoiler and the compensation transformer. Apart from the receiver coil, the components of the input circuit along with the SQUID chip carrier were located inside a cylindrical Nb shield designed to protect the SQUID from environmental magnetic noise. Several Nb superconducting pads deposited on a fibre board acted as connection points to which the different components of the input circuit were connected. This fibre board lay on a stycast holder which also gave support to the SQUID carrier. The assembly is shown in Figure 3.3. The Q-spoiler chip had two screw terminals through which it was connected to the Nb pads on the fibre board. Both, the compensation transformer and the input coil were located on the reverse of the stycast holder. A small hole drilled

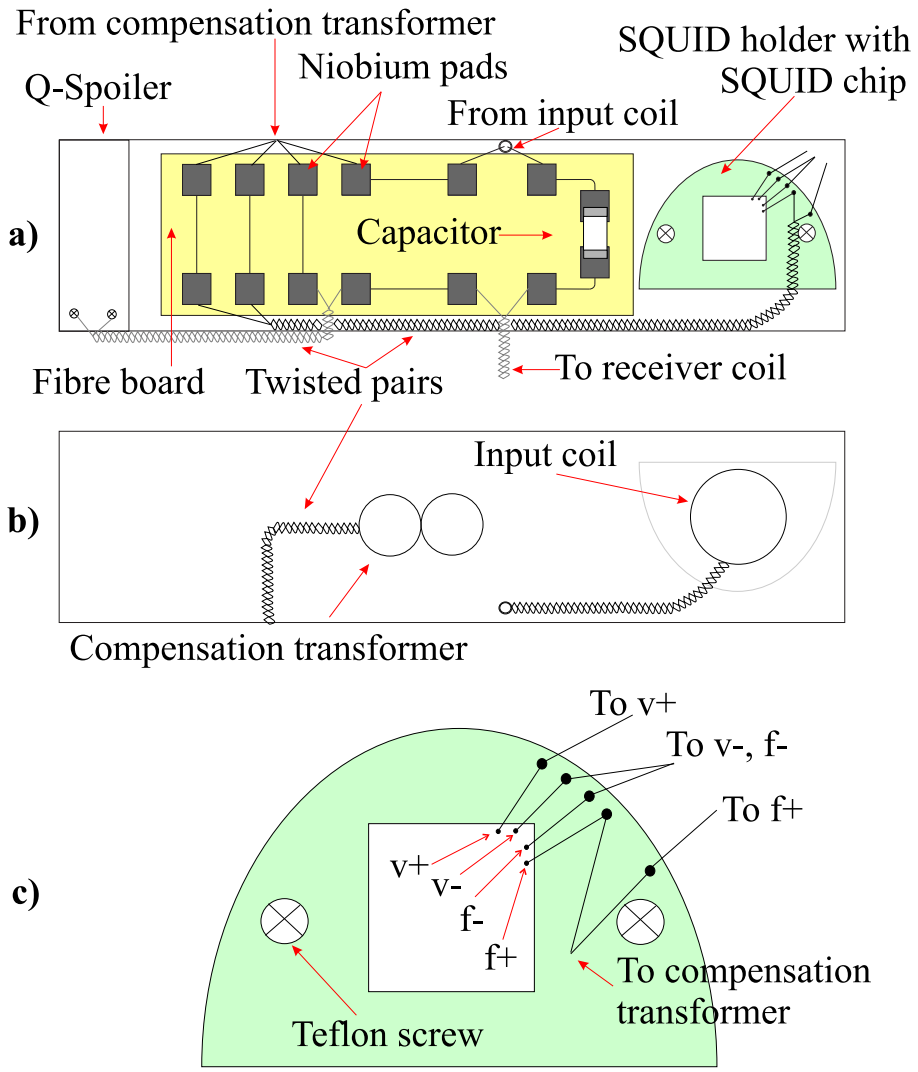

Figure 3.3: Input circuit and SQUID connections showing stycast holder front (a) and back (b)(not to scale). The yellow area represents the fibre board containing the Nb superconducting pads. A blow up of the SQUID chip is shown in (c), along with the SQUID connections.

on the stycast allowed the twisted pair coming from the input coil to be connected to the Nb pads.

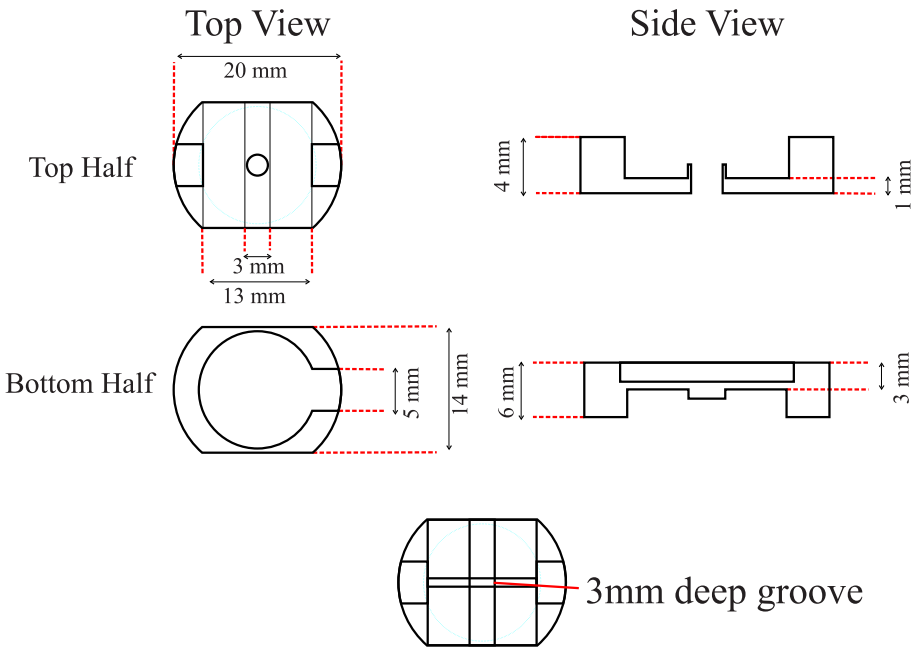

Figure 3.4: Top and Side views of both halves of the receiver coil former. The 3 mm deep groove in the bottom side of the lower half provides a path for the wiring to cross from one side to the other.

The receiver coil

The receiver coil, rectangular in shape, is wound around a coil former which encloses the experimental NMR cell. The receiver coil former is made out of Stycast 1266 and a rectangular shape was chosen over a circular one in order to improve the filling factor. The coil is split into two halves to allow some space for the cell's fill line. The wire used is enamelled copper wire, 44 SWG (80μm diameter), and the coil consists of 45 turns on each side of the fill line. This gives us a measured inductance of $L_{\mathrm{p}} = 37.9$ μH. Figure 3.4 depicts a sketch of the top and bottom halves of the receiver coil former. The lower half of the former presents a 3 mm deep groove in the bottom side to allow the wiring to cross from one side of the former to the other.

We can approximate the field:current ratio for an equivalent circular coil by the

expression

$$B_{\mathrm{r}} = \frac{\mu_{\mathrm{o}} N K}{l} \tag{3.9}$$

where K is an inhomogeneity factor referring to the fact that the solenoid is not infinite, $K = 1/[1 + 0.45(2a/l)]$, and l and a are the length and the radius of the solenoid, respectively. Taking a as the smallest possible radius of the solenoid, this is, the height of the coil, one can find $B_{\mathrm{r}} = 6.81$ mT/A. This parameter is very important since the NMR signal size is determined by the magnetic field inside the receiver coil. The copper leads coming from the receiver coil are heat sunk in a wedge-shaped plate at the lower end of the heat switch and soldered to CuNi clad NbTi leads which join the rest of the input circuit at the 4K plate. The room temperature resistance of the receiver coil was 18.3 Ω. Copper was chosen for the receiver coil in order to avoid the magnetic disturbances in the field homogeneity of the sample produced by superconducting wires.

The input coil

The "flip-chip" SQUID input coil is wound out of 106 μm Formvar CuNi clad NbTi wire. It is circular in shape with a diameter of 5.8 mm and it consists of 2×11 turns, one on top of the other. The reason of having two layers of wire is the higher inductance one can achieve in that way and, therefore, the higher mutual inductance between the input coil and the SQUID. In order to measure the inductance of the coil, it is connected to a LC circuit and the value of the capacitor is changed over a range which goes from 0 to 100 pF. For each value of the capacitor the resonant frequency is measured with a Vector Impedance Meter. By plotting $1/\omega^2$ against the capacitance and doing a linear fit we obtain a slope whose value is the desired inductance. The measured inductance of the coil is $L_{\mathrm{i}} = 4.78$ μH and the measured mutual inductance

with the SQUID is $M_{\mathrm{i}} = 2.27$ nH. The input coil is placed in a circular groove machined in the input circuit stycast holder (see Figure 3.3). It is intended to place it as close to the SQUID chip as possible in order to achieve maximum coupling. The leads from the input coil are soldered to two of the superconducting pads present on the fibre board.

The Q-Spoiler

Although the design of the transmitter and receiver coil is made to minimize any potential current in the receiver coil arising from the transmitter signal, cross-coupling does occur. This can have a harmful effect on the SQUID performance if large signals are coupled to the SQUID. In order to prevent that, a dynamic resistance is connected in series to the input circuit. This device is called a *Q-Spoiler* and it consists of a series of around twenty unshunted DC SQUIDs connected in series. A niobium control line running along the array is used to modulate the critical current of the device. While the current flowing through the Q-Spoiler is less than its critical current, the device behaves as a superconductor and has no effect on the input signal whatsoever. If the current exceeds the critical current of the Q-Spoiler, then it becomes resistive and the signal coupled to the SQUID is reduced sensibly. The critical current of the Q-Spoiler is controlled by a modulation coil. This critical current can take values between 20 and 40 μA for our particular Q-spoiler, as shown in Figure 3.5. The resistance in the normal state is 400 Ω.

The ring down time of the input circuit following the removal of the transmitter pulse is given by

$$\tau = \frac{2Q_{\mathrm{ip}}}{\omega_{\mathrm{o}}}$$

For our values of $Q_{\mathrm{ip}} \sim 100$ and $f_{\mathrm{o}} = 963$ kHz, our ring down time constant was

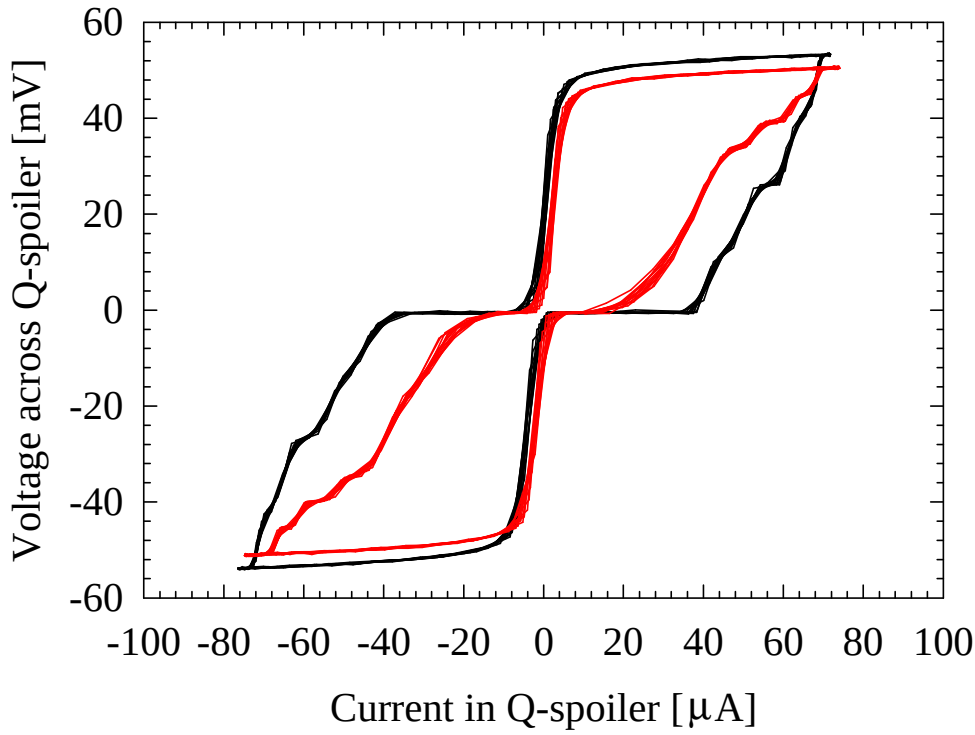

Figure 3.5: The Q-spoiler I-V characteristic. The maximum (black line) and minimum (red line) critical currents are 40 and 20 μA, respectively. The device has a normal state resistance of 400 Ω.

about 33 μs. Due to the fact that ^{3}He has a T_2^* of the order of ms, much larger than the ring down time, it was not necessary to minimize the Q-Spoiler critical current with the modulation line during these experiments.

The Q-spoiler used in this experiment was supplied by STAR Cryoelectronics.

The compensation transformer

We found that the signal fed back to the SQUID via the feedback coil was also coupled to the input coil and gave rise to a number of undesirable effects, such as

the dependence of the input circuit Q on the value of the feedback resistance, R_{f}. The system white noise was also found to vary with R_{f}. In order to get rid of those effects we use a compensation transformer. This consists of two superconducting twisted pairs twisted around each other forming an eight-shaped figure. Each of the loops of the eight-shaped outline has a radius of 3 mm. One of the twisted pairs is connected to the input circuit using the superconducting pads whereas the other is connected in series to the feedback loop via the f_+ terminal on the SQUID chip and to the room temperature preamplifier (see Figures 3.2 and 3.3). The current flowing through the twisted pair connected to the feedback coil induces a current equal and of opposite sign in the twisted pair connected to the input circuit. The compensation voltage across R_{i}, therefore, is equal and opposite in sign to the induced voltage in the input coil coming from the feedback coil. It is important to connect the compensation transformer in the correct way around to get the desired effect. This is identified by performing a set of measurements of the input circuit Q factor with different feedback resistors and observing any potential oscillations on it. These measurements were made on a transport dewar outside the fridge and are shown in tables 3.1 and 3.2 We can see in Table 3.1 that the Q is strongly dependent

Feedback Resistor	Q_{ip} measured
$2 \times 1k\Omega$	634.80
$2 \times 2.2k\Omega$	2518.26
$2 \times 4.7k\Omega$	369.01

Table 3.1: Q dependence on feedback resistors with compensation transformer in first way around

on the value of the feedback resistor. The behaviour is not linear, either, since the Q is four times larger with a pair of 2.2 kΩ feedback resistors than with a pair of 1.1 kΩ and for two 4.7 kΩ feedback resistors it has about half the value it had for

Feedback Resistor	Q_{ip} measured
$2 \times 470\Omega$	124.98
$2 \times 1k\Omega$	113.17
Open Loop (Shallow side)	141.27
Open Loop (Steep side)	141.65

Table 3.2: Q dependence on feedback resistors with compensation transformer in second way around

the pair of 1.1 kΩ. Changing the compensation transformer the other way around we observed a much more stable behaviour of the Q, with a value of the expected order for the input circuit. This was the way around chosen for the compensation transformer.

The transmitter coil

The transmitter coil is wound in a saddle geometry around a MACOR former and glued using black 2651 Stycast. The coil is made out of CuNi clad NbTi wire with 106 μm total diameter and it consists of 15 turns on each side of the saddle, with a 120^o angle in each circular arc. It is 44 mm long with a diameter 22 mm. The length being double the diameter provides the best field homogeneity at the center of the coil [55]. For a saddle coil with N turns, radius r and length $2l$, the field:current ratio is given by [55]

$$B_{\text{t}} = \frac{N\mu_{\text{o}}\sqrt{3}}{\pi}\left(\frac{rl}{(r^2+l^2)^{3/2}} + \frac{l}{r(r^2+l^2)^{1/2}}\right) \tag{3.10}$$

For our transmitter coil we found $B = 1.015$ mT/A. Its measured inductance was 53.3 μH. The leads from the transmitter coil are heat sunk at the mixing chamber plate and then again at the 4 K plate before entering the dipper probe (see Section 3.3.4).

3.3.2 The W9 series SQUID

The SQUID used throughout this work was made at PTB in Germany. The SQUID chip contained an integrated APF coil and was deposited on a plastic chip carrier, where four Nb pads gave access to the SQUID points $V+$, $V-$, $f+$ and $f-$ (Figure 3.3 c). The SQUID was first tested in a transport dewar outside the cryostat. It was

Parameter	**Label**	**W9M-6w/957-C51**
Maximum critical current	I_{c}	4.85 μA
Modulation depth for minimum noise	ΔV	38.9 μV
SQUID gain at working point	V_ϕ	540.8 $\mu V/\phi_{\mathrm{o}}$
Flux noise at 1 kHz	$<\phi^2_{\mathrm{N,i}}>^{1/2}$	1.14 $\mu\phi_{\mathrm{o}}/\sqrt{Hz}$
SQUID self-inductance	L_{s}	210 pH

Table 3.3: SQUID parameters at 4.2 K as measured at PTB

operated from a control box connected to the room temperature read-out electronics. A set of BNC sockets provided connections to the current, voltage and flux bias and to the FLL switch. The box also allowed to manually change between Reset and FLL modes by mean of a switch. For every BNC socket a knob could be used to adjust the current applied to the socket. In Reset mode the DC voltage and current offsets could also be adjusted using another two knobs to provide zero voltage across the SQUID and zero current through it.

Figure 3.6 shows the measured I-V and V-ϕ characteristics of our SQUID. In order to measure the SQUID I-V characteristic a low frequency (64 Hz) sine wave was applied to the current bias through the BNC socket in the SQUID control box. By adjusting the ϕ_{bias} pot the critical current was set to its maximum. The V-ϕ characteristic could be viewed by applying the same signal to the ϕ_{bias} socket. The I_{bias} pot was adjusted to obtain the maximum amplitude in the $V-\phi$ characteristic. The V_{bias} and ϕ_{bias} pots were likewise adjusted to establish the working point.

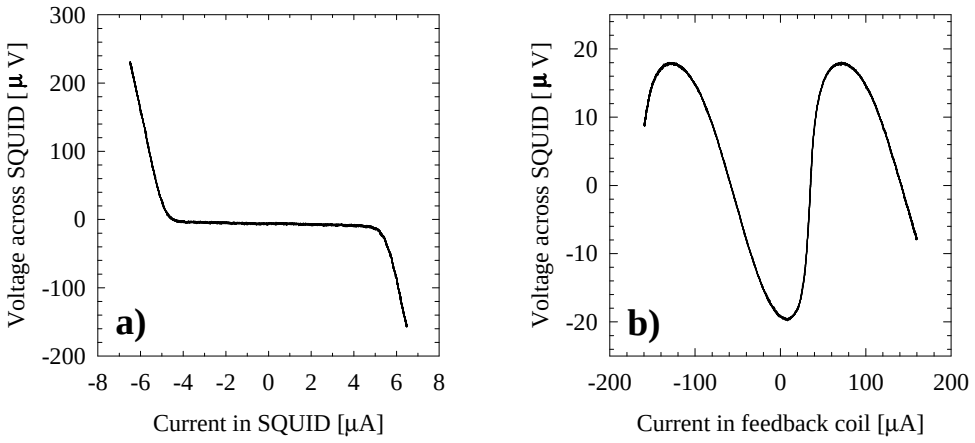

Figure 3.6: SQUID I-V (a) and V-ϕ (b) characteristics as measured in a transport dewar at 4.2 K

While measuring the characteristics, the SQUID was operated in open loop with the feedback resistor removed in order to prevent any effect from the feedback circuit.

Prior to the experimental work inside the fridge, the spectral noise of the SQUID system was tested in a transport dewar in order to adjust the optimal value of the feedback resistor R_{f}. A dummy receiver coil was used to mimic the actual receiver coil later used in the experiment. An inductance of 76.94 μH was measured for this receiver coil and the input circuit resonant frequency was 820 kHz. The capacitor used in the transport dewar had a value of 477 pF. The noise spectrum was captured with a spectrum analyzer from DC to 10 MHz for three different values of feedback resistors with the electronics in FLL mode. Figure 3.7 shows the spectral noise for 2 $\times$ 1.1 kΩ (red), 2 $\times$ 2.2 kΩ (blue) and 2 $\times$ 4.7 kΩ (black). The system

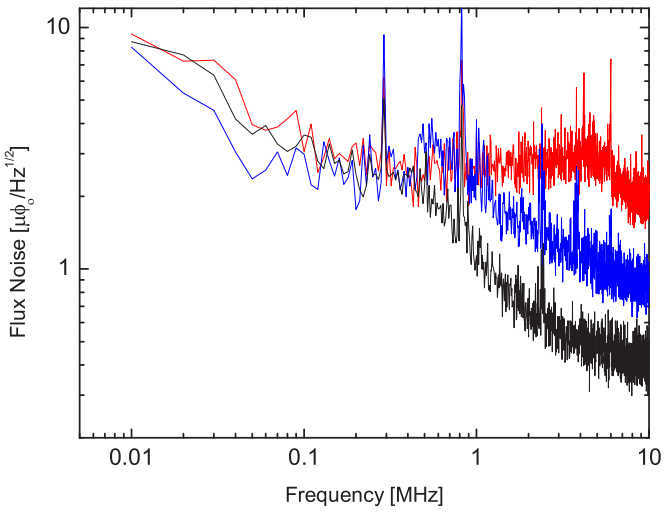

Figure 3.7: The SQUID system noise spectrum for 2 × 1.1 kΩ (red), 2 × 2.2 kΩ (blue) and 2 × 4.7 kΩ (black) feedback resistors

bandwidth showed a dependence on the value of the feedback resistor, whereas the magnitude of the noise peak and the system white noise seemed to be independent of R_f. The bandwidth decreased with increasing values of R_f, as expected [54]. It was also attempted to measure the system response with 2 × 470 Ω feedback resistors, but the feedback loop did not hold lock (at the time of writing, the cause of this problem is not completely understood). Therefore, the choice was made to use 2 × 1.1 kΩ feedback resistors in order to get the highest possible bandwidth (which was measured to be 5 MHz).

With the SQUID spectrometer inside the cryostat the noise flux density was measured for a number of different temperatures of the input circuit. As we can see in Figure 3.8, the magnitude of the noise peak decreases with $\sqrt{T}$, indicating that the measured noise is Johnson noise due to the resistance of the input circuit. If we extrapolate the data to zero flux density we can infer a noise temperature of the system of $T_N \approx 800$ mK. This means that below 800 mK the output noise

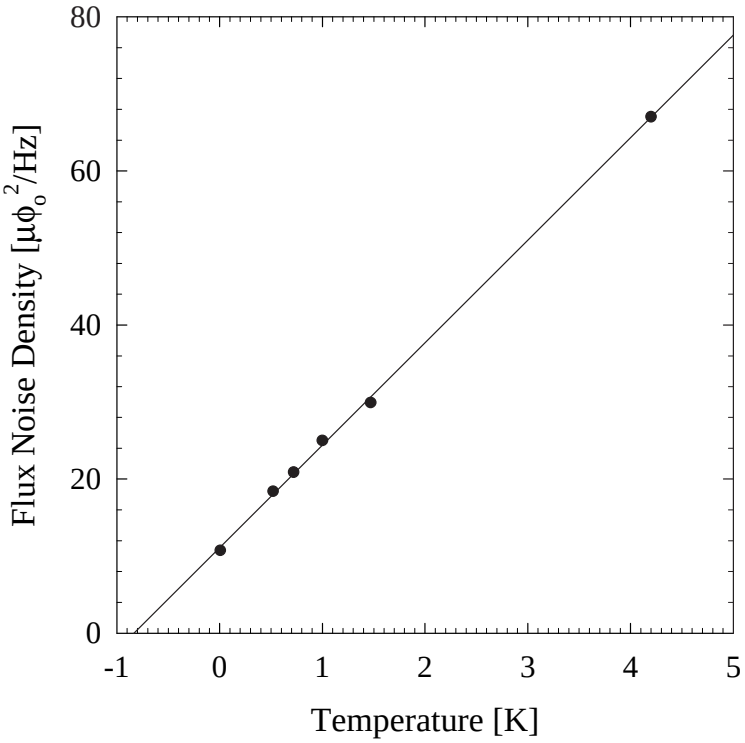

Figure 3.8: Flux noise density of the noise peak as a function of temperature. The extrapolated linear fit shows a noise temperature $T_{\mathrm{N}} \approx 800$ mK

was dominated by the SQUID intrinsic noise and the SNR did not benefit from subsequent cooling of the receiver coil.

One could now use Equation 3.7 and our spectrometer parameters to calculate the noise temperature we should be measuring (which is *not* the optimum noise temperature since the parameter $x = (\omega_{\mathrm{o}} M_{\mathrm{i}}^2)/(R_{\mathrm{i}} L_{\mathrm{s}})$ was not set to 1). Using $R_{\mathrm{i}} = 2.6\Omega$, $M_{\mathrm{i}} = 2.27$ nH, $L_{\mathrm{s}} = 210$ pH, $f_{\mathrm{o}} = 965$ kHz and $< \phi_{\mathrm{N}}^2 >^{1/2} = 1.41 \mu\phi_{\mathrm{o}}/\sqrt{\mathrm{Hz}}$ (including the effect of the preamplifier) we obtain a noise temperature of $T_{\mathrm{N}} = 78$ mK. It is evident that the measured noise temperature far exceeds the calculated noise temperature. We measured the SQUID noise at 100 kHz in the cryostat and obtained$< \phi_{\mathrm{N}}^2 >^{1/2} = 1.49\ \mu\phi_{\mathrm{o}}/\sqrt{\mathrm{Hz}}$, which agrees with the value provided by the SQUID manufacturer ($1.41\ \mu\phi_{\mathrm{o}}/\sqrt{\mathrm{Hz}}$ with our preamplifier). The disagreement

between the measured and calculated noise temperatures could be due to the effect of a spurious resistance in the input circuit, or some capacitive or inductive coupling to the SQUID. One potential candidate for these couplings was the APF circuit. In order to further investigate this issue, we made measurements in a transport dewar on two different SQUIDs: one with and one without APF. We used a high Q tank circuit with a superconducting receiver coil. The use of a superconducting receiver coil would make easier to identify the effect of any spurious resistance in the input circuit. In the SQUID with APF we measured a Q of 200 at a resonant frequency of 1.6 MHz. Since now the total inductance of the input circuit was 16.3 μH, this gave a resistance of 0.844 Ω. The Q was also found to decay by a factor of two at the steep side of the V-ϕ characteristic. This could be an effect of the APF. In the SQUID without APF, however, our Q was 600 and the input circuit resistance was 0.08 Ω. Also, the Q was not varying when we changed the SQUID working point from one side of the V-ϕ characteristic to the other.

These measurements suggested that the reason for the high noise temperature measured inside the cryostat could be the APF circuit. Although we could clearly see ^{3}He NMR signals with our spectrometer, as shown in Section 3.5, future work on this experiment will probably imply the use of a SQUID without APF.

3.3.3 The room temperature read-out electronics

The room temperature read-out electronics were designed by Dr. D. Drung from PTB, Berlin and have been described elsewhere [56]. They consisted of a integrated unit shielded in a brass can. The feedback resistors could be plugged in the circuit through four pin connectors. The electronics were connected to a 9-way Fischer connector on the top of the dipper probe. We used the electronics set XF2-HTS

M3, which provided an open FLL gain of 0.4194 $V\phi_o^{-1}$ for 2×1 kΩ feedback resistors and a preamplifier noise of 0.7 $nV/\sqrt{Hz}$. An extra amplifier following the FLL output provided an additional gain of 10.

3.3.4 The dipper probe

The SQUID shield and the wiring connecting the SQUID to the room temperature electronics were located on a dipper probe which entered the cryostat through one of the line-of-sight 40 mm diameter access ports. The probe runs through a stainless steel vacuum tube welded to the 4K flange. At the top of the probe there is a NW40 sealed brass plate with two NW10 sealed connectors for a SQUID box and the transmitter coil. The top plate is connected to the 4K flange by means of M4 stainless steel studding. A series of copper baffles are located all along the length of the studding in order to reduce the radiative heat leak coming from room temperature. The conductive heat leak is reduced by breaking the studding with three teflon rods. Two twisted pairs of 44 SWG copper wire join the SQUID box with a heat sink post at the 4 K flange. At the heat sink the copper wires are soldered to superconducting wire which is then connected to the superconducting pads in the SQUID chip carrier. Another copper twisted pair for the transmitter coil runs down the probe and is heat sunk above and below the teflon rods and then to a different post at the 4 K plate. Both heat sink posts are covered with cigarette paper to avoid the grounding of the sunk wires. At the 4K plate there is a 1 kΩ resistor soldered across the transmitter coil twisted pair acting as a high frequency filter with a cut off frequency of $\sim$ 3 MHz. Both heat sink posts are covered in aluminium foil and copper tape for shielding. The wiring coming from room temperature runs inside teflon in 1.6 mm stainless steel tubing. The last copper baffle provides support for

the two heat sink posts and for two M2 stainless steel studding which connect the SQUID plate to the probe.

3.3.5 Pulsing the system

The pulse sequencer used to obtain our NMR data is sketched in Figure 3.2. Prior to the pulse, the NMR static field is set at 29.75 mT, corresponding to a ^{3}He Larmor frequency of 965 kHz. Then, a short burst of 150 cycles of a 965 kHz sine wave is applied to the transmitter coil via a room temperature transmitter box containing two crossed diodes in series to block low-level noise. An Agilent 15 MHz function generator model 33120A is used to produce the burst and to trigger the oscilloscope. The Agilent is triggered by a home made pulse generator programmed by Dr. Tom Crane. This pulse generator has several boards whose parameters can be changed independently and it also makes possible to set any desired delay time between the pulses. The pulse generator also triggers a sample and hold unit and the reset-FLL switch in the read-out electronics (the FLL is opened during the transmitter pulse in order to avoid saturation). The object of the sample and hold is to remove the DC level coming from the activation of the FLL. This DC level is different each time due to a different number of flux quanta threading the SQUID loop. After the triggering from the pulse generator, the sample and hold allows also DC to pass through. As a side effect, the sample and hold also affects the bandwidth of the system (our particular unit has a bandwidth of ∼800 kHz, so the bandwidth of the system is reduced) and the output gain. This gain change is frequency dependent and, for our 965 kHz, it corresponds to a factor of 0.473.

The transmitter pulse could easily saturate the feedback electronics. The SQUID is, therefore, left in reset mode until 250 μs after the pulse is finished. 50 μs after the

activation of FLL, the pulse generator triggers the sample and hold, thus ensuring that the captured data contain zero DC offset. The FLL is activated for 50 ms. A delay of 460 μs between the triggering and the beginning of the data acquisition is set in the oscilloscope. The capture length in the oscilloscope is 2400 divisions, each division being 10 μs. The capture time is, therefore, 24 ms. It is recommended in pulsed NMR to have capture times of, at least, $5T_2^*$ in order to avoid signal distortion.

The transverse relaxation of the spins is due to variations of the local magnetic field over the sample. Spins that are not stationary (like those from a gas or a bulk liquid) would perceive larger variations of the local field. The time average of those variations would translate into a smaller spread of fields interacting with each spin, i. e. each spin would feel a more homogeneous field (and, therefore, a larger T_2^* than stationary spins). As a result, spins in a slab geometry show a smaller T_2^* than spins in bulk. At the lowest temperatures attained, T_2^* was of the order of 1 ms, making our capture time long enough for our purposes.

The NMR pulse could certainly induce eddy currents in the metallic substrate of the cell. An eddy current is a phenomenon caused by a moving magnetic field intersecting a conductor or vice-versa. The relative motion causes a circulating flow of electrons, or current, within the conductor. These circulating currents create magnetic fields that oppose the change in the external magnetic field. The current circulation can result in Joule heating of the substrate. For a rectangular metallic sheet of thickness t, the heating per unit area due to a magnetic field B in the plane of the sheet follows [57]

$$\frac{\dot{Q}}{A} = \frac{\omega\delta}{2\mu_0} B^2 \left[\frac{\sinh(t/\delta) - \sin(t/\delta)}{\cosh(t/\delta) + \cos(t/\delta)} \right] \tag{3.11}$$

where ω is the field frequency and δ is a characteristic length called the skin depth

$$\delta = \left(\frac{2\rho}{\omega\mu_0}\right)^{1/2}$$

with ρ the resistivity of the metal. The skin depth gives a measure of the length scale over which the magnetic field decreases in strength within the metal. Residual Resistance Ratios (RRR) of similar silver samples have been measured in the past giving values of about ∼300. This gives a resistivity at 4.2 K of $\rho = 5.74 \times 10^{-11} \quad \Omega\mathrm{m}^{-1}$. From the definition of skin depth we obtain, at 1 MHz, $\delta = 3.8\mu$m, which is much less than the 1 mm thickness of our silver substrate.

The 90^o pulse required a transmitter current of 112 mA during 155 μs (see Section 3.4.5). Using Equation 3.10 we find that such a transmitter pulse provides a magnetic field of 0.114 mT. According now to Equation 3.11 that magnetic field dissipates a power per unit area of 0.12 W/m^2 during the 155 μs pulse. For our two 13 mm diameter silver discs, therefore, the total power dissipated is 31.8 μW for each 155 μs pulse, or, in other words, 4.92 nJ dissipated per pulse. If we were to pulse every second, that would average a total heat leak of 4.92 nW. Note that the heat transfer to the sample would only happen *after the spins are tipped*, which means that the signal we obtain is the state of the spins at the pre-pulse temperature.

In order to reduce this heat leak as much as possible, the pulse size used during these measurements was equivalent to a $\sim 20^\circ$ tipping pulse (25 mA in the transmitter current and 0.24 nJ dissipated per pulse). Below 1 mK the pulse rate was kept at 1 pulse every 30 seconds, corresponding altogether to a heat leak of 8 pW.

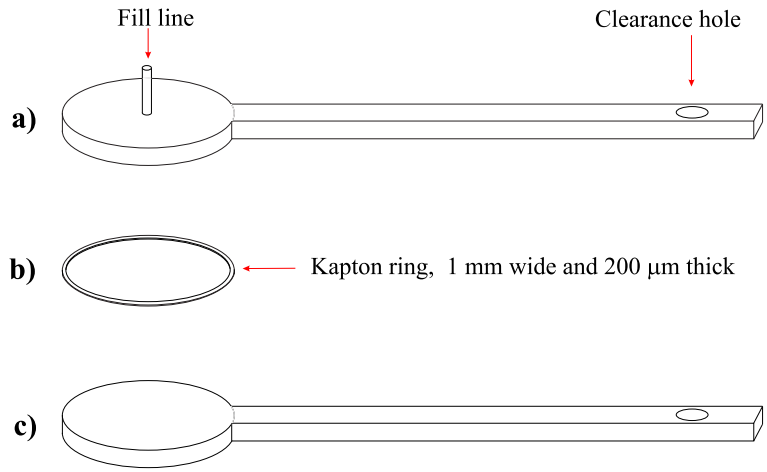

Figure 3.9: Sketch of the assembly of the experimental NMR cell (not to scale). A Kapton ring (b) provides the spacing between the top (a) and bottom (c) silver surfaces. See text for further explanation.

3.4 The experimental NMR cell

The study of thin films of ^{3}He presents severe experimental complications such as the small number of quasiparticles involved in the measurements and the stability of the sample. The NMR cell used for this experiment is designed to overcome those difficulties. Figure 3.10 shows a sketch of both halves of the experimental cell as well as the assembly of the fill line to the top surface whereas the general assembly of the cell surfaces can be seen in Figure 3.9. The ^{3}He quasiparticles are adsorbed on two 1 mm thick circular silver surfaces which form the top and bottom of the cell. A Kapton ring with the same OD as the diameter of the cell, 1 mm wide and 200 μm thick provides the spacing between both surfaces. The bonding of the two halves of the cell is attained by painting both sides of the Kapton ring with Stycast 2651 and letting the assembly to dry out. Once the epoxy is dry, the edges of the Kapton ring are likewise painted with the same Stycast. From each surface of the cell a 5 mm wide, 24 mm long rectangular tab emerges in order to provide a thermal link to the nuclear stage. The circular surfaces where the ^{3}He is adsorbed have a

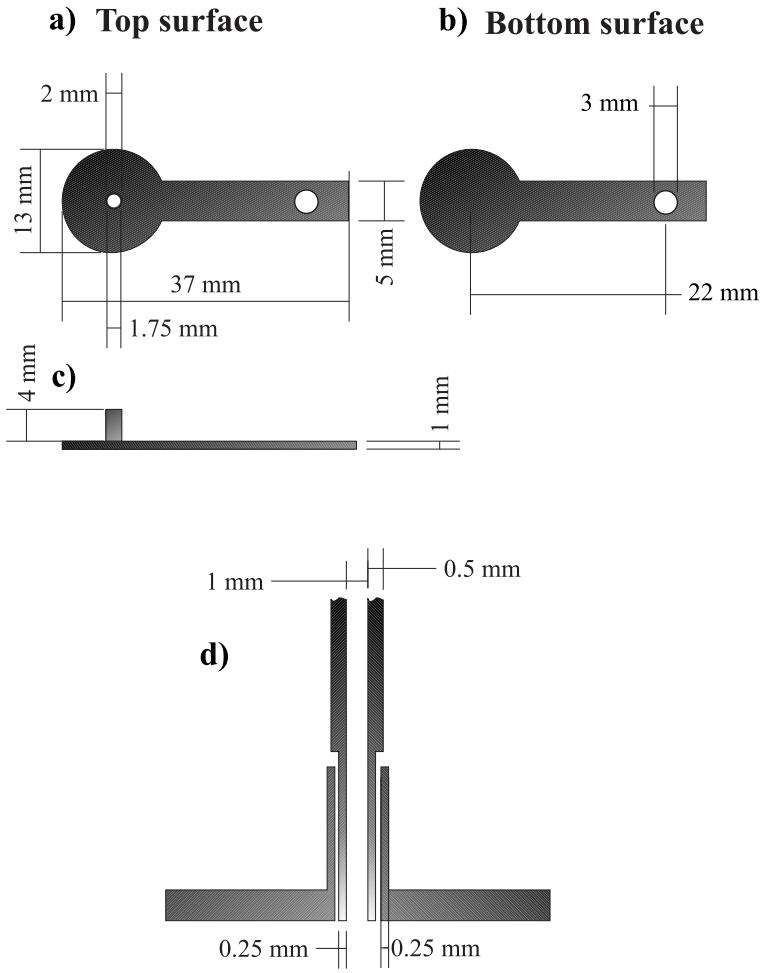

Figure 3.10: Design of the experimental NMR cell with fill line. a) Top view of the top surface. b) Top view of the bottom surface. c) Side view of the top surface. d) Longitudinal section of top surface showing assembly with thick silver tube

diameter of 13 mm, making the total length of each surface 37 mm. The diameter of the adsorbing surfaces was chosen as a compromise to maximize the surface area of the experimental sample and keeping it within the high homogeneity region of the NMR magnet. In order to allow ^{3}He inside the cavity, the top surface presents a hollow tube. The tube and the silver disc form a single piece of metal. This tube is 4 mm long with 2 mm OD and 1.75 mm ID and is attached to another silver tube, 60 mm long, with 2 mm OD and 1 mm ID. The attachment is made by thinning

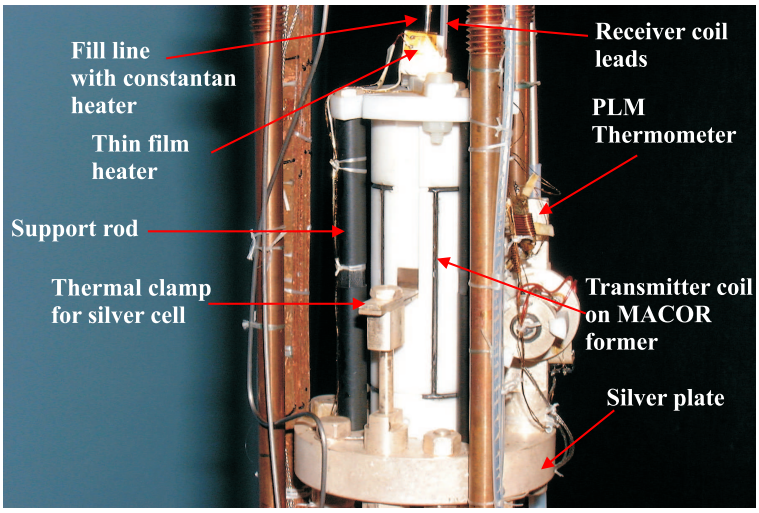

Figure 3.11: The NMR cell with transmitter and receiver coils set mounted on the silver plate.

the thicker tube, as depicted in Figure 3.10, and inserting it inside the thinner tube. This is done in such a way that a small length of the inner tube appears through the bottom side of the top silver surface. A 0.5 mm diameter 72Ag28Cu brazing wire is placed around the gap between the inner tube and the silver disc and the set is taken to 830 °C for five minutes. After the brazing is made, the extra length of the inner silver tube is machined away. The thicker silver tube joins on to a 0.15 mm ID CuNi tube which runs up to the room temperature gas handling system. Since it is needed to avoid condensation of the liquid inside the fill line, a heater made from 44 SWG constantan wire is employed below the cold plate (which operates at ∼60 mK) to wrap around the fill line. The fill line is also weakly thermally linked to the cold plate and mixing chamber plate of the cryostat. A thin film resistor provides yet another way of applying heat to the fill line. This resistor is attached to the fill line just outside the MACOR transmitter coil former, as shown in Figure 3.11.

There are several reasons behind the choice of silver as a substrate. First of all, it is a high-conductivity metal in order to minimize thermal gradients, particularly

those arising from heating associated with NMR pulses. Note that the ^{3}He sample is cooled down through an area of ~ 1 cm^2 and this boundary dominates the thermal resistance between it and the nuclear surface. Silver has a smaller nuclear heat capacity than copper, making it easier to cool down well below 1 mK, and the magnetoacoustic resonances following a NMR pulse are not as intense as those in copper [58]. Silver is used in both surfaces in order to avoid temperature gradients within the cell which could lead to internal flow of ^{3}He due to the thermomechanical effect [38] of the normal liquid, as observed in the previous cell used by Dyball [51].

The whole NMR cell assembly, comprising the transmitter coil MACOR former and the NMR cell enclosed by the receiver coil stycast holder, sit on a 10 mm thick silver plate connected thermally to the nuclear stage by a 10 mm diameter silver rod. This silver rod serves also as mechanical support. The NMR cell rectangular tabs present a M3 clearance hole at 22 mm from the centre of the circular surface through which a silver post runs providing thermal link with the experimental silver plate by means of a cone joint. A 200 μm thick silver washer is used between the tabs at the M3 clearance hole. The PLM thermometer is also mounted on this silver plate. A silver holder acts as a mechanical support for the thermometer. This silver holder is clamped to a silver post connected to the silver plate and thus providing a thermal link with the nuclear stage. Figure 3.11 shows the assembled NMR set in the experimental area along with the PLM thermometer.

3.4.1 Preparation of the metallic surfaces

Prior to the assembly of the cell, the silver surfaces needed to be mechanically polished and characterized. The polishing was carried out using a Buehler Minimet 1000 polishing machine. The surfaces to be polished were attached to a brass holder

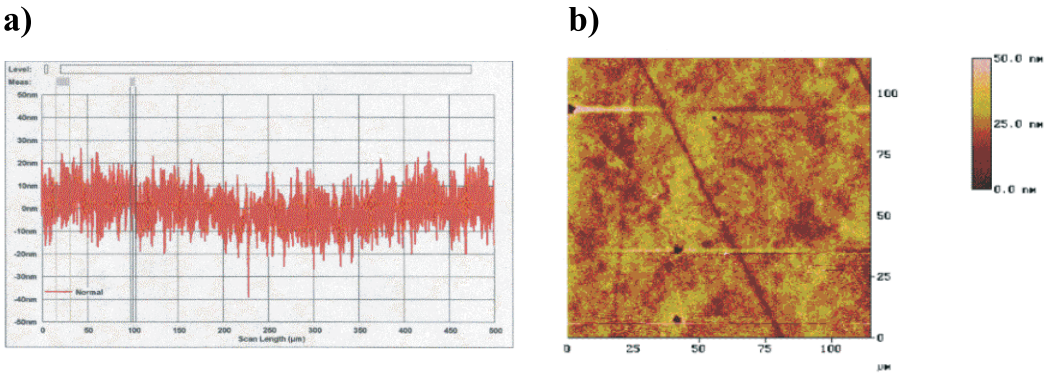

Figure 3.12: Surface characterisation as measured by a Tencor Profilometer (a) and by an Atomic Force Microscope (AFM)(b).

using wax. First, each surface was "roughed" down using grit paper. Then, the brass holder was attached to the polishing machine. The surfaces were polished using diamond paste and water as a lubricant. The diamond paste was progressively reduced in size, from 9 μm grit size to 3 μm and, finally to 1 μm. After this last stage, the final polish was made using a solution of Al_2O_3 which had a particle size of 0.05 μm. This polishing method enabled us to achieve a measured surface roughness of $\pm$ 10 nm, as shown in Figure 3.12.

3.4.2 Top and Bottom Films

Liquid ^{3}He is ideally adsorbed on the silver surfaces of the cell forming two uniform films, one at the top surface and one at the bottom surface. A state of equilibrium is reached in which the chemical potential of both film surfaces is the same. The liquid is bound to the surfaces by van der Waals forces, which arise from the fluctuating dipole moments of the atoms. Near the absorption surface the van der Waals potential has the form $-C_3 d^{-3}$, where C_3 is a constant describing the strength of the long-range van der Waals interaction and d is the thickness of the ^{3}He film.

However, for thicker films, a retardation effect takes place and the van der Waals potential for a film of thickness d can be written as [59]

$$V_{\text{retarded}}(d) = -\gamma_{\text{o}} \frac{d_{\text{o}}}{1.4} \frac{1}{d^4}$$

where γ_{o} and d_{o} are constants that depend both on the liquid and on the substrate. For ^{4}He adsorbed on gold, d_{o} has a value of 160 Å and γ_{o} has a value of 3100 k_{B} Å^3 [59]. We will use those values for this discussion. Note that the retardation effect only occurs for films of thickness much larger than d_{o}. We can, therefore, write

$$-\gamma_{\text{o}} \frac{d_{\text{o}}}{1.4} \frac{1}{d_{\text{b}}^4} = -\gamma_{\text{o}} \frac{d_{\text{o}}}{1.4} \frac{1}{d_{\text{t}}^4} + mgh \tag{3.12}$$

where d_{b} and d_{t} are the film thicknesses at the bottom and the top of the cell, respectively, m is the mass of a ^{3}He atom and h is the height of our cell, in this case, 200 μm. We use now the values of γ_{o} and d_{o} and find that

$$\frac{1}{d_{\text{t}}^4} - \frac{1}{d_{\text{b}}^4} = 2.02 \times 10^{-12} \text{Å}^{-4}$$

Therefore, when $d_{\text{b}} \to \infty$, $d_{\text{t}} \to 840$ Å. This is the maximum possible thickness on the top surface. We will define $d_{\text{TOTAL}} = d_{\text{t}} + d_{\text{b}}$ and $d_{\text{M}} = 84$ nm. We have then that

$$\frac{1}{d_{\text{t}}^4} = \frac{1}{d_{\text{b}}^4} + \frac{1}{d_{\text{M}}^4}$$

and thus

$$d_{\text{t}} = d_{\text{b}} \Big(1 + \frac{d_{\text{b}}^4}{d_{\text{M}}^4} \Big)^{-1/4} \tag{3.13}$$

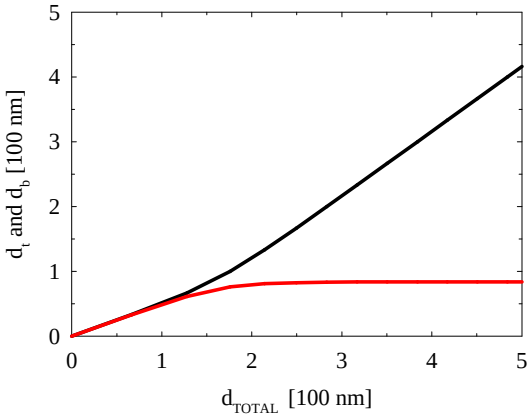

Figure 3.13: The thickness of top (red) and bottom (black) films within the NMR cell as a function of the total thickness for a cell height of 200 μm

We can also express the total thickness as

$$d_{\mathrm{TOTAL}} = d_{\mathrm{b}}\left[1 + \left(1 + \frac{d_{\mathrm{b}}^4}{d_{\mathrm{M}}^4}\right)^{-1/4}\right] \tag{3.14}$$

By using Equations 3.13 and 3.14 we can relate each of both films to the total thickness. This is shown in Figure 3.13. We can observe that up to about 50 nm both films increase at the same rate. Above 50 nm, however, gravity starts to make increasingly difficult the adsorption of liquid in the top film. For a 150 nm thick film on the bottom surface, the top film has already reached its maximum of 84 nm.

This model did not take into account the possibility of capillary condensation of the liquid in the corners of the cell. Another analysis is presented in Section 4.2.1 in which the film surface energy is considered, although there the non-retarded potential is used to investigate the possibility of capillary condensation for thin films. In the NMR cell, the stycast used to bond the top and bottom halves could form a curved surface in which the ^{3}He could adsorb smoothly forming a constant thickness

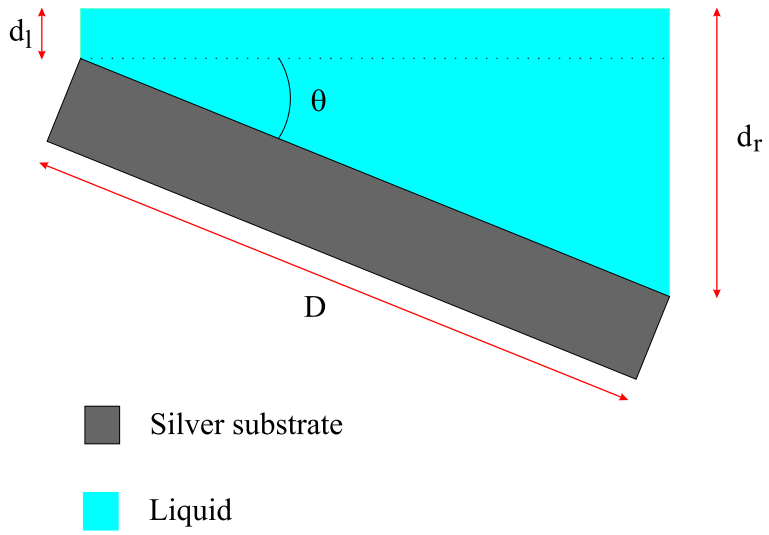

Figure 3.14: Film distribution over the substrate for a tilted cell

film all over the cavity. The NMR data presented in the next section did not show clear signatures of capillary condensed liquid in the corners.

3.4.3 Effect of the tilt

If the silver surfaces are not absolutely levelled, the thickness of each film will vary throughout the substrate. We can study this effect by writing an equation similar to Equation 3.12

$$-\gamma_o \frac{d_o}{1.4}\frac{1}{d_l^4} = -\gamma_o \frac{d_o}{1.4}\frac{1}{d_r^4} + \frac{mgD\sin\theta}{k_B} \tag{3.15}$$

where now d_l is the left side thickness and d_r is the right side thickness, respectively, as shown in Figure 3.14. D is the diameter of the cell and θ is the tilt angle. We have then

$$\frac{1}{d_l^4} - \frac{1}{d_r^4} = 1.808 \times 10^{-10} \sin\theta \text{Å}^{-4} = \text{t}$$

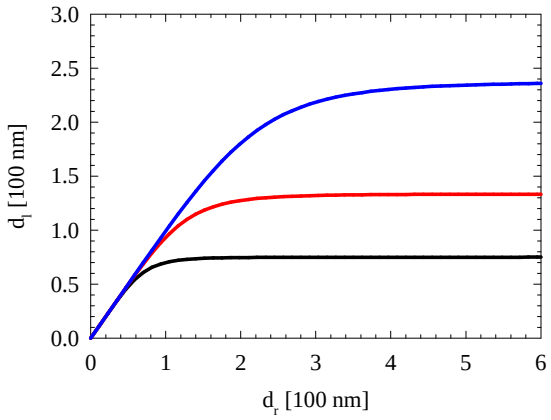

Figure 3.15: Variation of the film thickness as a function of the tilt angle. The black curve corresponds to a tilt angle of 1°, the red curve to 0.1° and the blue curve to 0.01°.

We will call t the tilt factor. Let us now write d_l as a function of d_r

$$d_\mathrm{l} = d_\mathrm{r}[1 + td_\mathrm{r}^4]^{-1/4} \tag{3.16}$$

Figure 3.15 shows the left and right sides thicknesses for different tilt angles. The black curve corresponds to a tilt angle of 1°, the red curve to 0.1° and the blue curve to 0.01°. Even for a tilt of 0.01°, we can observe that above 200 nm the left side of the cell does not adsorbs any more liquid. It is thus important to make sure that the cell is as levelled as possible in order to avoid a non uniform thickness across the entire substrate.

3.4.4 Signal sizes and inferred magnetisation

In order to know the magnetisation of a ^{3}He sample we need an estimation of the number of spins contributing to its NMR line. This estimation is made as follows.

From Equation 3.9 we can obtain the current flowing through the input circuit as a result of a given flux change in the receiver coil. Let us consider a signal following a 90^o pulse. The flux in the receiver coil produced by the NMR signal would be

$$\phi_{\mathrm{r}} = B_{\mathrm{rc}} K M_0 v_{\mathrm{s}}$$

with B_{rc} the field per unit current at the centre of the coil, K the inhomogeneity factor, M_0 the magnetisation of the sample and v_{s} sample volume. This gives rise to an induced voltage across the receiver coil which is given by

$$V_{\mathrm{r}} = -\frac{\partial \phi_{\mathrm{r}}}{\partial t} = \omega_0 B_{\mathrm{rc}} K M_0 v_{\mathrm{s}}$$

since the flux varies sinusoidally with time at a frequency ω_0 and the phase is unimportant for our purposes. For this calculation we will use $B_{\mathrm{rc}} K = 8.7$ mT/A, which is equivalent to take $K = 1$ in Equation 3.9. The factor K is the major source of error in these calculations. Taking it as 1 makes B_{c}, if anything, an overestimation of the actual field within the coil.

The voltage across the receiver coil would produce a current flowing through the input coil

$$I_{\mathrm{ip}} = \frac{\omega_0 B_{\mathrm{rc}} K M_0 v_{\mathrm{s}}}{R_{\mathrm{i}}} \tag{3.17}$$

and a flux coupled to the SQUID

$$\phi_{\mathrm{SQ}} = \frac{\omega_0 B_{\mathrm{rc}} K M_0 v_{\mathrm{s}} M_{\mathrm{i}}}{R_{\mathrm{i}}}$$

where M_{i} is the mutual inductance between the input coil and the SQUID and R_{i} is the resistance of the input circuit. This resistance is given, as noted in Section

3.2.2, by

$$R_{\mathrm{i}} = \frac{\omega_0 L_{\mathrm{T}}}{Q_{\mathrm{ip}}}$$

with L_{T} the total inductance of the input circuit. Therefore

$$\phi_{\mathrm{SQ}} = \frac{B_{\mathrm{rc}} K M_0 v_{\mathrm{s}} M_{\mathrm{i}} Q_{\mathrm{ip}}}{L_{\mathrm{T}}} \tag{3.18}$$

Now, ^{3}He follows Curie's law down to its magnetic temperature, T_{m}=253 mK, below which the magnetisation remains constant as a function of temperature. This gives a magnetisation for a spin density n of

$$M_0 = \frac{n\hbar^2\gamma^2}{4k_{\mathrm{B}}T_{\mathrm{m}}} B_0$$

and this can be related to the total number of spins N_{spins} in the sample by

$$M_0 = \frac{N_{\mathrm{spins}}\hbar^2\gamma\omega_0}{4k_{\mathrm{B}}T_{\mathrm{m}}v_{\mathrm{s}}} \tag{3.19}$$

We can now substitute Equation 3.19 into Equation 3.18 to obtain a flux through the SQUID

$$\phi_{\mathrm{SQ}} = \frac{B_{\mathrm{rc}} K N_{\mathrm{spins}}\hbar^2\gamma\omega_0 M_{\mathrm{i}} Q_{\mathrm{ip}}}{4k_{\mathrm{B}}T_{\mathrm{m}}L_{\mathrm{T}}}$$

This flux is multiplied by the read-out electronics' FLL gain and by the sample and hold gain before reaching the oscilloscope. The Fourier transformed signal height is then given by (see Appendix B)

$$H_{\mathrm{s}} = \frac{V_s T_2^*}{2\Delta}$$

where Δ is the sampling interval. Finally, we need to take into account the fact that

we wait during the input circuit ring-down following a transmitter pulse and only then we start to capture the data. By that time, the original NMR signal will be decreased by a factor e^{-t/T_2^*}. The above analysis was for a 90° pulse. The tipping angle used in these experiments was ∼20° and that needs also to be scaled in our final result. We can now relate the number of spins with the height and width of the measured NMR signal by

$$N_{\rm spins} = \frac{8\, H_{\rm s}\, \Delta\, k_{\rm B}\, T_{\rm m}\, L_{\rm T}}{G_{\rm SH}\, G_{\rm FLL}\, B_{\rm rc}\, K\, \hbar^2\, \gamma\, \omega_0\, M_{\rm i}\, Q_{\rm ip}\, T_2^*\, \cos(70)\, e^{-t/T_2^*}} \tag{3.20}$$

For our particular set-up, $G_{\rm SH} = 0.473$ at 963 kHz, $G_{\rm FLL} = 0.4194\ {\rm V}/\phi_0$, $B_{\rm rc}K = 8.7$ mT/A, $\gamma = 2.038 \times 10^8\ {\rm s}^{-1}{\rm T}^{-1}$, $f_0 = 963$ kHz, $M_{\rm i} = 2.27$ nH, $Q_{\rm ip} = 100$ and $L_{\rm T} = L_{\rm p} + L_{\rm i} = (37.9 + 4.78)\ \mu$H= 42.68 μH. The capture delay time was 460 μs and the oscilloscope was set to 120,000 points in 2400 divisions at 10 μs/division. This gives a sampling interval of $\Delta = 2 \times 10^{-7}$ s/point. T_2^* and $H_{\rm s}$ were obtained from the width and the amplitude, respectively, of the NMR peak. The number of spins can be also translated into film thickness by using the molar volume of ^{3}He (36.59 cm^3/mol) and the substrate surface (9.5×10^{-5} m^3 each plate). We obtain

$$t = 6.393 \times 10^{-25} N_{\rm spins}$$

where t is the total thickness (i.e. top and bottom films) in meters.

3.4.5 The 90 ° pulse

To calibrate the tipping angle provided by a given transmitter pulse, we studied the signal height as a function of the current through a 10 Ω resistor in the transmitter coil circuit. The test was carried out on a sample of 4.1 $\times 10^{17}$ spins at a temperature

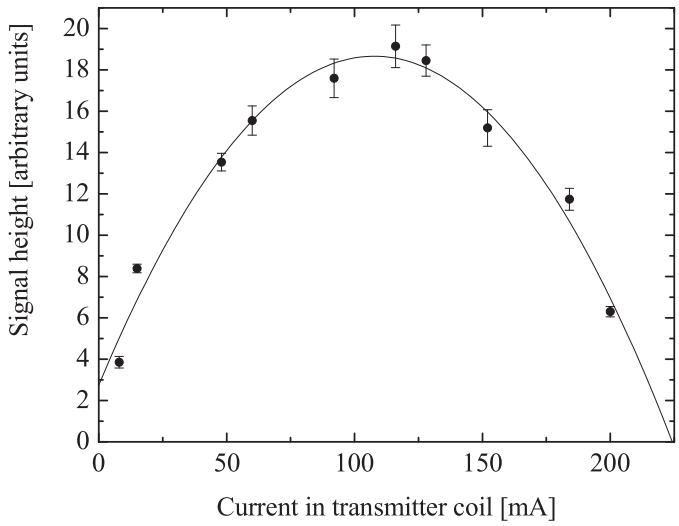

Figure 3.16: The NMR signal height as a function of applied current in the transmitter coil. The transmitter pulse has a frequency of 965 kHz and is applied during 155 μs.

of $\sim$7 mK. The applied current was varied by changing the amplitude of the transmitter pulse, of frequency 965 kHz and duration 155 μs. According to the solution of Equation 3.2, the magnetic field required to produce a 90^o pulse would satisfy

$$\gamma B t = \pi/2$$

when the magnetic field is applied during a time t. Therefore, for t =155 μs, the required magnetic field is 4.97×10^{-5} T. Since the magnetic field exciting the spins is half of the total applied field [50], we would need an RF field of amplitude 9.94×10^{-5} T. From Equation 3.10 the total current needed for a 90^o pulse is 98 mA. Figure 3.16 shows the result of our measurements. The maximum of the quadratic fit to the data corresponds to a current of 112 mA, a discrepancy of $\sim$15% with the calculated value. In order to reduce the eddy current heating and provided that the

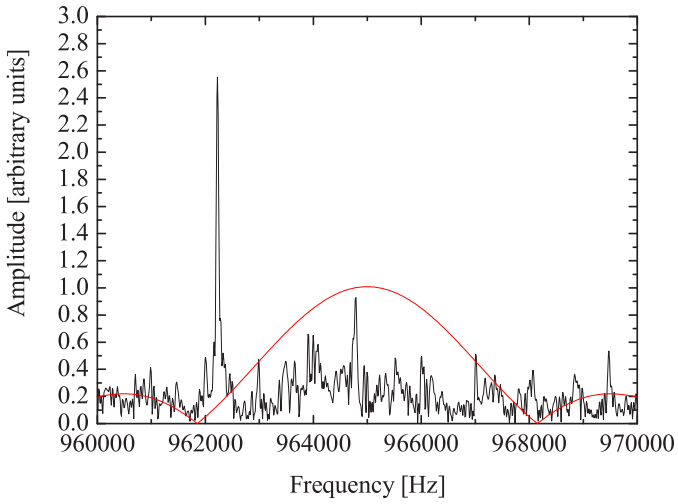

Figure 3.17: The frequency components of the background resonances (black) compared to the frequency components of the 155 μs transmitter pulse (red)

NMR signals could be resolved with ease even for our thinnest samples, a tipping pulse of 20^{o} was used throughout all our measurements.

3.4.6 NMR signals and Background resonances

The NMR data was taken on a PC and Fourier transformed using a LabView routine. We took background signals with the NMR field off-tune. After Fourier transforming this data, several magnetoacoustic resonances were observed in the frequency domain. The comparison of these resonances with the exciting pulse can be seen on Figure 3.17. The signal was averaged for 30 times. A sharp feature is clearly seen at around 962 kHz, even though that corresponds to the first minimum of the transmitter pulse. This peak was coherent in nature and could, therefore, be removed by subtracting the background signal from the data signal. This subtraction was done by moving the static field a few kHz away from the Larmor frequency and subtracting the resultant data set from the signal data in the time domain. We

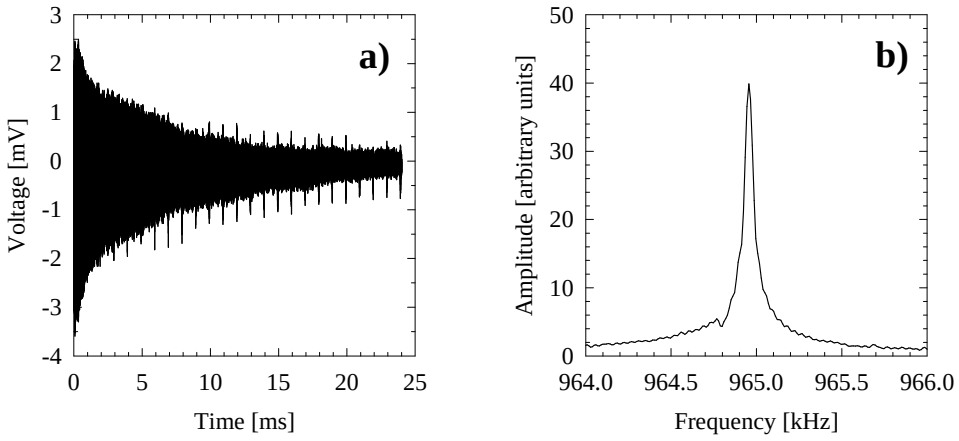

Figure 3.18: Time domain (a) and frequency domain (b) NMR signals for a sample consisting of 29×10^{17} spins (2×927 nm). Data were averaged 30 times.

observed that the background signal changed after transferring liquid helium to the cryostat, so it was needed to refresh it after each transfer.

A typical NMR signal, corresponding to a sample of $29{\times}10^{17}$ spins $(2{\times}927$ nm$)^2$ is displayed on Figure 3.18. The time domain data (Figure 3.18a) was taken for 24 ms. After subtracting the background, the Fourier transformed line (Figure 3.18b) was fitted to a Lorentzian curve to give a T_2^* of 4.3 ms. For shorter T_2^* times (i.e. signals from the superfluid state) a string of zeros could be added to the end of the time domain data to increase the number of points of the NMR line. The frequency resolution in the frequency domain is inversely proportional

[2]From this point onwards we will adopt the following notation when referring to a NMR sample: x spins (2×y nm), meaning that the nominal number of spins was x and that corresponds to two films y nm thick each, should the morphology be that of a regular slab.

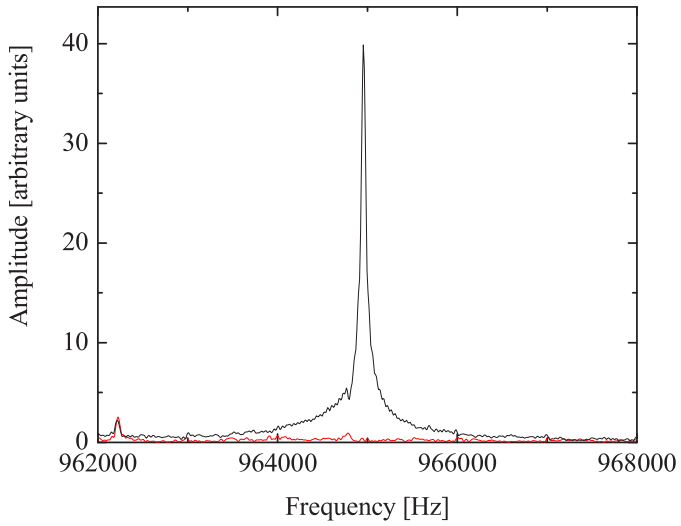

Figure 3.19: NMR signal from 29×10^{17} spins (2×927 nm) (black) compared with the background (red). Both signals were averaged 30 times.

to the capture time so if we double the number of points in the time domain the number of points in the frequency domain is also increased by a factor of two. The feature visible on the left wing of the line in Figure 3.18b was artificially created by the background subtraction. The background (as well as the signal) was divided in small intervals, each of which was fit to a polynomial prior to the subtraction. The number of degrees of freedom allowed in the fits could be chosen. We observed that changing that number of degrees of freedom had different effects on the output Fourier transform lineshape. The final choice was to use a nine-order polynomial.

For our thickest samples, the background subtraction was not strictly necessary, as shown in Figure 3.19.

3.5 Results and discussion

Prior to cooling down to superfluid temperatures, we attempted to make a systematic study of sample growth. The idea was to obtain a signal which would be stable over time and to get the maximum amount of the added atoms inside the experimental cell. We will briefly summarize the observations that led to the sample growth method used in the NMR experiment and will comment on the differences with the method used in the Torsional Oscillator experiment (Section 4.4.1).

3.5.1 Forming the samples

Attaining a stable and well defined film in this cell presents several problems which make the choice of a growth method a critical part of the experiment. One of the difficulties is to ensure that the sample forms inside the cavity and not along the fill line. The fill line heaters are designed to avoid such a problem. Another issue is the possibility of the formation of droplets, rather than an homogeneous film, inside the cell. This is the reason for doing a sample annealing, in which the cell is taken to a higher temperature once the loading has taken place, in an attempt to redistribute the liquid homogeneously. Other problems include the capillary condensation of the liquid in the edges of the cell (which is studied in Chapter 4) and the stability of the sample after its formation.

We studied the growth of four different samples. For our first two samples, consisting of 3.3×10^{17} (2×105 nm) and 5.9×10^{17} spins (2×189 nm), the cell was kept stable at 60 mK with the fill line heater on while the gas was allowed into the fill line. This avoided the formation of liquid outside the experimental cell. The cell was then taken to 450 mK in order to anneal the samples and the NMR signal increased in both cases. Lowering the temperature to 200 mK resulted in the NMR

signal size reaching its maximum. For these two first samples we observed at 200 mK the total number of spins added. Both heaters were kept on during the annealing process. The next step was to cool down the cell again to ~ 80 mK, at which point both heaters were switched off and the cell was taken to the fridge base temperature ($\sim 5-6$ mK). The signal at base had less spins than the signal at 200 mK but was found stable over a period of more than 12 hours.

Since we found that we achieved the total amount of spins added at 200 mK there was no need to go to 450 mK. For the next sample we introduced 9.9×10^{17} spins (2×316 nm) into the fill line with the cell stabilized at 60 mK and both heaters on. The temperature was then raised to 200 mK and left there until the NMR signal stopped increasing. When the magnetisation reached its maximum the same cooling procedure as for the previous samples was used to reach base temperatures. This became from this point onwards the loading method for the NMR cell. The signal at base temperature always showed a number of spins which was smaller than the number of spins at 200 mK, suggesting that part of the sample left the cavity during the cool down. The samples, however, were found to be stable at base temperature for periods of weeks. We used the measured number of spins at base as our nominal loading in the NMR experiment.

This loading procedure was studied once more in a sample consisting of 13.9×10^{17} spins (2×444 nm) with the same results observed in the sample with 9.9×10^{17} spins (2×316 nm).

As we will show in Section 4.4.1, the growth method for the Torsional Oscillator was different from the method described above. In the torsional oscillator cell, the part which is thermally linked to the nuclear stage is the copper isolator located above the oscillator. This is, therefore, the coldest point of the device. The liquid was expected to condense in some volume inside the portion of the fill line running

through the copper mass. In order to encourage the liquid to reach the experimental cell it was needed to heat the nuclear stage up to $\sim$ 450 mK, where the vapour pressure of ^{3}He is $\sim$ 0.1 mbar. In the NMR experiment, however, the experimental cell itself is thermally linked to the nuclear stage and the liquid is expected to condense inside the cavity. Going to 450 mK, therefore, is not necessary to grow a sample within the NMR cell. The growth in signal size observed at 200 mK was probably due to liquid condensed in the silver tube connected to the upper half of the cell being poured inside the cavity due to the gravitational force. Nevertheless, as far as the annealing process is concerned, going to 450 mK in the NMR cell would probably allow the transformation of potential liquid droplets formed inside the cell into a uniform film. The vapour pressure of ^{3}He at 200 mK is quite low (10^{-4} mbar) and evaporation is unlikely, so once the sample is formed no annealing is possible at that temperature. As we will show in Sections 3.5.3 and 3.5.4, some of our samples probably suffered from incorrect annealing and not always formed a film in the NMR experiment.

3.5.2 The solid layer

A solid layer was expected to be formed in the metal surfaces.This solid layer is a consequence of the strong van der Waals binding potential at the substrate surface. The first layer follows Curie's Law (Equation 3.3) down to lower temperatures than bulk liquid. The second layer behaves like a high density liquid. Bulk ^{3}He at zero pressure has a magnetic temperature of T_m = 253 mK. Therefore, at 1 mK, the magnetization per atom from the solid would be 253 times larger than that from the liquid. Typical surface densities are 10 atoms/nm^2 in the first layer and 8 atoms/nm^2 in the second. For our geometry, that means that, for a 100 nm thick film the signal

from the solid should have a magnetisation of about ~ 4 times the magnetisation of the liquid. However, the solid signal has a extremely short T_2^* (hundreds of microseconds), and cannot be observed due to our long capture delay time (460 μs) which is set in order to allow the ring down of the input circuit following the removal of the transmitter pulse.

Another possible effect from the solid layer is a frequency shift in the normal liquid signal due to solid-liquid exchange. Other experiments [42] have observed a tipping angle dependence in the liquid due to the shift in the solid. The frequency shift in the liquid under a constant tipping angle, however, was negligible for a 300 nm thick film. The fact that we do not observe a frequency shift in the normal state liquid even for our thinner samples could be due to its morphology: a liquid droplet, for example, would have much less interaction with the solid than the same amount of atoms distributed as a uniform film.

3.5.3 Imaging the samples

Ideally, one would like to know precisely what the disposition of the liquid is within the experimental cell. We tried to map out the sample's morphology by means of a set of shim coils situated inside the helium bath. These coils allowed us to produce the field gradients $\partial B_z/\partial x$ and $\partial B_z/\partial y$, amongst others. Therefore, the frequency spectrum of the NMR signal can in principle provide an image of the sample. However, a precise calibration of these gradients was not available, since the shim coils are part of the high homogeneity NMR magnet. We applied currents from 1 to 5 A to the X and Y shim magnets in order to produce field gradients of different magnitudes. The currents were applied in both directions so the actual current range was from -5 to +5 A. As shown in Figures 3.20 and 3.21, the NMR

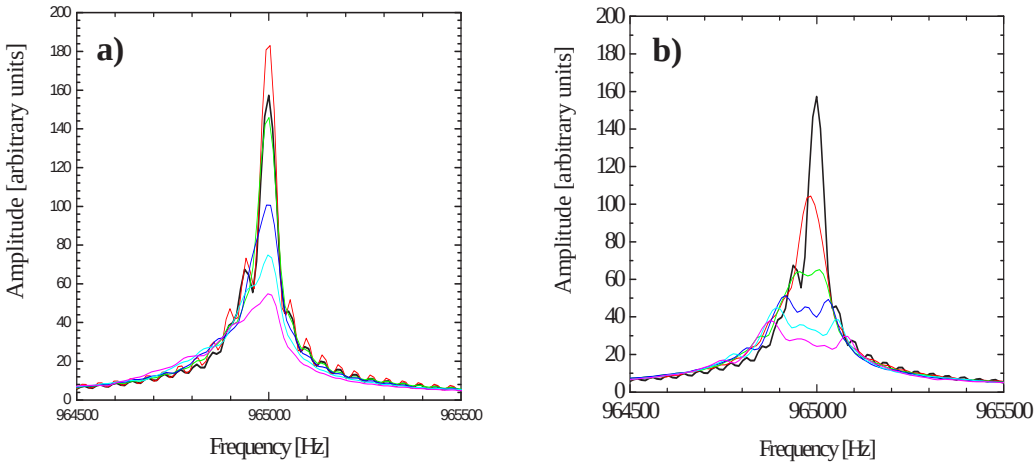

Figure 3.20: NMR lineshapes for different currents in the x-gradient coil. The black line is the unshimmed signal. The applied currents are 1 (red), 2 (green), 3 (blue), 4 (cyan) and 5 (magenta) A. The coil was biased forward (positive currents, b) and reversed (negative currents, a). Data corresponds to a 29×10^{17} spins (2×927 nm) sample.

lineshape changes with the applied field gradient. As the coil current is increased, a two-peak structure develops, the more clear case being the +X shim (Figure 3.20b).

This configuration would be compatible with a capillary condensed ring around the edges of the cell. However, it was observed that the separation between the peaks was not constant, but changed with sample sizes, or even with different anneals of the same sample. That suggested a morphology consisting of little bulk-like droplets condensed over different places within the cavity and which would give rise to a peak separation in response to a field gradient. A spherical droplet 200 μm in diameter (the height of our cell) would contain of the order of 1 $\times10^{17}$ spins. Therefore, some of our samples might well consist of several spaced droplets.

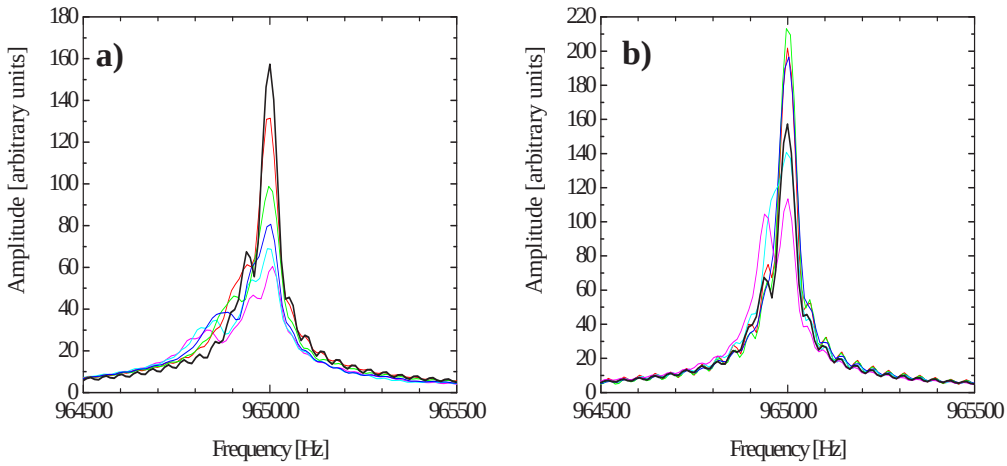

Figure 3.21: NMR lineshapes for different currents in the y-gradient coil. The black line is the unshimmed signal. The applied currents are 1 (red), 2 (green), 3 (blue), 4 (cyan) and 5 (magenta) A. The coil was biased forward (positive currents, b) and reversed (negative currents, a). Data corresponds to a 29×10^{17} spins (2×927 nm) sample.

The unshimmed signal was often seen to be formed by more than one peak, revealing some planar inhomogeneity in our static field. The shim study of the samples also allowed us to determine the optimum shim configuration in order to observe a single peak with maximum height. This configuration varied with the samples. In the case of Figures 3.20 and 3.21 it can be seen that the optimum configuration is +2 A in the Y shim and -1 A in the X shim. The results presented in the next section were obtained with all our samples in the optimum shim configuration.

3.5.4 Superfluid results

We observed superfluid transitions in sample sizes ranging from 3×10^{17} spins (2×96 nm) to 48×10^{17} spins (2×1.53 μm). As discussed in Section 3.4.2, the film thickness of the top film has a higher boundary of about 84 nm and, therefore, it is expected that the majority of the liquid would get adsorbed in the bottom of the cell for our thickest samples.

Due to the imperfect annealing of our samples they probably included small bulk-like droplets with a diameter similar to the height of the cell (200μm), as noted in Section 3.5.3. We show one of the observed superfluid transitions in Figure 3.22. These data correspond to 29×10^{17} spins (2×927 nm, more likely distributed as a ∼1.8 μm slab in the bottom surface) and were taken on warming. A current of -1 A was applied to the Y-SHIM magnet in order to obtain a signal as sharp as possible in the normal state. Two main peaks could, nonetheless, be resolved at temperatures near T_c[3]. The red line corresponds to a temperature of 0.94 mK and it is at the Larmor frequency. As the temperature decreases, we can observe a positive frequency shift and two peaks can be clearly resolved. Below 0.75 mK (green line) the two peaks join in a single peak due to the decrease in T_2^* which makes the lines wider. The coldest signal (blue line) was taken at 0.60 mK. The inset shows the total magnetisation of the signal (black dots), the magnetisation of the left hand peak (red squares) and the magnetisation of the right hand peak (blue triangles). The magnetisation for each peak was calculated by plotting the square of the NMR signal and fitting each individual peak of the squared signal to a Lorentzian. This gave the parameters T_2^* and H_s mentioned in Section 3.4.4 and the number of spins could be then calculated by using Equation 3.20. We can see that below 0.84 mK

[3]With regard to notation, we will refer to the bulk ^{3}He superfluid transition as T_c throughout this work. When talking about the transition temperature of films we will use T_c^{film} or, simply, T_c^f.

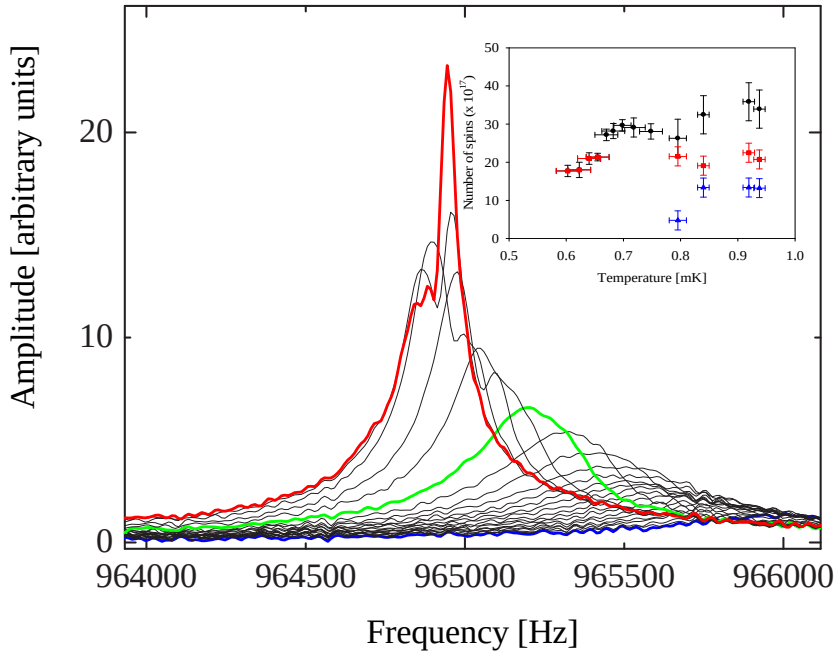

Figure 3.22: Positive frequency shift from a sample consisting of 29×10^{17} spins (2×927 nm). The red line corresponds to a temperature of 0.94 mK and the coldest temperature was 0.60 mK (blue line). At 0.75 mK (green line) the two peaks join each other due to a decrease in T_2^*. The inset displays the dependence of the magnetisation with temperature (see text for explanation).

the total magnetisation drops slightly due to a lost in resolution of the right hand peak. The magnetisation remains nearly constant down to 0.65 mK, where the short T_2^* makes difficult to obtain a reliable estimate of the number of spins.

When doing transverse pulsed NMR on superfluid ^{3}He, it is expected to observe a frequency shift (whose sign depends on the relative orientation of the **l** and **d** vectors) with unchanged magnetisation in the NMR line for ^{3}He-A. A decrease in magnetisation with no change in frequency for small tipping angles would suggest a transition into ^{3}He-B (see Chapter 2). The positive shift observed in Figure 3.22 would suggest a transition into ^{3}He-A with a dipole locked texture. Our static mag-

netic field of ~ 30 mT is enough to make the **d** vector to orientate perpendicular to the field throughout the whole sample in order to minimize the Zeeman energy of the Cooper pairs. The **l** vector would tend to be parallel to the **d** vector in order to minimize the dipole energy, but there is a strong boundary condition on it: the **l** vector is perpendicular to the walls over distances smaller than the dipole bending length. This length, in superfluid ^{3}He-A, is $\sim 10\mu$m, so it would be possible in a 200 μm diameter droplet for the **l** vector to become parallel to the **d** vector, thus producing a positive shift. The B phase could, under certain conditions, produce also a positive shift. The tipping angle in that case should be greater than the critical angle 104^o in order to provide an additional torque in the magnetic moment of the Cooper pairs. Osheroff and Corruccini [60] observed that for tipping angles larger than 104^o two components comprised the precession signal, one of them at the Larmor frequency and the other following the theoretical predictions of Brinkman and Smith [61]. Both components showed a diminished magnetisation. Since that is not what is observed in Figure 3.22 and the magnetisation remains reasonably constant, we can conclude that the observed superfluid transition corresponds to the A phase. We also can rule out a tipping angle larger than 104^o with our small tipping pulses and, therefore, the possibility of a transition into the B-phase can be disregarded. According to the bulk phase diagram of superfluid ^{3}He, the A phase should not occur at zero pressure, but the size effects on the order parameter of superfluid ^{3}He in a 200 μm droplet could be strong enough to produce an A-like phase at the bulk transition temperature even at zero pressure [62], [63]. For smaller samples we observe a similar behaviour (see Figure 3.23). The transition temperature, about 0.89 mK, is sample independent, suggesting that smaller samples consist of a smaller number of similar size droplets. The discrepancy between the transition temperature observed and the ^{3}He bulk transition temperature is attributed to an

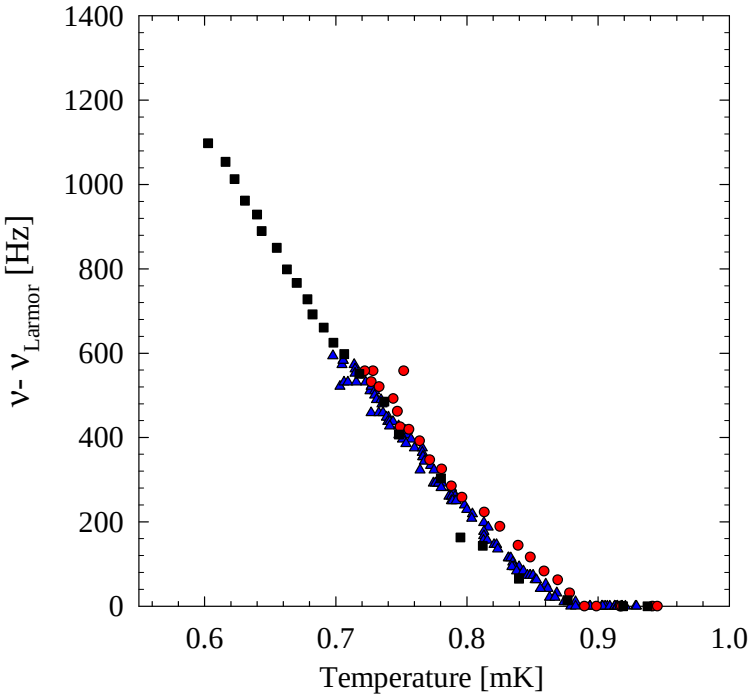

Figure 3.23: The frequency shift as a function of temperature for samples consisting of 29×10^{17} spins (2×927 nm) (black squares), 14×10^{17} spins (2×448 nm) (blue triangles) and 4×10^{17} spins (2×128 nm) (red circles). They all show a similar transition temperature of about 0.89 mK.

inefficient cooling of the samples, which would place them slightly hotter than the PLM thermometer reading (the same effect is observed in the torsional oscillator experiment, see next Chapter).

Another kind of superfluid transition was observed on the 29×10^{17} spins (2×927 nm) sample. The positives shifts shown above were observed the first time the samples were cooled down below the superfluid transition after the annealing. This particular sample, however, behave differently during the second superfluid transition. After observing the discussed positive shift, the sample was left to warm up to base temperature and then cooled again. In this case the normal state signal split into two peaks at 0.82 mK. One of the peaks was shifted negatively whereas

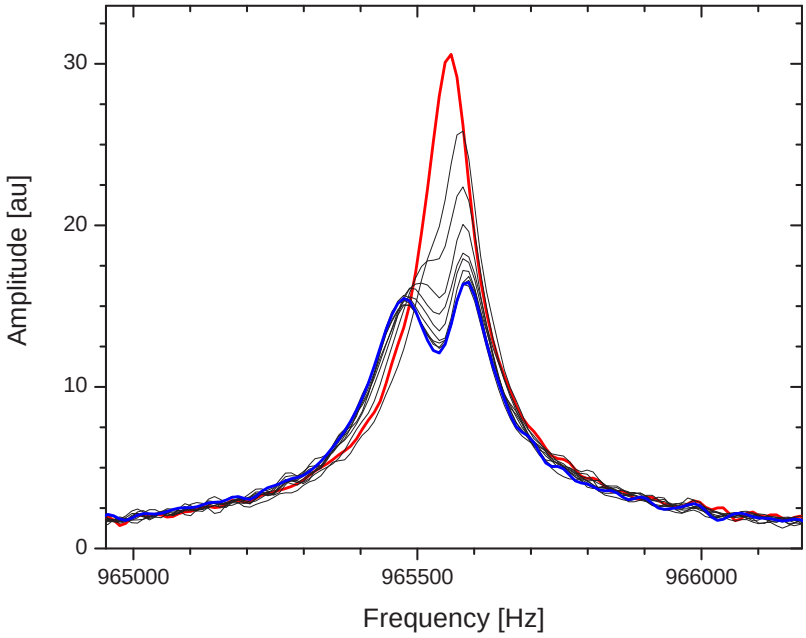

Figure 3.24: Signal split for a sample consisting of 29×10^{17} spins (2×927 nm). Data cover a temperature range between 0.82 mK (red line) and 0.81 mK (blue line) and were taken on cooling.

the other one was slightly positively shifted (Figure 3.24). The data were taken on cooling in small steps, allowing the sample to reach thermal equilibrium in between cooling stages. Further cooling below 0.80 mK produced the signal to snap into a single peak which shifted positively as the temperature decreased. This result could be explained under the light of a spin wave model [64]. In this model the relative orientation of the **l** and **d** vectors changes over the sample, giving rise to different textures. In a uniform **l** field a uniform spin wave is excited with frequency $\tilde{f} = \cos 2\theta$ with θ being the angle between the **l** and **d** vectors. The conditions close to the walls resemble pure **l** vector solitons [65]. The spin wave potential has two minima adjacent to the walls and a maximum in the centre. The potential minima (dipole-unlocked texture) would produce a negative NMR shift whereas the

maximum (dipole locked texture) would produce a positive shift.

We could model our sample by two thin films on the top and bottom plates of the cell joined by a liquid pillar stabilized by capillary condensation. The **l** vector would be pinned perpendicular to the walls by boundary conditions and it would align parallel to the **d** vector in the pillar. Therefore, simultaneous positive and negative frequency shift could be observed below the superfluid transition. This configuration is believed to be metastable and subsequent cooling could result in the liquid snapping into a droplet, thus producing the same results as in Figure 3.22. This was, in fact, the observed behaviour.

Although the signal splitting could only be seen below 0.82 mK that temperature only represents a lower boundary for the transition temperature. Indeed, the small shifted peak could have started the split at a slightly higher temperature but remained unresolved due to a lack of resolution in the NMR line. A reliable extraction of the number of spins from the Fourier transformed NMR signal was not successful due to the proximity of the two peaks. A transition temperature as low as 0.82 mK would suggest we were observing the novel phase predicted by the theory [28] in the region of the confined phase diagram where the B-phase is not available at any temperature.

Although it would be interesting to study the tipping angle dependence of the shift, it was not possible to do such a measurement. Any attempt to increase the tipping angle resulted in the signal jumping into a positively shifted line, probably because the transmitter pulse produced a change in the morphology of the liquid. The signal splitting was highly reproducible in this sample, always on the second superfluid transition after the sample growth. Once it was observed for the first time in a sample, it also could be reproduced provided the temperature was kept below 1 mK.

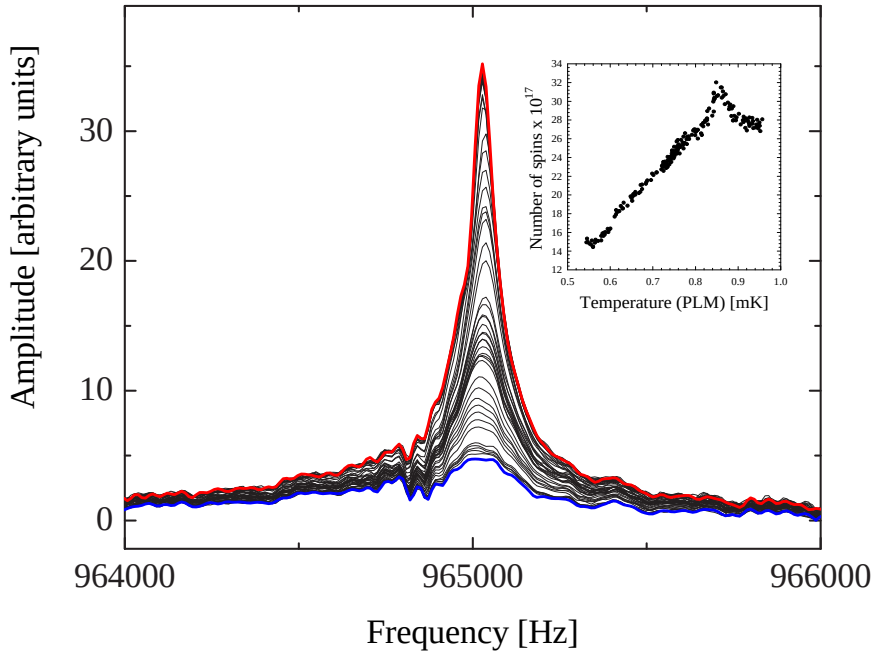

Figure 3.25: A superfluid transition in a sample consisting of 29×10^{17} spins (2×927 nm) with no frequency shift and a decrease on magnetisation (inset) indicative of B phase. The transition temperature is 0.89 mK.

These observations suggested that the first incursion into the superfluid state acted as a sample anneal (a "superfluid anneal"), changing the morphology of the liquid as a result of the mechanical properties of superfluid ^{3}He.

Yet another different superfluid transition was observed on the 29×10^{17} spins (2×927 nm) sample. This observation followed a first cool down to 0.73 mK in order to do a "superfluid annealing". The sample was then taken to 1 mK and cooled down again to 0.53 mK. No frequency shift was observed in this measurement whereas the magnetisation was decreased down to half the value of the normal state magnetisation. Figure 3.25 shows these results. The red signal was taken at 0.94 mK and the blue signal at 0.53 mK. The signal height decreases as the sample is cooled down and the signal width simultaneously increases, in an effect similar

to that on Figure 3.22. But if we calculate the total magnetisation we observe a steady linear decrease, a characteristic associated with the B-phase. In fact, the spin susceptibility of the B-phase is proportional to the Yosida function [20]. In the Ginzburg-Landau region, the Yosida function can be expanded in powers of the energy gap Δ

$$Y(T) \approx 1 - \frac{7}{4}\zeta(3)\frac{\Delta^2(T)}{\pi^2 k_{\mathrm{B}}^2 T_{\mathrm{c}}^2} + ...$$

where ζ is the Riemann zeta function. By using the BCS value of the energy gap it can be proved [20] that the Yosida function is linear from T_{c} down to $0.5T_{\mathrm{c}}$.

The data shown in Figure 3.25 were taken on warming and the sharp feature on the magnetisation near T_{c} could be due to a B to A transition before reaching the normal state. That transition would take place over a very short temperature range [28] and the frequency shift associated with it could be masked by the fact that each data set was taken averaging pulses for 50 minutes. The B to A transition could occur during the acquisition of a single NMR data set with the signal shifting in frequency and coming back to the Larmor frequency in that period of time. The averaging procedure would produce an artificial widening of the unshifted signal because of the temporary shift. This would translate into a smaller T_2^* and, hence, a larger magnetisation, according to Equation 3.20.

This sample was subsequently cooled down from 1 mK to 0.79 mK and a signal split like the one shown in Figure 3.24 was observed. Although this method of sample growth and superfluid anneal was repeated up to four times, the B-transition could not be reproduced, and from the second superfluid transition only a signal split was observed.

A thicker sample consisting of 48×10^{17} spins (2×1.53 μm, probably distributed as a 3.0 μm slab on the bottom surface) was formed and annealed in the same fashion

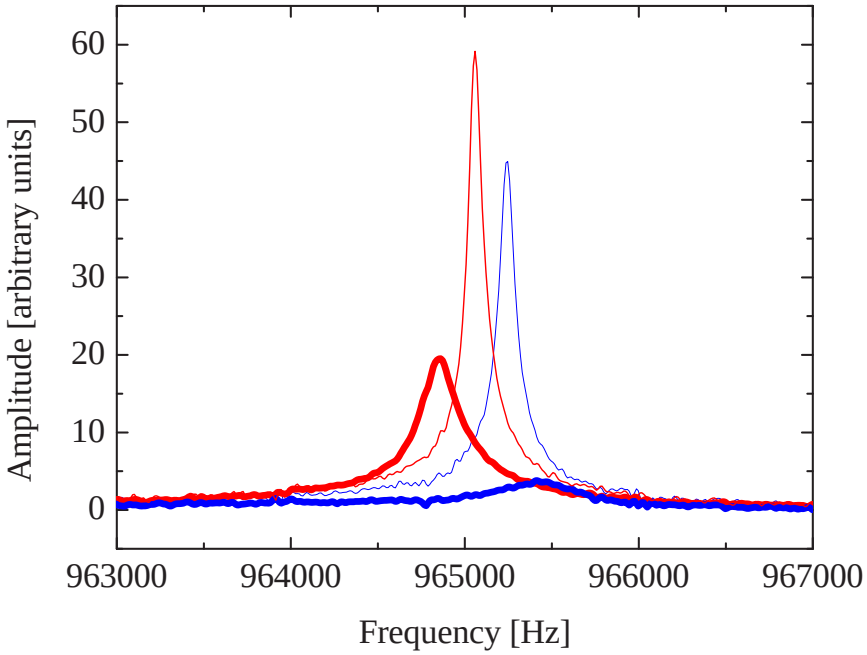

Figure 3.26: NMR signals showing negative shift from a sample consisting of 48×10^{17} spins (2×1.53 μm) on two different coolings. Red lines are negative frequency shifts and blue lines are at the Larmor frequency. The sample was cooled down to 0.38 mK (thick lines) and 0.75 mK (thin lines).

as the previous samples. In this case, and during the second demagnetization below T_c, we observed a signature of the A-phase over two different coolings. The first incursion into the superfluid phase in this sample was not monitored, as it was used as a superfluid anneal. In the second demagnetization below T_c, the whole signal was negatively shifted, consistent with a dipole unlocked texture. We show the transitions in Figure 3.26. After about 20 hours in the superfluid state the NMR signal jumped to the Larmor frequency and showed a decreased magnetisation suggesting a transition into the B-phase with the **n** vector parallel to the static magnetic field. No transition temperature could reliably be extracted because the sample was not allowed to reach thermal equilibrium with the PLM thermometer during the cool

down. Each NMR data set was acquired for 50 minutes, an interval of time during which the sample was changing its temperature and the PLM thermometer, pulsed every five minutes, was showing different readings. In Figure 3.27 we can appreciate this behaviour in the spacing of the green triangles, which correspond to this sample. The points were taken at equal intervals of 50 minutes, as noted above. Near T_c, during the demagnetization process, the points are spaced out, indicating a fast change in temperature. When the demagnetization was finished both, the sample and the thermometer, kept cooling, more slowly, for several hours until they reached thermal equilibrium with the nuclear stage. This slower change in temperature can be appreciated in the closed together green points of Figure 3.27. The minimum temperatures were 0.38 mK (thick lines in Figure 3.26) and 0.75 mK (thin lines in Figure 3.26). No subsequent B to A transition was observed on warming.

The superfluid A-phase would be stabilized only over a narrow temperature regime near T_c for such a thick film. 3 μm translates into approximately 40 coherence lengths, corresponding to an interval of less than 0.05 mK in which the A-phase is stable (see Figure 2.7). This indicates a strongly supercooled A-phase in a metastable state and points out the first order nature of the A to B transition in superfluid ^{3}He. Note that the cell levelling would play a relevant role in such a thick film (see Section 3.4.3) and the thickness of the slab at the upper side of the tilted substrate could be significantly smaller than the thickness at the lower side.

This is, to our knowledge, the first A-B transition observed in a ^{3}He film at zero pressure using transverse pulsed NMR.

The problem of the B-phase nucleation in a supercooled A-phase has been studied in the past both, theoretical [66], [67] and experimentally [68], [69] and, most importantly, [62]. For a bubble of B-phase within the supercooled A-phase to grow it has to have a minimum critical radius of $R_c = 2\sigma/|\Delta F|$, where ΔF is the dif-

ference in the bulk free energies of the two superfluid phases and σ is the surface tension. R_c has a value of about 0.45 μm at $T = 0$ and increases with temperature, reaching a value of $\sim 1.5\mu$m at $0.7T_c$. For smaller radii, the surface energy forces the B-phase bubble to disappear. The transition from the supercooled A-phase to the energetically preferred B-phase occurs due to thermal fluctuations within the A-phase. The values of R_c stated above correspond to an energy barrier for thermal nucleation of the order of $10^6 k_B T$, which makes homogeneous nucleation impossible in this system. Several possible explanations to this phenomenon have been given in the past. One of those explanations is the nucleation near the surfaces of the container. The textural effects associated with rough surfaces could depress the barrier to nucleation. Another option is a model proposed by Leggett in 1984 [67] and called the "baked Alaska" effect. In this model cosmic ray muons or other forms of ionizing radiation pass through the supercooled A-phase. Secondary electrons created by these cosmic rays would heat the superfluid above T_c within a volume of the order of R_c^3. ^{3}He quasiparticles have a mean free path comparable to this radius and, thus, would form a shell of normal fluid with the center relatively free of quasiparticles. Leggett suggested that the B-phase could nucleate in this interior and grow, protected by the normal fluid shell, large enough to be stable when the shell dissipated. This model was tested at Stanford in 1992 [62] using a ^{60}Co source to simulate cosmic-ray muons and it was found that the nucleation rate increased by more than three orders of magnitude when the ^{60}Co sample was placed near the superfluid. On restricted geometries, they suggested that nucleation could be possibly induced by a combination of the radiation and the textural defects caused by rough surfaces.

Under the light of the above considerations we could suggest that A to B transition observed in our largest sample was triggered by the surface roughnesses in

combination with ionizing radiation. A small B-phase seed would form at the surface of our cell and grow from there. For our positive shifts, the possibility of a spherical A-phase droplet would imply that the liquid had less contact surface with the roughnesses, making the nucleation less likely.

It is interesting to compare our results with the expected NMR behaviour for the bulk. Although no measurements have been done at saturated vapour pressure concerning the transverse NMR shift of ^{3}He-A, the higher pressures measurements can be extrapolated to make them comparable with our work. The NMR transverse frequency shift in ^{3}He-A in bulk samples is given by the Pythagorean relation

$$\nu_{\rm trans}^2 = \nu_{\rm long}^2 + \nu_{\rm L}^2$$

where $\nu_{\rm L}$ is the Larmor frequency and $\nu_{\rm long}$ is the usual field-independent frequency of the longitudinal ringing of the A-phase following a sudden change in the magnetic field. For both the, A-phase and B-phase, the longitudinal resonance given by Leggett is [70]

$$\nu_{\rm long}^2 = \alpha(3\pi\gamma^4 h^2) < R^2 > [\Psi]^2/\chi \tag{3.21}$$

where γ is the gyromagnetic ratio for ^{3}He, h is Planck's constant, α is a phase-dependent factor (1/2 for B-phase and 1/5 for A-phase), χ is the magnetic susceptibility and $[\Psi]$ is the amplitude of the order parameter. $< R^2 >$ is a renormalization constant. Substituting the order parameter in Equation 3.21 we obtain, near $T = 0$ for the A-phase

$$\nu_{\rm long}^2(A)[T] = \nu_{\rm long}^2(A)[0][1 - C(T/T_{\rm c})^4]$$

Schiffer *et al.* [71] measured the temperature dependence of the longitudinal resonance at pressures of 5, 12, 21, 29.4 and 34.2 bars. At the lower pressures the

B-phase always nucleated relatively close to T_c, limiting their data to the high temperature regime. However, for the 29.4 and 34.2 bars data they could measure $\nu_{long}(A)$ in the low temperature limit. The slope of $\nu^2_{long}(A)[T]$ versus $(T/T_c)^4$ gave them a value for $\nu^2_{long}(A)[0]$ which they then used to obtain the averaged energy gap, Δ_{A0}, as a function of the BCS cutoff energy ϵ_c. The cutoff energy is bounded between 0.040 and 1.0 K and they found that Δ_{A0} was remarkably insensitive to it. The renormalization factor (a function of the energy gap and the cutoff energy) they used was obtained from the B-phase data in the low temperature limit.

Moving now on to the Ginzburg-Landau limit, ν^2_{long} is linear in $(1 - T/T_c)$, the slope being given by

$$\frac{\partial[\nu^2_{long}(A)]}{\partial(T/T_c)} = -\frac{\pi}{10}\gamma^2(1+\frac{1}{4}Z_0)[2N(0)]\frac{\Delta C}{C_N} < R^2 > (k_B T_c)^2 \left(\ln \frac{1.14\epsilon_c}{k_B T_c} \right)^2 \quad (3.22)$$

We will call this slope $-f(P)$ because it is a function of the pressure only (provided we stay within the Ginzburg-Landau regime). Reference [71] takes into account that the linear behaviour of the longitudinal shift in temperature is restricted to a region near T_c. In fact, they find that the curvature is insignificant for $T > 0.9T_c$ and pressures below 34.2 bars.

The only quantities which remain uncertain in Equation 3.22 are ϵ_c and $< R^2 >$. The value of the slope can be used to get a relationship between these two quantities. $< R^2 >$ is found to depend only weakly, if at all, on temperature. The values of the cutoff energy closest to the theory are obtained using $< R^2 >= 1$ and this value falls around 0.8 K at zero pressure. A linear fit to the points of reference [71] gives a value for the slope at zero pressure of $f(P)_{P=0} = 0.489 \times 10^{10}$ Hz^2. Another work [72] provides only a data point at 2.05 bar for $f(P)$ (0.61×10^{10} Hz^2) and use this point along with some other experimental data [73], [74], [75], all above 20 bar, to

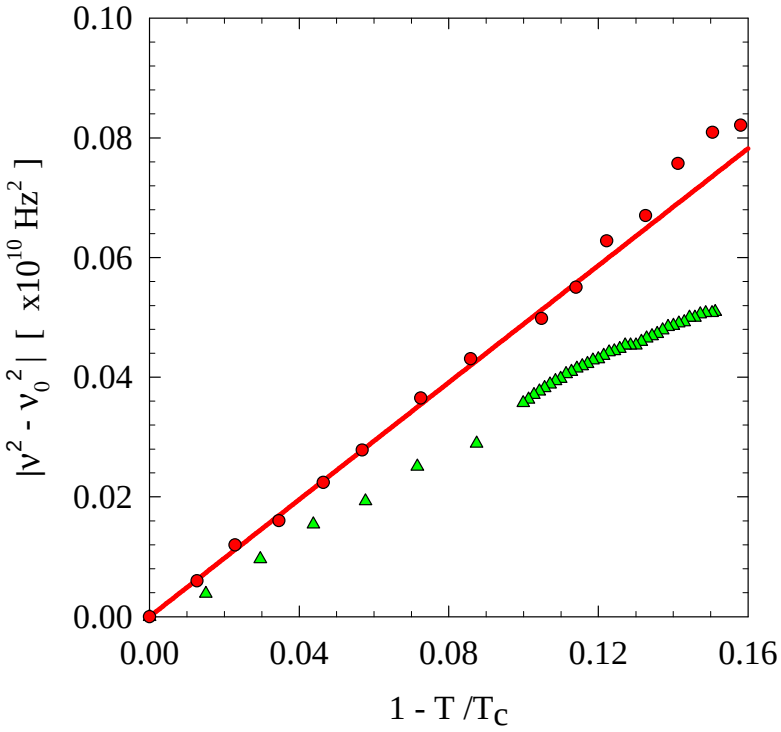

Figure 3.27: Positive frequency shifts from our 29×10^{17} spins (2×927 nm sample (red circles) compared to the zero pressure extrapolation of the bulk data from reference [71] (red line). The negative shift from the 48×10^{17} spins (2×1.52 μm) sample (green triangles) is shown for comparison.

map out the $f(P)$ function. Reference [72] uses a value of 0.7 for $< R^2 >$ and a value of 0.7 K for ϵ_c, both independent of pressure. We use reference [71] to compare our data with, since it is more accurate at lower pressures than reference [72].

Our A-phase positive frequency shifts are in good agreement with the bulk data (see Figure 3.27, red circles) down to $T \sim 0.85T_c$. As discussed above, it is unlikely that the observed frequency shift came from B-phase due to our small tipping angle along with the results from the imaging attempt. Figure 3.27 adds yet another support to the hypothesis of a bulk-like A-phase taking place in our small droplets with a transition temperature similar to the normal to B transition temperature in bulk at zero pressure. We show the negative shift data (green triangles in Figure

3.27) to highlight the difference in behaviour of the two superfluid transitions. They show a fair departure from the bulk data. This could be a signature of suppression of the order parameter. As these data were taken on cooling, there exists the chance that the actual points would be slightly hotter than the points displayed. This would only make the green triangles to lie further from the extrapolated red line.

As mentioned in Chapter 2, there have been other measurements of the A-B transition on the past [45], [46] for film thicknesses of the order of 1 μm and a range of pressures from 10 bar to 30 bar. A supercooled A phase was observed at 10 bar [47] by the Osaka City University group. This group made measurements on ^{3}He slabs of fixed thickness of 1.1 μm with diffuse boundaries. Their substrate was polyethylene and the used ^{4}He to coat the surfaces. For their higher pressures, 20, 24 and 27 bar, they observed a suppression of $T_{\rm AB}$ of about 15% with respect to the bulk transition. The supercooled A-phase they observed at 10 bar had a $T_{\rm AB}$ transition temperature of 1.5 mK whereas the theoretical calculations [27] predicted 1.7 mK. The supercooled A-phase survived for four days in their run.

Another experiment in which a supercooled A-phase was observed is that of Freeman and Richardson [42]. They performed measurements on 300 nm thick ^{3}He films enclosed by two diffusive walls and used Mylar sheets as a substrate. They observed the superfluid A-phase, but not the A-B transition. Their pressures ranged from 1.5 to 22.6 bars. They also studied the effect of coating their substrate with ^{4}He and found indication of specular boundary conditions, as the superfluid transition temperature approached the bulk value by increasing ^{4}He coverage.

3.5.5 Conclusions

Our cell was designed to allow us to continuously tune the film thickness at zero pressure. Unfortunately, our sample growth method was not optimal and our samples probably suffered from imperfect annealing, as the measurements performed with our shim coils suggested.

We detected NMR signals from superfluid samples ranging from 3×10^{17} (2×96 nm) to 48×10^{17} spins (2×1.52 μm). All samples showed a positive shift the first time they were cooled down below the superfluid transition, which was measured to be 0.89 mK, independent of the sample size.

For our 29×10^{17} spins (2×927 nm) sample we observed a different behaviour after the first superfluid transition. During the second cool down the NMR signal split into two peaks at 0.82 mK and snapped into a single positively shifted peak at 0.80 mK. This behaviour could be explained by a spin-wave theory. After reannealing this sample, and following a first incursion into the superfluid state, another kind of superfluid transition was observed. This time, the NMR signal remained at the Larmor frequency and showed a linear decrease in magnetization, a signature of the superfluid B-phase. The transition temperature was again 0.89 mK. Following this transition, the signal split observed before was recovered. The B-phase transition could not be reproduced in subsequent reannealings of the sample.

Finally, for our 48×10^{17} spins (2×1.53 μm) sample we observed a negative shift over two different coolings. This was a signature of the A-phase in its dipole-unlocked texture, which, with our experimental settings, could only be caused by a film. This A-phase was strongly supercooled, remaining in that state at temperatures of 0.38 and 0.75 mK for around 20 hours before a sudden transition into the B-phase. Subsequent warming of the B-phase did not show a signature of the A-phase before

the normal state. These were, to the best of our knowledge, the first observations of the A-B transition on a confined slab geometry at zero pressure. Other works [47] have observed the A-B transition at pressures as high as 20 bars in 1.1 μm thick films, whereas supercooling of the A-phase has likewise been observed at high pressures [42], [47].

The temperature dependence of our positive frequency shifts was in good agreement with the extrapolation to zero pressure of previous studies [71] done in bulk superfluid ^{3}He at higher pressures.

We showed that our SQUID spectrometer has enough sensitivity to observe signals from films thinner than 100 nm. The measured noise temperature, 800 mK, was, however, much higher than the 78 mK expected. This was believed to be caused by the inductive coupling of the APF coil to the input coil. Further improvements in the spectrometer include the use of SQUIDs without APF and SQUID arrays. The next generation of cells for this project are based on alternative geometries, where the cavity would be a single submicron slab and the pressure could be changed in order to tune the reduced thickness $d/\xi(T)$. In such a geometry there is the advantage of a well-defined morphology of the sample, but the minimum reduced thickness achievable is limited by the size of the cavity, since the coherence length can only be decreased by applying pressure. These cells would be made out of materials which would be strong and flat at the same time. Glass and silicon are the two more immediate candidates at the time of writing.

Chapter 4

The Torsional Oscillator experiment

Any sufficiently advanced technology

is indistinguishable from magic.

Arthur C. Clarke.

Rationale

The torsional oscillator technique was first used by Andronikashvili in 1946 when studying the normal and superfluid components of ^{4}He-II [76] and nowadays it has become a widespread technique in the study of superfluids. It allows the detection of extremely small changes in the moment of inertia of the system under investigation. In the case of superfluid ^{3}He, the superfluid component of the liquid decouples from the oscillator and no longer contributes to the total moment of inertia. This

causes the oscillator to resonate at a slightly higher frequency. The fraction of fluid decoupled can then be measured by measuring the shift in the resonant frequency.

In these experiments the torsional oscillator has been used to study the flow of ^{3}He slabs in the extreme Knudsen limit. In this limit the inelastic mean free path, $\lambda = v_{\rm F}\tau_\eta$ where $v_{\rm F}$ is the Fermi velocity and τ_η the quasiparticle relaxation time, is much larger than the slab thickness, and so is the viscous penetration depth, $\delta = (2\eta/\omega\rho)^{1/2}$ with η the viscosity and ρ the density. Therefore, in this regime, the film is expected to be locked to the oscillating surface and can be regarded as a surface boundary layer. The inelastic mean-free path is temperature dependent in normal ^{3}He, in contrast to classical fluids, with $\lambda \propto 1/T^2$. The reason for this is the Fermi liquid nature of liquid ^{3}He. This dependence of λ with T allows us to enter the Knudsen regime (for which the Knudsen number, $K_{\rm N} = \lambda/d \sim 1$) from viscous flow (where $K_{\rm N} < 1$ and the main interaction of the quasiparticles is with themselves) by cooling down the sample. Beyond the Knudsen limit one enters the ballistic regime (or extreme Knudsen limit, $K_{\rm N} \gg 1$) in which the inelastic mean-free path is much larger than the thickness of the slab and the main interactions of the quasiparticles are those with the walls. It is, therefore, in the ballistic regime in which the surface roughness plays an essential role. In fact, the nature of the elastic scattering processes from the surface is what determines whether the film will remain locked to the oscillating substrate or not. The surface roughnesses correlations are of the uttermost importance when describing the interaction between the liquid and the substrate.

An important part of this experiment explores the behavior of the liquid in its normal state. This was motivated by some very surprising results observed at temperatures well above the superfluid transition.

Of course, ^{3}He is not the only system for which this technique is employed.

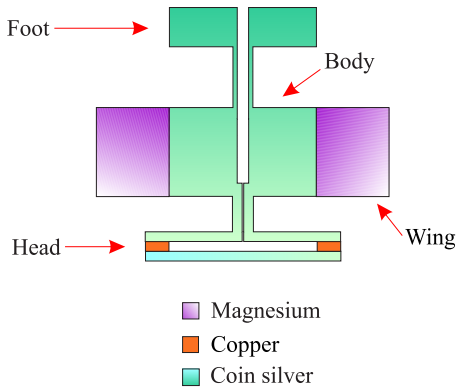

Figure 4.1: Cross section of the torsional oscillator (not to scale)

Other experiments involving torsional oscillators include gravity waves studies [77] and, more recently, possible quantum flow in solid ^{4}He [78].

In this Chapter we will describe the design and construction of the torsional oscillator and the experimental setup. We will then present the data obtained from the normal liquid measurements, which showed a decoupling of the film, and will discuss the results under the light of an internal friction model. We will describe the changes made in the cell's surface in order to pin the films down to the superfluid transition temperature. The last part of the Chapter will show the superfluid transitions observed in our films and a comparison of our results with past experiments and theories will be provided.

4.1 Oscillator design

The torsional oscillator used for this experiment is a double oscillator (see Figure 4.1). We will give here a brief description of its design and method of construction. A more detailed account can be found elsewhere [79], [80]. There are two oscillating parts in the device: the head, which contains the ^{3}He sample, and the body, cylindrical in shape. The head, which is built with two circular pieces, is attached

to the body through a hollow torsion rod. A second hollow torsion rod connects the body to the foot of the oscillator, which is clamped to the nuclear stage and does not oscillate. Both torsion rods also function as a fill tube to admit the ^{3}He sample. The upper part of the cell, both torsion rods, the body and the foot are machined from a single piece of coin silver (silver-copper alloy with 90% silver and 10% copper). The lower part of the head is a circular disc machined independently, also from coin silver. Two magnesium wings are attached to the body in order to excite and detect the oscillator's motion, forming a pair of capacitive transducers with two copper electrodes mounted on the experimental plate.

The device has several natural resonant modes, namely, two torsion modes (symmetric and antisymmetric) as well as floppy modes. We run the oscillator in the antisymmetric torsion mode (i. e. the head and the body oscillating out of phase about an axis along the torsion rod) for this is the most sensitive mode to any potential change in the oscillating frequency arising from changes in the moment of inertia of the head. The floppy mode (in which the head and body oscillate about an axis perpendicular to the torsion rod) is desired to be as high in frequency as possible in order to prevent it from being excited. This is achieved by using a short torsion rod and by keeping the wings as close to the rod as possible. The moment of inertia of the head for the antisymmetric torsion mode is desired to be as small as possible in order to be sensitive to any potential decoupling of the liquid ^{3}He sample.

To detect the mass loading of ^{3}He slabs as thin as 100 nm an extremely sensitive torsional oscillator is required. Torsional oscillators used to study bulk superfluid ^{3}He have a typical slab thickness of ~ 5 μm and are usually machined from BeCu. In our case, due to the small samples studied, the frequency stability and the temperature dependence of the empty oscillator are critical. This was the reason behind the

choice of coin silver, which provides a small background temperature dependence of the resonant frequency as compared to equivalent BeCu oscillators [81]. The frequency stability of the oscillator under a stable temperature was found to be better than $\pm 1\mu$Hz/10h, which translates into a frequency resolution better than 1 part in 10^9. The wings were made out of magnesium (a low density metal to minimize its moment of inertia). This magnesium electrode had to be electrically isolated from the body, since they would be biased at a high voltage during the experiment in order to drive the oscillator and detect its response. The electrodes were, therefore, epoxied to the body with cigarette paper spacers [79]. The epoxy used was Stycast 2850 FT. The two discs which form the head of the oscillator are 15 mm in diameter and each 1.05 mm thick. They are diffusion welded by mean of a 50 μm thick 0.5 mm wide copper gasket [79]. The head torsion rod has a length of 2.5 mm an ID of 0.36 mm and an OD of 1.8 mm. The body is a cylinder 7.5 mm high with a diameter of 13 mm. The body torsion rod is 5 mm long with an ID of 1 mm and an OD of 1.6 mm. The device is mounted on to a copper torsional isolator which serves as a filter for high frequency vibrational noise coming from the environment. This torsional isolator is a cylinder with a diameter of 3.9 cm and 1.5 cm high. It presents a 1 mm diameter clearance drill through which the oscillator fill line runs. The isolator joins a smaller copper block, 13 mm in diameter and 4 mm high, which, in turn, is attached to a copper post connected to the nuclear stage of the cryostat. The resonance frequency of the isolator is 25 Hz. Also attached to the isolator are the L-shaped copper electrodes, 5 mm thick and 24.5 mm high, placed within 50 μm of the oscillator wings. The foot of the electrodes is 15 long and 5 mm high. The coaxial cables connected to the electrodes are anchored to the isolation mass to avoid coupling any acoustic vibration and to promote the stability of the oscillator frequency. All these dimensions were chosen for the antisymmetric torsion mode to

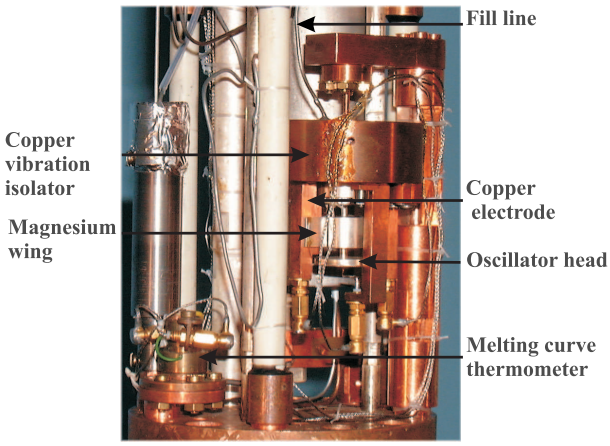

Figure 4.2: The torsional oscillator mounted on to the nuclear stage.

resonate at about 3 kHz. The lengths of the torsion rods set the floppy mode of the whole oscillator at 341 Hz and the floppy mode of the head at 4.6 kHz. The resonance frequency of the symmetric torsion mode was found at 660 Hz. Once in the cryostat, the cell was levelled to a degree better than 0.1° with the aid of a travelling microscope. Figure 4.2 shows the torsional oscillator mounted on to the nuclear stage and the ^{3}He Melting Curve Thermometer next to it.

4.2 The experimental cell

The torsional oscillator experimental cell shares the design with the NMR cell described in the previous chapter, the only difference being the bond between the two silver plates. The polishing recipe explained in Section 3.4.1 was used to achieve a roughness of ± 10 nm over a length of 50 μm. For this cell, however, the upper surface formed a single piece with the oscillator's body and had to be mounted on the polisher with the help of a brass holder. The available space in the mechanical polisher constricted the maximum length of the oscillator to 2 cm. Once polished, both discs were assembled with the copper gasket. Copper makes the bond leak

Figure 4.3: Probable film profile within the cell

tight and provides good thermal contact between both coin silver plates. Also, copper and coin silver have a similar thermal expansion coefficient. The assembly was then taken to 755 °C for 40 minutes in a furnace while held together with the help of a jig. This procedure relies on the phase diagram of copper and silver alloys [81].

4.2.1 Study of the film profile

The copper gasket presumably produces a corner much sharper and defined than the Stycast in the NMR cell. It is possible then to make an estimation of the liquid profile within such a cavity. A possible situation is depicted in Figure 4.3. We assume that there exists the possibility for capillary condensation to occur (i. e. the height of the cell is less than twice the capillary length, which for ^{3}He is about 380 μm). The question is how thick the film can be grown before it capillary condenses, at which point any subsequent liquid allowed within the cell would join the meniscus. We want to compare the cost in energy of adding a particle to the film to the cost in energy of adding a particle to the corner. For this reasoning, and since we want to obtain the thinnest film at which capillary condensation occurs, we will use the non-retarded Van der Waals potential without the retardation effects introduced in Section 3.4.2 where we were studying much thicker films. Gravity is neglected this time for simplicity. Assume that the chemical potential before adding the particle is μ_o. Then, the energy cost of adding a particle to the film is given by

$$\mu_f = \mu_o - \frac{C_3}{z^3}$$

Now for the meniscus we have that the change in energy is going to be given by the change in the surface energy of the liquid-vapour interface. This will involve the surface tension of the liquid, which is the energy per unit area at the interface. The pressure difference across the liquid-vapour interface is given by [82]

$$\sigma(\frac{1}{R_1} + \frac{1}{R_2})$$

with R_1 and R_2 the two principal radii of curvature at the surface. For our case, these radii are the radius of the cell and the radius of the meniscus. The radius of the meniscus is much smaller than the radius of the disc and therefore we can neglect the latter in the previous expression and simply write

$$dp = \frac{\sigma}{r}$$

That change on pressure results in a change on the molar Gibbs energy or, in other words, on the chemical potential according to the well known $d\mu = vdp = dp/n$ (at constant temperature), with v the volume of a particle and n the number of particles per unit volume. The energy cost of adding a particle to the meniscus is, then,

$$\mu_{\mathrm{m}} = \mu_{\mathrm{o}} - \frac{\sigma}{r} \cdot \frac{1}{n}$$

The negative sign arises from the fact that the concave vapour-liquid interface implies that the liquid has lower pressure than the vapour. Since the vapour pressure is zero in our experiment, the liquid pressure has to be negative. Therefore the negative sign in the surface energy.

Now we can set both potentials equal and get

$$\frac{\sigma}{r} \cdot \frac{1}{n} = \frac{C_3}{z^3}$$

Since r has an upper bound (h/2), it cannot become arbitrarily large and therefore neither can z. At some point the atoms will start joining the meniscus. We can define the characteristic length $\zeta = (nC_3/\sigma)^{1/2}$ [83]. Then we obtain

$$r = \frac{z^3}{\zeta^2}$$

Using now the values $\sigma = 1.55 \times 10^{-4}$ J/m^2, $C_3 \sim 3500$ KÅ^3 and a density of 36 gm/cm^3 for ^{3}He, we get $\zeta \simeq 2$ nm. The maximum radius achievable is $r = h/2 = 25$ μm. That implies a maximum film thickness of $z \sim 50$ nm.

According to the previous calculation we should be prevented from growing films thicker than 50 nm. That is certainly not the case reflected by the data. A possible explanation could be related to the growth method used for this cell (see Section 4.4.1): the film might be deposited by distillation from the liquid condensed along the fill line that runs through the body. A thicker film thus deposited could probably be metastable in this geometry.

4.3 Experimental details

In order to carry out the measurements we need to apply a periodical force to the oscillator and measure its response to that excitation. Figure 4.4 shows the experimental setup employed for this purpose. We applied a periodic sinusoidal signal from a Stanford function generator (model DS345) to one of the copper electrodes to excite the oscillator. The measured capacitances of the transducers formed by

the copper electrodes and the magnesium wings were 4.75 and 2.89 pF. To improve sensitivity the detection electrode was the one with the larger capacitance. The wings of the oscillator were connected to a DC voltage of 100 V through a resistance of 10 MΩ. A 1 μF capacitor connected to ground acted as a short for any parasitic AC current coming from the voltage supply. The purpose of this high tension was to linearize the force applied on the wings of the oscillator. The force exerted on the plates is given by $F = CV^2/2d$, which is not linear in voltage. However, when the AC signal is on top of a high enough DC voltage, we have

$$V = (V_{\rm DC} + \delta V), \qquad \text{and} \qquad V^2 = (V_{\rm DC} + \delta V)^2$$

$$V_{\rm DC}^2 + 2V_{\rm DC}\delta V + (\delta V)^2 \simeq V_{\rm DC}^2 + 2V_{\rm DC}\delta V$$

since the amplitude of the exciting signal (2 mV) is much smaller than the DC voltage applied and we can neglect second order terms in δV. The output was sent through a EG&G preamplifier model 5182 to a Krohn-Hite filter model 3343 set as a band pass between 1700 and 3700 Hz and lock-in amplified with a Stanford model SR830 DSP. The in-phase and quadrature components of the signal were introduced into a computer which also controlled the Stanford generator parameters. The Stanford function generator was communicated with the computer by means of a GPIB interface. The oscillator was driven at a fixed frequency close to its resonance. From the in-phase and quadrature components one can obtain the dissipation and the resonance frequency (see Appendix B). A LabView program determined the resonance frequency from the input data and changed the frequency of the exciting signal in the Stanford generator to match the oscillator's resonance frequency.

To remove any ambiguity in the estimation of the resonant frequency when per-

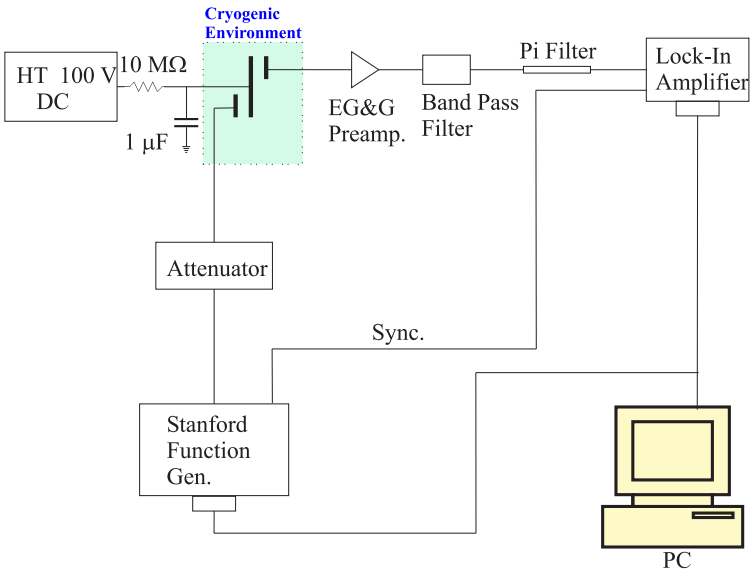

Figure 4.4: Experimental setup for the torsional oscillator experiment.

forming the experiment the lock-in amplifier should be set to detect components of the signal in phase and quadrature with the excitation in zero relative phase at resonance. This is achieved by doing a slow frequency sweep over a frequency span of ∼200 Hz around the resonant frequency. The relative phase of in-phase and quadrature is thus calculated and the phase in the lock-in amplifier changed accordingly. Figure 4.5 (a) shows a typical frequency sweep, done at a constant temperature of 10 mK. Also shown in the Figure (b) is the relative phase between the components as a function of frequency. The in-phase component (red line in Figure 4.5 a) and the quadrature component (black line in Figure 4.5 a) were squared and added together to obtain the squared modulus of the signal. The maximum of the squared modulus allowed us to determine the resonance frequency. The relative phase between the components could be calculated as $\arctan(Y/X)$ where Y is the in-phase component of the resonance and X is the quadrature component.

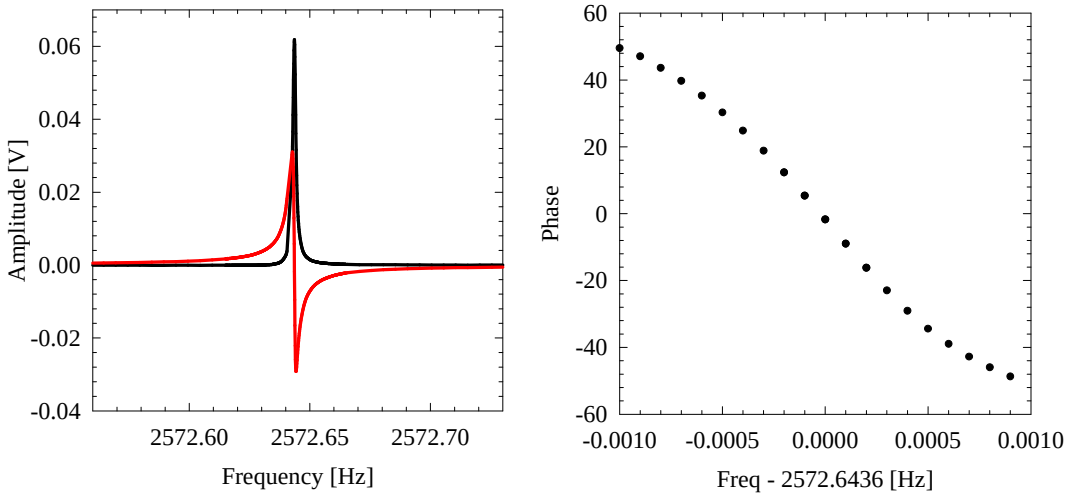

Figure 4.5: Typical frequency sweep done at 10 mK to determine the relative phase between the in-phase (red line) and quadrature (black line) components of the oscillator output signal (a). Also displayed is the relative phase as a function of frequency (b).

4.4 Normal fluid measurements

The results and data presented in this Section were obtained previous to this thesis but are included for completeness. They will help to understand the reasons that led to the design of the experimental cell used for the measurements on the superfluid phase. Further details can be found elsewhere [80].

4.4.1 Sample preparation

The range of film thicknesses studied in this first cell was from 100 to 300 nm. In order to get a reliable measure of the thickness of the film one needs to relate the

change in frequency observed when filling the oscillator with the mass of a ^{3}He slab.

The change in the resonant frequency is going to be related to the change in moment of inertia due to the mass loading according to

$$\frac{|\Delta f|}{f_o} = \frac{|\Delta I|}{2I}$$

where f_o is the resonant frequency and I is the total moment of inertia of the oscillating head. Consider now a slab of material of radius R, mass M and thickness h. The moment of inertia for the antisymmetric torsion mode is given by

$$I = \frac{1}{2}MR^2 = \frac{1}{2}\rho h \pi R^4$$

For two (top and bottom) films of thickness t, and since $I_{\mathrm{Head}} \gg I_{\mathrm{Liquid}}$, we can approximate the change in frequency as

$$|\Delta f| = \frac{\rho_{\mathrm{liquid}}\, t\, R^4_{\mathrm{slab}}}{\rho_{\mathrm{metal}}\, h\, R^4_{\mathrm{head}}} \times f_o \tag{4.1}$$

where h is the height of the head of the oscillator. The antisymmetric torsion mode resonance frequency for this oscillator was 2840 Hz. Hence, for two 1000 Å thick films we get a frequency-thickness conversion of 1 mHz/(2× 1000 Å), according to Equation 4.1. For our resonance frequencies and with our frequency resolution (better than 1 part in 10^9) our uncertainty in film thickness is of about ±40 nm (roughly half a coherence length) if we assume our annular ring model to be correct.

The sample growth method used in the torsional oscillator differs significantly from the method used in the NMR experiment (see Section 3.5.1). Figure 4.6 shows a typical filling procedure. A shot of ^{3}He was allowed into the filling system with

the fill line heated near 1 K and the oscillator stabilized at 60 mK[1]. That prevented the gas from condensing along the fill line and the liquid was formed initially inside the oscillator, but still outside the cell. Note that the copper isolator is the part which is thermally linked to the nuclear stage and it is, therefore, the coldest point of the device. The point at which the hollow tube running along the oscillator's body joined the clearance drill in the copper mass provided some dead volume. It is in this dead volume where the liquid probably condensed. The oscillator was then taken to 490 mK, where the saturated vapour pressure of ^{3}He is $\sim$ 0.1 mbar, in order to evaporate any liquid condensed outside the oscillator and make it condense inside the cell. The drop in frequency was monitored and the cell was cooled back down once the frequency was flat or we achieved the desired load. The typical loading rate was recorded to be around 0.1 mHz/h. The frequency shift at 60 mK was then converted into film thickness using Equation 4.1 and used as our nominal film thickness. The measurements reported in this section were obtained from films whose nominal thicknesses were 100, 240 and 350 nm. In Figure 4.6 we plot the difference between the inferred frequency at a given time and the frequency of the empty oscillator at 60 mK, f_o. At temperatures higher than 60 mK the background frequency drops dramatically (see Figure 4.7). That is the reason of the sudden change in frequency when the cell is heated to 490 mK. During the cool down from 490 mK to 60 mK some liquid probably condensed inside the oscillator's body and was poured inside the head by gravity. Part of the liquid, however, could have remained inside the body's hollow tube, to which the oscillator is insensitive. That could be the reason of the slight discrepancy between the loading at the two different temperatures shown in Figure 4.6. After each change in temperature the oscillator

[1]The reason for using 60 mK as a reference frequency is the maximum that the background frequency shows at that temperature, making it more stable against small temperature changes.

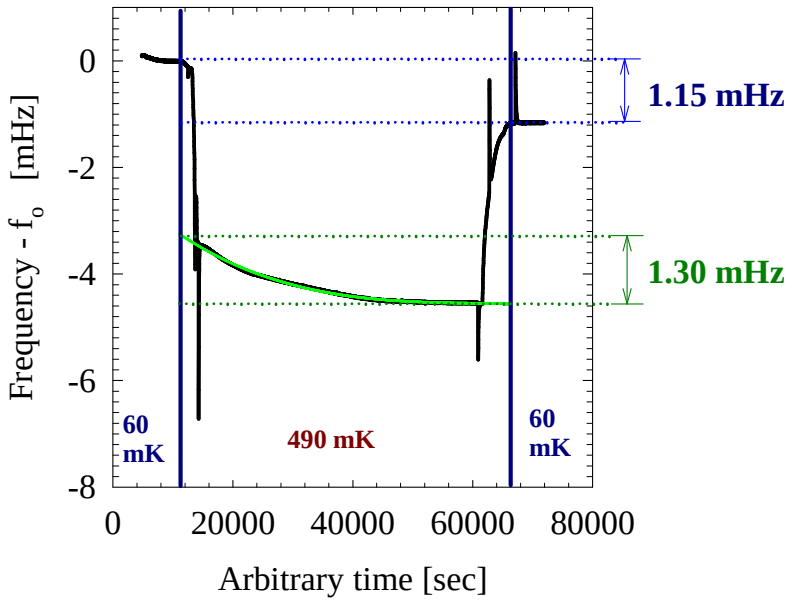

Figure 4.6: Typical filling procedure for the torsional oscillator. The black line represents the frequency minus the frequency of the empty cell at 60 mK (f_o). The green line is a polynomial fit to the frequency drop at 490 mK. See text for further explanation.

was retuned in order to obtain a reliable reading in frequency, as can be seen in the sharp features of the black line.

4.4.2 Results and discussion

For the normal liquid measurements, the temperature was measured and regulated using a ^{3}He melting curve thermometer mounted on the nuclear stage (see Appendix A). The empty cell temperature dependence of the frequency and the dissipation are shown in Figure 4.7. For each film studied, the frequency and dissipation empty cell backgrounds were subtracted. Figure 4.8 shows the frequency shift fraction together with the dissipation measured for several films. There is a flat region at high

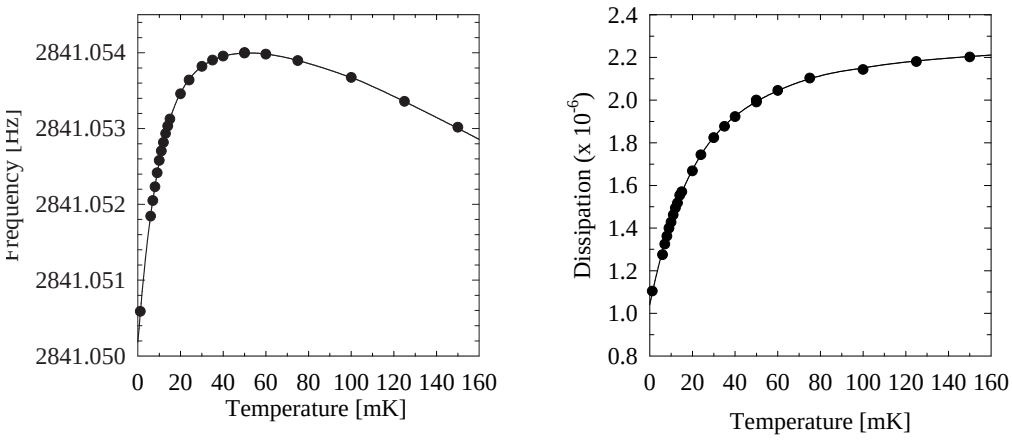

Figure 4.7: Frequency and dissipation temperature dependence for the empty cell.

temperatures (above 60 mK) in the fractional frequency shift, which is consistent with the film locked to the substrate. However, as the temperature drops below ∼60 mK the film starts to decouple. This behavior is independent of the mass loading. The decoupling is also reflected in the dissipation data, where all three film studied show a maximum at ∼ 10 mK. The maximum in the dissipation is a consequence of the liquid losing lock with the substrate and arises from the interaction between the oscillator and the liquid quasiparticles. All three films studied have about the same finite extrapolated frequency shift at $T = 0$. According to Landau-Tizsa two-fluid theory [84], [85] all the fluid should be decoupled at $T = 0$. Therefore, that residual frequency shift can be interpreted as capillary condensed liquid around the circular perimeter of the cell. The extrapolated frequency shift is equivalent to that of a 50 nm thick film on each surface.

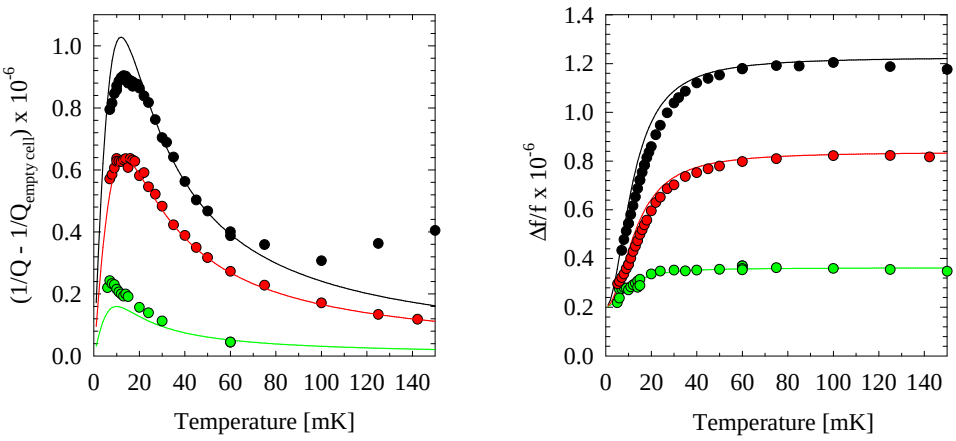

Figure 4.8: Fractional frequency shift and dissipation for nominal film thicknesses of 350 nm(black), 240 nm(red) and 100 nm(green)

The viscous penetration depth of ^{3}He at 100 mK is of the order of 5 μm and increases when the temperature decreases. The film should then behave as a rigid object locked to the oscillator throughout all the measured temperature range. Since this is not the case, surface slip must be taken into account in order to analyze these results. We can model the film as an mass m connected to the oscillator via a dashpot and with a damping force applied to it. The damping force per unit area is then given by the velocity of the film relative to the surface multiplied by a friction coefficient η. Solving the equations of motion for this system, we find that

$$\frac{x_o}{X_o} = \frac{1}{1 + i\omega\tau_{osc}} \tag{4.2}$$

where x_o and X_o refer to the oscillating amplitudes of the oscillator and film, re-

spectively, ω is the angular frequency and $\tau_{\rm osc}$ is a relaxation time defined by m/η with η the friction coefficient between oscillator and film.

From 4.2 it can be seen that for short relaxation times (small $\tau_{\rm osc}$) the phase of the complex denominator in the right is small and the film can follow the movement of the oscillator. As $\tau_{\rm osc}$ increases, so does the phase and for large relaxation times that is translated into a decoupling of the film (the film cannot "follow" the oscillator).

The effect of the film is to change the natural resonance frequency and quality factor (Q) of the oscillator:

$$\frac{\Delta f}{f_{\rm o}} = -\frac{m}{2M}\frac{1}{1+(\omega\tau_{\rm osc})^2} \tag{4.3}$$

$$\Delta\left(\frac{1}{Q}\right) = -\frac{m}{M}\frac{\omega\tau_{\rm osc}}{1+(\omega\tau_{\rm osc})^2} \tag{4.4}$$

From the frequency shift and dissipation data we can obtain $\omega\tau_{\rm osc}$ by simply dividing them. If we now plot $\omega\tau_{\rm osc}$ versus $1/T$ we observe a linear behavior (see Figure 4.9). The slope and m/M can be used as fitting parameters in equations 4.3 and 4.4 for the frequency shift and dissipation data after taking into consideration the thickness independent frequency shift at $T = 0$ (Figure 4.8). As it can be appreciated from Figure 4.8, these fits(represented by lines in that Figure) show reasonable agreement with the data.

Figure 4.8 also shows that the decoupling temperature depends on film thickness. The thinner the film, the colder the decouple temperature. As stated above, to enter the Knudsen flow the condition for the Knudsen number, $K_{\rm N} = \lambda/d$, is $K_{\rm N} \sim 1$. Therefore, going to a thinner film should make the inelastic mean-free path at which Knudsen flow is entered lower. That means entering the Knudsen flow at higher temperatures, since $\lambda \propto 1/T^2$. On the other hand, the Knudsen minimum has been

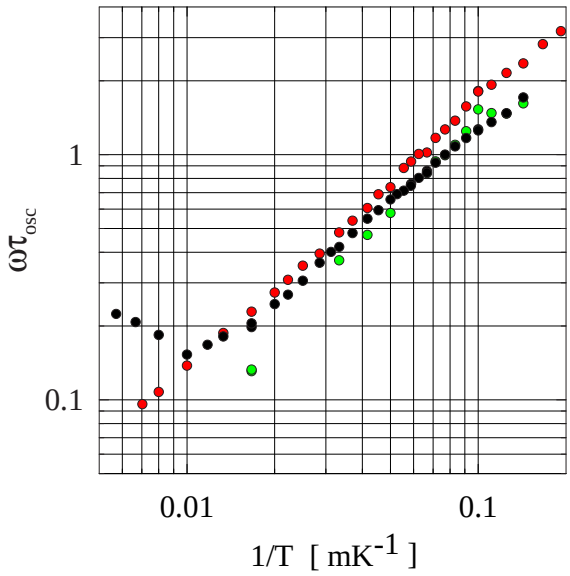

Figure 4.9: Temperature dependence of the relaxation time $\tau_{\rm osc}$ for nominal film thicknesses of 350 nm(black), 240 nm(red) and 100 nm(green)

measured to move to higher temperatures with increased specularity [86], which could be the case in this study, although no measurement has been done on this (like, for example, preplating the substrate with ^{4}He).

In order to explain the $1/T$ behavior of the film-substrate relaxation time, $\tau_{\rm osc}$, we can take into account four different times relevant to our problem:

- $\tau_{\rm osc} \propto 1/T$ (film-substrate relaxation time)
- $\tau_\eta \propto 1/T^2$ (quasiparticle relaxation time)
- $\tau_{\rm R} = m_3^* R^2/\hbar$ (characteristic of the surface)

- $\tau_{\mathrm{F}} = \hbar/(2E_{\mathrm{F}})$

where m_3^* is the ^{3}He effective mass, E_{F} is the Fermi energy and R is the correlation length. When $\tau_\eta \ll \tau_{\mathrm{R}}$ it can be shown [87] that

$$\frac{\tau_\eta}{\tau_{\mathrm{osc}}} = \frac{2\sqrt{2}}{3}\pi\left(\frac{\tau_\eta}{\tau_{\mathrm{F}}}\right)^{1/2}\left(\frac{l}{R}\right)^2\frac{1}{k_{\mathrm{F}}d} \tag{4.5}$$

where l is the height of the surface inhomogeneities (10 nm for our cell). The condition $\tau_\eta \ll \tau_{\mathrm{R}}$ is easily fulfilled in our case, since $\tau_\eta \sim 1.24 \times 10^{-6}$ s at 1 mK and $\tau_{\mathrm{R}} = 1.20 \times 10^{-5}$ s for a roughness size[2] of 300 nm. From equation 4.5 $\tau_{\mathrm{osc}} \propto \sqrt{\tau_\eta} \sim 1/T$ as measured. However, the dependence $\tau_{\mathrm{osc}} \propto d$ that the model predicts has not been observed, as commented above.

Another suitable way to measure τ_{osc} would be to measure the parameter (l/R). The surface characterisation of the substrate would give a value for l, whereas R could be inferred by studying the spatial distribution of the surface roughnesses and calculating their autocorrelation function. This function is given by

$$G(x,y) = \int_{-\infty}^{\infty}\int_{-\infty}^{\infty}\Psi^*(s,p)\Psi(s+x,p+y)\,\mathrm{d}s\,\mathrm{d}p$$

where the function $\Psi(x,y)$ describes the surface profile. Using now the definition of the inverse Fourier transform of a two-dimensional function

$$\Psi(x,y) = \frac{1}{(2\pi)^2}\int_{-\infty}^{\infty}\int_{-\infty}^{\infty}\psi^*(k_{\mathrm{x}},k_{\mathrm{y}})e^{i(k_{\mathrm{x}}x+k_{\mathrm{y}}y)}\,\mathrm{d}k_{\mathrm{x}}\,\mathrm{d}k_{\mathrm{y}}$$

[2]Equation 4.5 provides a way of inferring R/l, since all other parameters entering the expression are known. We obtain a value of $R/l \sim 30$

we can write

$$G(x,y) = \int_{-\infty}^{\infty} \mathrm{d}s \int_{-\infty}^{\infty} \mathrm{d}p \left[\frac{1}{(2\pi)^2} \int_{-\infty}^{\infty} \int_{-\infty}^{\infty} \psi^*(k_\mathrm{x}, k_\mathrm{y}) e^{-i(k_\mathrm{x}s + k_\mathrm{y}p)} \, \mathrm{d}k_\mathrm{x} \, \mathrm{d}k_\mathrm{y} \right] \times$$

$$\times \left[\frac{1}{(2\pi)^2} \int_{-\infty}^{\infty} \int_{-\infty}^{\infty} \psi^*(k'_\mathrm{x}, k'_\mathrm{y}) e^{i[k'_\mathrm{x}(s+x) + k'_\mathrm{y}(p+y)]} \, \mathrm{d}k'_\mathrm{x} \, \mathrm{d}k'_\mathrm{y} \right]$$

and, after rearranging terms and making use of the fact that

$$\int_{-\infty}^{\infty} e^{i(k''-k')s} \, \mathrm{d}s = 2\pi\delta(k'' - k)$$

we finally obtain

$$G(x,y) = \frac{1}{(2\pi)^2} \int_{-\infty}^{\infty} \int_{-\infty}^{\infty} |\psi(k_\mathrm{x}, k_\mathrm{y})|^2 \, e^{i(k_\mathrm{x}x + k_\mathrm{y}y)} \, \mathrm{d}k_\mathrm{x} \, \mathrm{d}k_\mathrm{y}$$

In other words, the autocorrelation function $G(x,y)$ of the surface profile $\Psi(x,y)$ is the inverse Fourier transform of the modulus squared of the Fourier transform of $\Psi(x,y)$. The interfacial friction model presented above assumes Gaussian correlations for the surface roughness [87]. Should this be the case for our substrate, the full width at half maximum of the autocorrelation function would give the value of R.

The decoupling of the normal liquid prevents the observation of superfluidity. That decoupling occurs because of long film-substrate relaxation times at low temperatures. In order to keep the normal fluid coupled to the oscillator, one would need to decrease the relaxation time. The design of a new cell aimed for that by adding randomly distributed elastic scattering centres. This is described in the next Section.

4.5 Superfluid measurements

The addition of elastic scattering centres to the cell's surface in order to drag the normal component of the liquid implied the fabrication of a new oscillator. This idea already appears in the torsional oscillator work of Freeman and Richardson [42] where the liquid was confined inside a set of Mylar sheets. To establish the spacing between the Mylar surfaces they added polystyrene microspheres which also fulfilled the function of pinning the normal liquid. The design and construction of our new cell were kept identical to those of the former undecorated oscillator. After polishing both surfaces and before making the diffusion bond we carried out the decoration of the surface.

4.5.1 Decoration procedure

The polished oscillator was placed on a teflon holder which covered the perimeter of the circular surface thus preventing particles from being deposited in the region where the copper gasket would later be placed. The holder creates a 14 mm diameter, 1 mm deep cavity in which a solution of particles in ethanol is poured. We used silver powder from Alfa Aesar consisting of spherical particles of 0.6 μm average diameter. The powder was 99.9% in purity. The surface to be covered was a circle of 14 mm (oscillator minus copper ring) diameter (1.54×10^{-4} m^2) and we aimed for a particle every $\sim 5\mu$m. That translates into $\frac{10^{12}}{25}$ particles/m^2 or 6.16 million particles to cover our surfaces. Taking into account the density of silver (10.49 g/cm^3) and the fact that each silver particle is a rough sphere of 0.6 μm diameter (which is equivalent to a volume of 1.13×10^{-19} m^3) we can infer that the mass of powder necessary for our purposes is 7.3 μg. This number was too small to be measured in our lab. We therefore prepared a suspension of silver powder in ethanol with

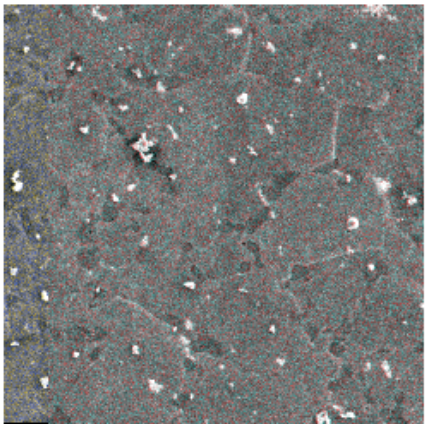

Figure 4.10: Electron micrograph of the oscillator's decorated surface. The shown area is $\sim 100\mu$m $\times 100\mu$m.

the adequate composition and covered the oscillator surface with it. The volume of the 14 mm diameter, 1 mm deep cavity is 1.54×10^{-7} m^3. From the density of ethanol, 0.789 g/cm^3, that volume is equivalent to 0.121 g of ethanol. Hence, the solution should have a ratio of masses 1:16.6$\times 10^3$ silver:ethanol. The 0.5 mg of silver powder measured was diluted in 10.53 cc (8.31 g) of ethanol. That dilution was used to fill up the cavity and the holder was placed in an ultrasonic bath until the ethanol evaporated. The ultrasonic bath caused the particles to be distributed randomly. The treated substrate was then brought to 755 °C for 10 minutes and then submerged inside ethanol in the ultrasonic bath to remove any loose particles.

The decoration was carried out in both halves of the oscillator's head and then the cell was diffusion bonded as explained above. Figure 4.10 shows a photograph of 100 μm $\times$ 100 μm area of the actual decorated surface. The white dots are the silver particles.

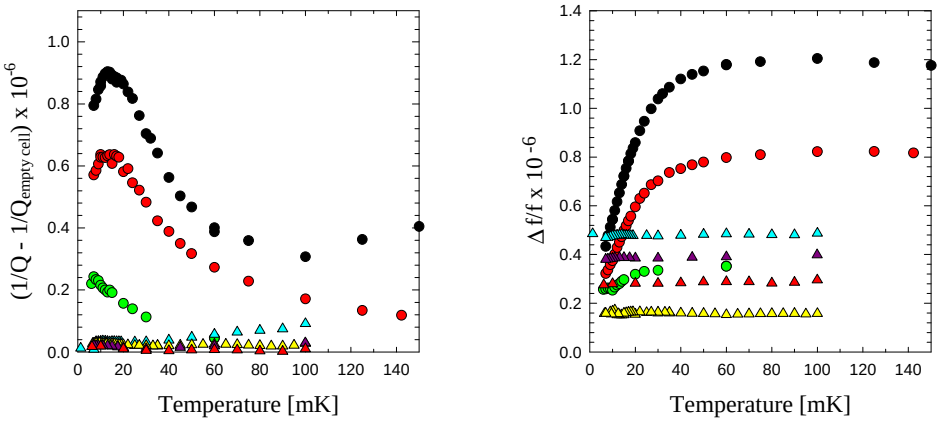

Figure 4.11: Fractional frequency shift and dissipation data comparing undecorated (circles) and decorated (triangles) oscillators. The film remains locked down to 1 mK in the new cell. Nominal thicknesses are 143 nm (cyan), 112 nm (purple), 84 nm (red) and 44 nm (yellow). The dissipation shows no peak as opposed to the previous undecorated cell, where the decoupling of the films was accompanied by a maximum in the dissipation.

4.5.2 Effect on the film

We studied films of different thicknesses in this new decorated oscillator. In this case, the resonance frequency of the antisymmetric torsion mode was ~ 2570 kHz. According to equation 4.1 the frequency to nominal thickness conversion was now 0.909 mHz/(2 $\times$ 1000 Å). Figure 4.11 displays the temperature dependence of the fractional frequency shift and dissipation for nominal film thicknesses of 143, 112, 84 and 44 nm. (where the residual frequency shift of 0.5 mHz. due to the annular ring suggested by Figure 4.8 has already been subtracted). It is clear the locking of the film to the substrate down to temperatures of the order of the millikelvin,

bordering the superfluid transition temperature. The dissipation data appears flat in contrast with the maximum observed in the data from the undecorated oscillator. These results reinforce the interfacial friction model presented earlier.

Our observations meant that the normal liquid was locked to the cell and that decoupling would only occur as a result of a superfluid transition. We present the superfluid results in the next Section.

4.5.3 Results and discussion

In these experiments we are able to cool below 0.5 mK, the total residual heat leak to the nuclear stage being about 4 nW at zero magnetic field. The thermometry below 1 mK is based upon the nuclear magnetic susceptibility of platinum wires (PLM thermometer explained in Appendix A). Two runs in the cryostat were performed with the decorated oscillator: Run 13 and Run 14.

In Run 13, after carrying out the decoration, we experienced some experimental problems with the oscillator. In this Run we observed a big change in the temperature dependence of the empty oscillator resonance frequency (see Figure 4.12). Also, the oscillator was found to be rather unstable upon perturbations: a helium transfer on the cryostat, a sudden change in temperature or the loading procedure, would cause a jump in frequency, thus making necessary to shift our background. Constantly adding and subtracting random shifts to the frequency was absolutely undesirable and, in fact, a clear superfluid transition in a film could not be determined. It also compromised the reliability of the determination of the nominal film thickness.

However, we did measure the response of three different samples of nominal film thicknesses 100, 180 and 300 nm (Figure 4.13). Below 0.90 mK all three films show

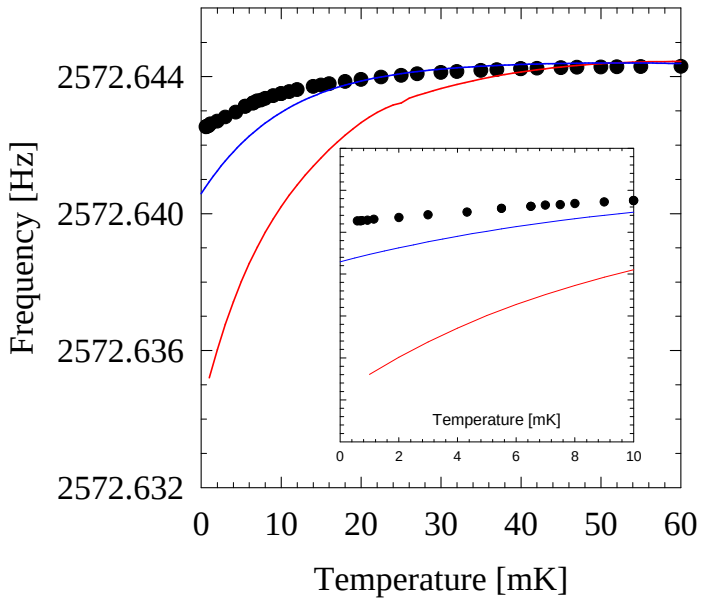

Figure 4.12: Background comparison between undecorated (blue) and decorated cells. The red line shows the background of the decorated cell during Run 13, where high instabilities were observed. After some changes in the cell (see text) the background became much flatter (black points) in Run 14. The inset is a blow up of the region below 10 mK.

a departure from the background. This was our first observation of a superfluid transition in the torsional oscillator and gave evidence of the effectiveness of the decoration method described above. The two thinner films show an increase in the momentum of inertia below 0.90 mK, contrary to what one would expect from a superfluid transition. Such a behavior is not well understood yet, although it could be a consequence of a redistribution of the liquid within the cell following the bulk transition. Further cooling made the 180 nm sample to actually decouple, reaching a total frequency shift of about 1.1 mHz at 0.30 mK. We never cooled down the 100 nm sample below 0.82 mK. The most striking feature from this set of data comes from the thickest film (red line in Figure 4.13). The magnitude of the sharp peak

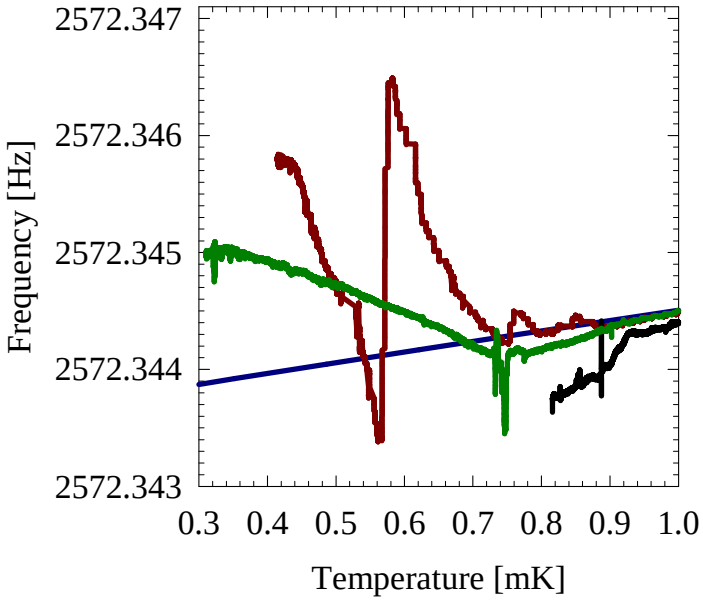

Figure 4.13: Sub-1mK data for samples of nominal thicknesses of 100 (black), 180 (green) and 300 (red) nm obtained in Run 13. All coverages show a departure from the background (blue line) below 0.90 mK. The thickest film shows a resonance which could be attributed to coupling with fourth sound.

is of the order of the total frequency shift from loading. It actually looks like the imaginary component of a resonance. This resonance is likely to arise from the coupling of the oscillator to some sound mode in the liquid. ^{3}He shows five different kinds of sound, some of them only observable on its superfluid form. Normal ^{3}He at high temperatures and low frequencies has only ordinary "hydrodynamic" or first sound. As the temperature decreases, a collisionless collective mode develops. That new mode is the zero sound [18], in which the quasiparticles do not come into thermal equilibrium locally but respond only dynamically. Zero sound is also observed in superfluid ^{3}He [88] and has an excitation frequency of the order of tens of MHz. Second sound [89] is characteristic of ^{3}He-^{4}He mixtures and arises from

the counter-oscillation of the normal and superfluid mass densities. Third sound, related to waves on the surface of a thin film of superfluid, has modes of frequencies of the order of Hz in superfluid ^{3}He [30]. Fourth sound [90], like third, is only related to the superfluid part of the liquid, and the normal fluid remains clamped [91]. It occurs in restricted geometries where the normal component is locked to the walls due to its viscosity while the superfluid is free to flow. The velocity of fourth sound $C_4 \propto \sqrt{\rho_s C_1^2/\rho}$, where C_1 is the velocity of first sound, ρ_s is the superfluid density and ρ is the total density. This means that fourth sound is for the superfluid the equivalent of first sound for the normal liquid. This could be used to measure the superfluid density. It is this mode that we believe was probably coupled to the 300 nm sample. We did not, however, investigate this effect in deeper detail.

Before running the oscillator again some minor changes were made on the system concerning the anchoring of the coaxial cables connected to the magnesium electrodes. These cables were probably acting as a mechanical link between the cell and the nuclear stage. Also, the fridge was run with the air mounts down which did not prevent us from cooling below 0.5 mK. As a result, the temperature dependence of the background frequency improved noticeably, as shown in Figure 4.12. Here, the black points were taken at several stabilized temperatures, whereas the blue and red lines represent fits to the measured backgrounds in the other two cases. Not only the instabilities completely disappeared after carefully rearrange the wiring, but the new background was less temperature dependent than that of the previous undecorated cell, which implied a better mass resolution for our samples.

We move on now to discuss the superfluid transitions observed in the new cell during Run 14. We made measurements on three different samples, of thicknesses 143, 112 and 83 nm, and for all of them we observed a bulk superfluid transition. This is shown in Figure 4.14, where the thicker lines represent the frequency and

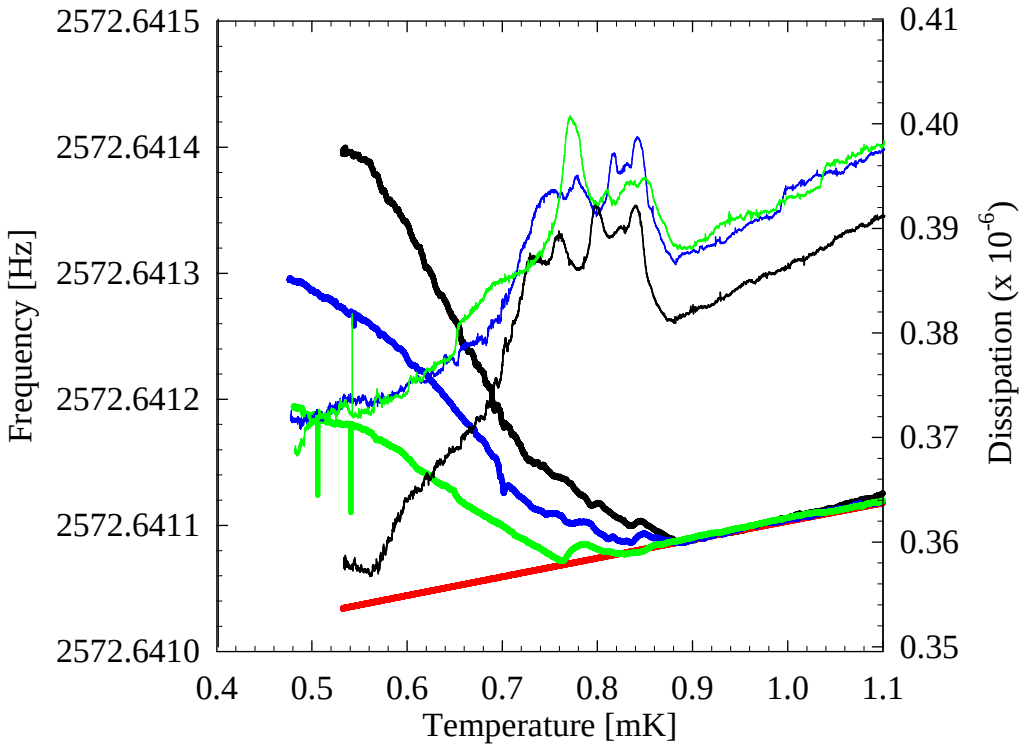

Figure 4.14: Sub-1mK frequency (thick lines) and dissipation (thin lines) data for samples of nominal thicknesses of 143 nm (black), 112 nm (blue) and 83 nm (green) in Run 14. Data were taken on warming. The red line represents the empty cell frequency background. See text for explanation.

the thinner lines represent the dissipation. These data were taken on warming. Evidence of a superfluid transition in the film was only found in two of the samples (143 and 112 nm): for both of them a sudden increase in slope (in the frequency data) occurs at 0.73 mK. All three samples showed a "bump" in the frequency at the beginning of their decoupling. This feature was more pronounced the smaller the nominal thickness of the sample. It happened around bulk T_c for the two thicker samples, but colder, at about 0.80 mK, for the 83 nm sample (green line in Figure 4.14) and it could be linked to a change in distribution of the liquid within the cell. For the 143 nm sample and the 112 nm sample the jumps in the dissipation at 0.88 mK coincided with the beginning of the frequency decoupling. We attribute

these jumps in dissipation, therefore, to a superfluid bulk transition in the capillary condensed liquid at the periphery of the cell.

The Ginzburg-Landau theory predicts a superfluid transition temperature of 0.21 mK for a 83 nm thick film. The coldest temperature achieved in our 83 nm sample was 0.48 mK and nothing in the data suggested that a superfluid transition occurred in a film. The behaviour in frequency of this sample near bulk T_c is not well understood. Its frequency joins the empty cell background at a temperature which is colder than the decoupling temperature of the two thicker samples. The dissipation, however, shows a jump around bulk T_c, agreeing with the observations made in the other two samples and revealing that the superfluid bulk transition also took place at 0.88 mK in the 83 nm sample. The two sudden drops in frequency at 0.50 and 0.54 mK were caused by helium transfers to the cryostat.

As commented above, the measured temperature for the superfluid bulk transition was 0.88 mK for all our samples. The ^{3}He bulk superfluid transition temperature is 0.94 mK at zero pressure and we believe that the reason for the disagreement in T_c shown by our data is a temperature gradient between the thermometer and the sample. Also, in Run 13 we measured a superfluid bulk transition temperature of 0.90 mK (see Figure 4.13). This difference in T_c between the two runs could be due to a change in the thermal resistance of the cone joint which provides the thermal link from the nuclear state to the PLM thermometer after the thermal cycle between the runs.

We will study now the film transition for our 143 nm and 112 nm samples. It is clear from Figure 4.14 that a sudden increase in the frequency slope occurs at 0.73 mK for both samples. The higher rate of decoupling can be attributed to the superfluid transition in the film. Now, both samples show the change in slope at the same temperature whereas they have different nominal film thickness. However, the

nominal film thickness was calculated under the assumption that the bulk liquid at the edge of the cell contributed with 0.5 mHz to the total frequency shift at loading. If we consider a smaller contribution from the bulk liquid at the edges for our 112 nm sample, the nominal thickness would be different. Specifically, a 0.3 mHz frequency shift from the edge at loading would mean a change in nominal thickness from 112 nm to 134 nm. That would also explain the slower decoupling shown by the blue curve in Figure 4.14 between 0.88 and 0.73 mK. We will consider these issues in the analysis below.

Let us analyze the 143 nm sample first. The reduced superfluid density is related to the change in period by

$$\frac{\rho_s}{\rho} = \frac{\Delta P}{(1-\chi)(\Delta P_{\text{load}})} \tag{4.6}$$

where ΔP is the change in period due to the superfluid decoupling and ΔP_{load} is the change in period observed when filling the cell up. Imperfections in the flow path could keep a fraction, χ, of the sample coupled to the oscillator, even when the liquid is completely superfluid. In their torsional oscillator experiment, Freeman and Richardson measured the χ factor of their oscillator using pure ^{4}He [92] and found a value of 0.27. Their substrate was Mylar and the samples were enclosed between two enclosed boundaries. They expected χ to be approximately half the measured value and attributed the discrepancy to an imperfect parallel plates geometry. Our case is slightly different, since our samples present a free surface and, therefore, have less contact area with the substrate. Since χ was not measured for our cell, we will take the χ factor as zero throughout our analysis.

In order to extract the superfluid film fraction and compare it with the predictions of the Ginzburg-Landau theory one needs to subtract the decoupling of the

bulk liquid capillary condensed around the cell perimeter. The reduced superfluid density as a function of temperature for bulk ^{3}He at zero pressure has been studied in the past [93]. In reference [93] we use the data from the Cornell group to get a bulk period shift that we can compare with our results. It is important to remember the role played by the bulk liquid at the edges when calculating that loading period shift. Let us consider that the bulk liquid is responsible for a total shift *in frequency* of 50 mHz. Now, when working in periods, we do the following:

$$\Delta P_{\mathrm{Total}} = \frac{1}{f_{\mathrm{o}} - 1.8 \times 10^{-3}} - \frac{1}{f_{\mathrm{o}}} = \Delta P_{\mathrm{Bulk}} + \Delta P_{\mathrm{film}}$$

where f_{o} is the frequency of the empty cell at the temperature at which our nominal film thickness is calculated (60 mK) and our sample had a loading frequency shift of 1.8 mHz in total. Now, of this total frequency shift of 1.8 mHz, 0.5 mHz come from the bulk. Therefore

$$\Delta P_{\mathrm{Bulk}} = \frac{1}{f_{\mathrm{o}} - 0.5 \times 10^{-3}} - \frac{1}{f_{\mathrm{o}}}$$

Hence, the period shift due to the film is simply

$$\Delta P_{\mathrm{film}} = \Delta P_{\mathrm{Total}} - \Delta P_{\mathrm{Bulk}}$$

One could, of course, argue that we could also calculate the change in period due to the film first and then obtain the bulk by subtracting it from the total. That calculation would give a film period change smaller than the above obtained by four parts in 10000. That means a difference in thickness of 0.6 Å, less than our thickness resolution (1 Å).

The bulk superfluid density experimental points can be fit in order to obtain a

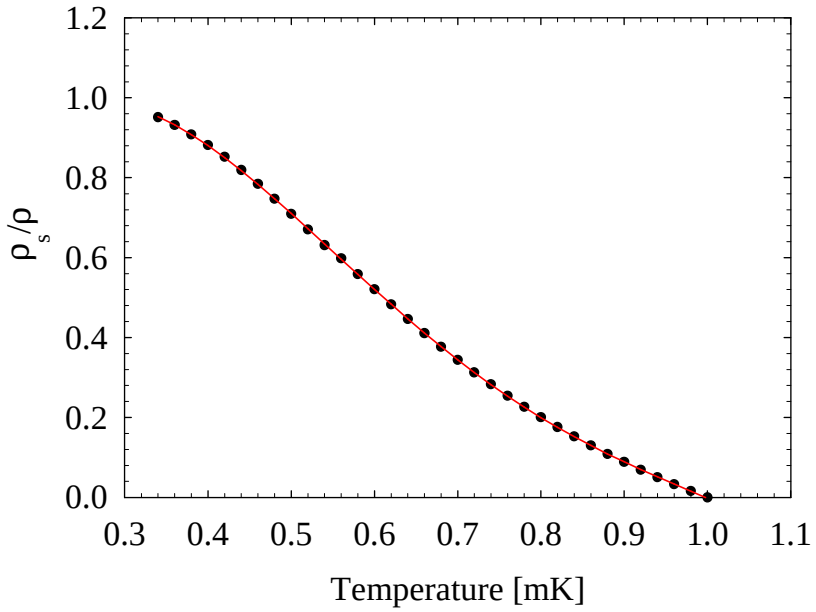

Figure 4.15: The bulk superfluid fraction for ^{3}He-B as measured at Cornell [93] at zero pressure as a function of temperature (black). The red curve is a fourth order polynomial fit to the experimental points.

curve with which compare our measurements. This is shown in Figure 4.15, where the discrepancy in the bulk superfluid transition temperature is due to temperature scale differences. By multiplying the red curve in Figure 4.15 by our ΔP_{Bulk} we can estimate what the period shift would be as a function of temperature following a superfluid transition in the liquid located at the periphery of our cell. For our 143 nm sample, assuming a 0.5 mHz frequency shift from the bulk liquid, the resultant curve is the red line in Figure 4.16, which also shows the measured period shift (black line) and the difference between both (green line). The agreement is remarkable down to $T/T_{\mathrm{c}} = 0.82$.

Below $T/T_{\mathrm{c}} = 0.82$ our data no longer follows the bulk data, indicating a possible transition in the film. We can now treat the bulk period shift as a background and

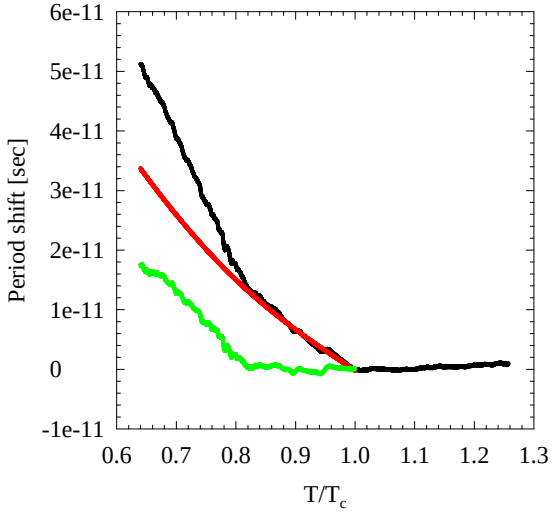

Figure 4.16: Period shift from our 143 nm thick film (black line). The empty cell background has been subtracted. The red line shows data from ref [93] scaled by our period change on loading. The green line is the difference between the black and red lines and reflects the behavior of the film.

subtract it from our data (green line). The resulting line is then divided by $\Delta P_{\rm film}$ to obtain the superfluid film reduced density (black line in Figure 4.18).

The Ginzburg-Landau theory provides an estimate of the superfluid density near T_c. For ^{3}He-A it has been calculated [26], [94], [95] that

$$\frac{<\rho_{\rm s}^{\rm A}>}{\rho_{\rm s,bulk}^{\rm A}} = 1 - \frac{k(w)}{w} \tag{4.7}$$

where w is the dimensionless thickness $D/\xi(T)$. Note that in our case, due to the specular boundary of the free surface, our thickness $d = D/2$. The function $k(w) = 3.2$ for $w >> \pi$ [96] in ^{3}He and varies slowly with w. Let us develop the above

expression a bit further by using the correlation length temperature dependence

$$\xi(T) = \xi_{\mathrm{T}}\left(1 - \frac{T}{T_{\mathrm{c}}}\right)^{-1/2}$$

The correlation length in superfluid ^{3}He has two components: one longitudinal and one transversal to the order parameter. It is the shortest one, the transverse component ξ_{T}, the one we use in this analysis following the conventional procedure [23]. This transversal component can be expressed as

$$\xi_{\mathrm{T}} = \sqrt{\frac{3}{5}}\,\xi_{\mathrm{s}}$$

where ξ_{s} is the s-wave BCS correlation length and is given by

$$\xi_{\mathrm{s}} = \sqrt{\frac{7\zeta(3)}{48}}\frac{\hbar v_{\mathrm{F}}}{\pi k_{\mathrm{B}} T_{\mathrm{c}}}$$

ζ is the Riemann zeta function and v_{F} is the Fermi velocity. The quantity $\hbar v_{\mathrm{F}}/\pi k_{\mathrm{B}} T_{\mathrm{c}}$ is the zero pressure, zero temperature coherence length for superfluid ^{3}He, ξ_{o}.

We can now write Equation 4.7 as

$$\frac{<\rho_{\mathrm{s}}^{\mathrm{A}}>}{\rho_{\mathrm{s,bulk}}^{\mathrm{A}}} = 1 - k\,\frac{\xi(T)}{D} = 1 - \frac{k}{2d}\,\sqrt{\frac{3}{5}}\,\sqrt{\frac{7\zeta(3)}{48}}\,\xi_{\mathrm{o}}\left(1 - \frac{T}{T_{\mathrm{c}}}\right)^{-1/2} \tag{4.8}$$

The film thickness is related to the film superfluid transition temperature by [26]

$$\frac{\xi_{\mathrm{o}}}{d} \sim \left(1 - \frac{T_{\mathrm{c}}^{\mathrm{film}}}{T_{\mathrm{c}}}\right)^{1/2}$$

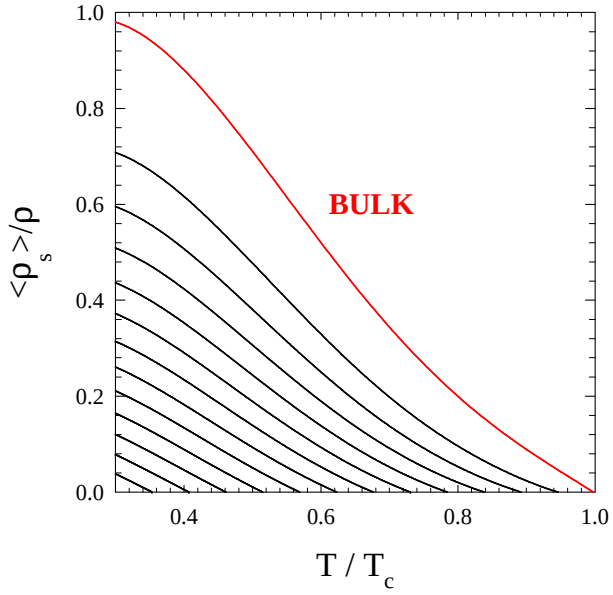

Figure 4.17: Ginzburg-Landau theoretical curves for the superfluid film fraction in different film thicknesses

and Equation 4.8 becomes

$$\frac{<\rho_{\rm s}^{\rm A}>}{\rho_{\rm s,bulk}^{\rm A}} = 1 - \frac{k}{2}\sqrt{\frac{3}{5}}\sqrt{\frac{7\zeta(3)}{48}}\left(1-\frac{T}{T_{\rm c}}\right)^{-1/2}\left(1-\frac{T_{\rm c}^{\rm film}}{T_{\rm c}}\right)^{1/2}$$

Operating and rearranging, we finally reach

$$\frac{<\rho_{\rm s}^{\rm A}>}{\rho_{\rm s,bulk}^{\rm A}} = 1 - 0.649\frac{k}{2}\left(\frac{T_{\rm c}-T_{\rm c}^{\rm film}}{T_{\rm c}-T}\right)^{1/2} \tag{4.9}$$

Using the superfluid bulk data of reference [93] and a constant value of 3 for the function $k(w)$, we can produce a family of curves describing the reduced superfluid density for a number of different $T_{\rm c}^{\rm film}$(Figure 4.17). However, the Cornell data [93] refer to an isotropic superfluid density, which is not the case for ^{3}He-A. For

an anisotropic superfluid we should use the z component of the superfluid density tensor, $\rho_s^{A,\perp}$. Although they are different, related by $\rho_s^{A,\perp} = 2\rho_s^B/5\beta_{245}$, they can be regarded as equal in the weak coupling limit [97]. In the strong coupling limit the error made in such an approximation is of the order of 10-20%.

Comparing our data with the Ginzburg-Landau prediction for a film with a transition temperature $T_c^f/T_c = 0.82$ we observe a reasonable agreement down to $T/T_c = 0.75$. This is shown in Figure 4.18. The Ginzburg-Landau theory also predicts a film thickness of 173 nm for a transition temperature of $T_c^f/T_c = 0.82$, our nominal film thickness being 143 nm for this sample. A possible explanation for this disagreement could be related to the larger thickness of the film on the bottom surface of the cell, as explained in Section 3.4.2.

A theoretical prediction for ρ_s/ρ as a function of film thickness near $T = 0$ that does not make use of the Ginzburg-Landau theory of phase transitions can be found in the work of Yamamoto *et al.* [29], which we will discuss below.

As a final remark, we would like to point out that the 143 nm sample was cooled down twice, in both cases showing identical responses in frequency and dissipation.

The previous analysis can be now be applied to our 112 nm sample. Figure 4.19 shows the period shift of this sample (thin blue line) along with the calculated period shift for a bulk sample contributing with 0.3 mHz (thick blue line) and 0.5 mHz (red line) at loading. The black line represents the period shift of the 143 nm sample. The period shift of the 112 nm sample agrees remarkably well with the blue thick line from $T/T_c = 1$ down to $T/T_c = 0.82$ and falls well below the red line. That reinforces the hypothesis of the capillary condensed bulk liquid contributing with 0.3 mHz frequency shift at loading. As discussed above, that would put the nominal thickness of this sample at 134 nm, probably slightly thicker at the bottom, consistent with the measured $T/T_c = 0.82$. The film superfluid transition is masked

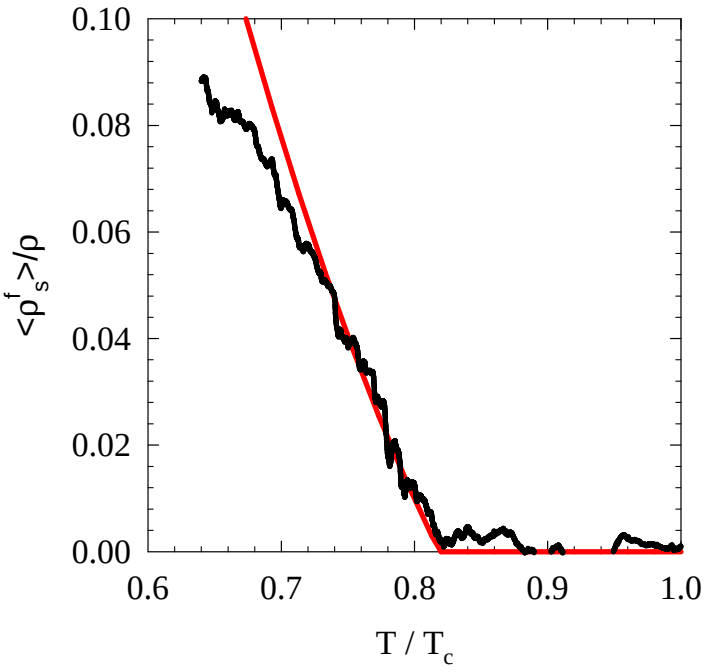

Figure 4.18: Superfluid film fraction from a 143 nm thick film (black) compared to the theoretical prediction for film with $T_c^f/T_c = 0.82$ (red). We observe a reasonable agreement down to $T/T_c = 0.75$.

by a sudden jump in the period shift at $\sim T/T_c = 0.8$, caused by a helium transfer to the cryostat. Under the light of these results, it seemed that we had actually formed a sample similar in thickness to our 143 nm sample. We could now also isolate the response from the film by subtracting the bulk period shift. This is shown in Figure 4.20. As it can be seen, both data set have a similar decoupling below $T/T_c = 0.82$, which suggests that both sampled actually consisted of films with similar thicknesses. If, as it can be inferred from the data, the amount of capillary condensed bulk liquid at the perimeter of the cell was not constant but changed with the samples, the growth of a film with a specific thickness would constitute a problem. Further research is necessary in order to understand this issue.

We will now compare the results from our 143 nm sample with other previous

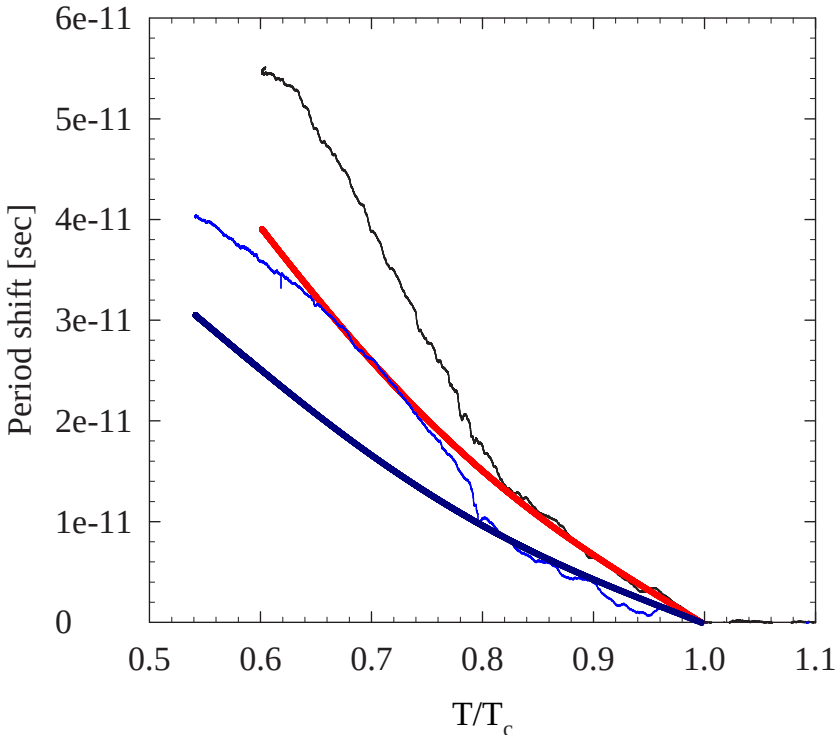

Figure 4.19: Period shifts from our 112 nm nominal thick film (thin blue line). The calculated bulk period shift considering a contribution of 0.3 mHz (thick blue line) and 0.5 mHz (red line) at loading are also displayed. The black line represents the period shift from our 143 nm sample. The empty cell background has been subtracted for all data.

experiments performed on similar systems. As presented in Chapter 2, the group at Purdue University [97] measured several film thicknesses ranging from 100 to 170 nm. They used a torsion pendulum and their samples, like ours, presented a free surface. Figure 4.21 shows their measured transition temperatures for several film thicknesses. The inset shows their experimental setup. Although their transition temperatures agreed within reason with the theoretical calculations of reference [25] (see Figure 4.21), their measured superfluid density was much lower than ours. As it can be seen in Figure 4.22, even for their thickest films ($\sim$ 160 nm) they never measured a superfluid fraction of more than 8% at $T/T\mathrm{c} = 0.4$ whereas we were obtaining a 9 % decoupling from the film at $T/T\mathrm{c} = 0.64$ (note that their

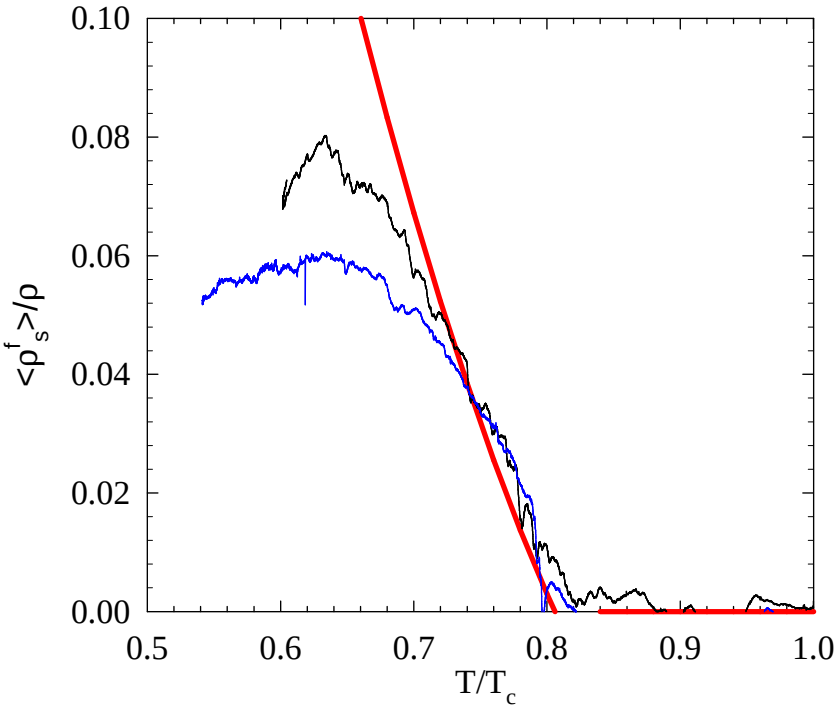

Figure 4.20: Superfluid film fractions from the 143 and 112 nm samples compared to the theoretical prediction for a film with $T_c^f/T_c = 0.82$. Both samples show similar behaviour below $T_c^f = 0.82$, suggesting that they actually consist of films with similar thicknesses (about 140 nm).

nominal thicknesses in Figure 4.22 are doubled to account for the free surface and, therefore, their empty squares are the closest to our 143 nm data). Interestingly, one of their measurements (on a film 137 nm thick) was done at nearly the same film thickness as ours. The measured reduced film transition temperature for this sample was $T_c^{film}/T_c = 0.82$. Their results showed an anomaly in the superfluid density at precisely this thickness. When they plotted $\rho_s/\rho_{s,bulk}$ as a function of the reduced film thickness $w = 2d/\xi(T)$, they found that their set of data fell into two different curves, determined by whether the film thickness was above or below 1375 Å. They suggested that a thickness dependent phase transition was taking place in the film. Since the Ginzburg-Landau theory [26] predicted a film thickness of 353

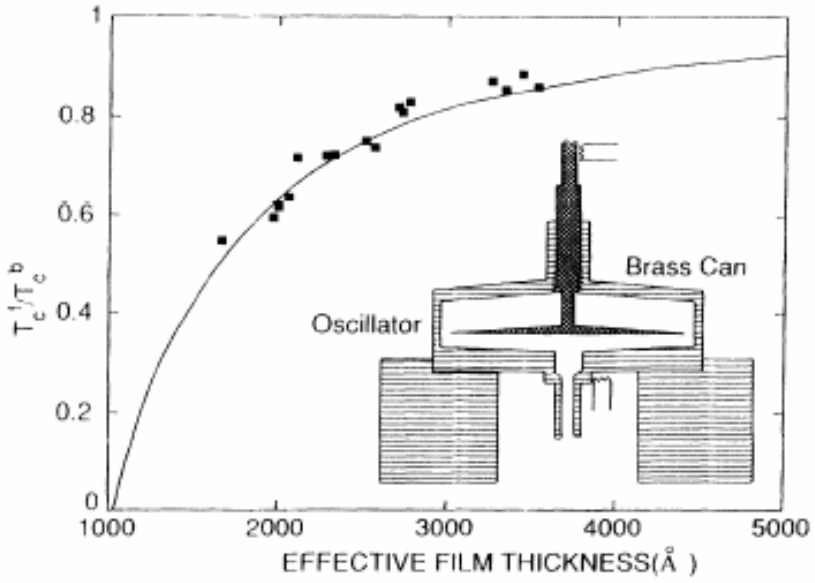

Figure 4.21: The transition temperature as a function of film thickness as measured by Xu and Crooker [43]. The inset shows the experimental setup.

nm, much thicker than their film, for the A-B transition to occur at a temperature $T/T_c = 0.82$ (see Figure 2.5) they suggested a non-B unidentified phase for their anomaly. We could not support or refute this last result with this work, since only one film thickness could be successfully studied, but Schechter *et al.* [30] (see below) never observed such a behaviour.

Schechter *et al.* [30] measured the superfluid fraction of thin ^{3}He films by using the third sound technique. Their range of thicknesses varied from 92 to 281 nm and observed reasonable agreement with the theory in the Ginzburg-Landau regime (see Figure 4.23). The samples were grown by positioning a thick horizontal copper disk in a container of ^{3}He. After the ^{3}He bath was cooled below the superfluid transition, the van der Waals attraction between the ^{3}He and the copper disk pulled ^{3}He atoms

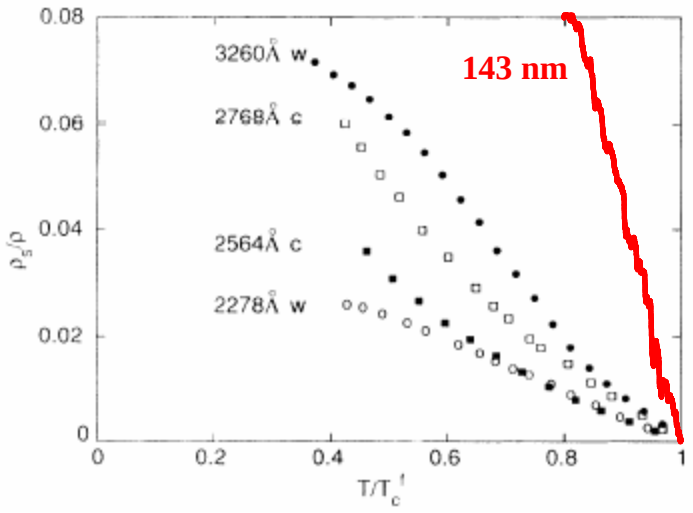

Figure 4.22: The superfluid density as a function of the temperature for several film thicknesses as measured by Xu and Crooker [43]. Data from this work are represented by the red line. The nominal thicknesses from the reference are doubled in order to account for the free surface. Our film thickness of 143 nm would be the closest, therefore, to the empty squares in the Figure.

onto the disk's exposed surface. The thicknesses of the films were governed by the energy balance between the gravitational force and the van der Waals interaction between the copper and the ^{3}He and they could be determined by using the substrate as one side of a parallel plate capacitor (the other side being a suspended plate above the sample) and taking into account the dielectric constant of ^{3}He (~ 1.0426). The capacitance increased, thus, linearly with the film thickness. This method had the disadvantage of a possible tilt in the capacitor plates and they relied, therefore, on the alternative parameter h, the height from the surface of the bulk liquid to the surface of the film. h was related to the film thickness by a power law. However, they found discrepancies between the film thicknesses measured on two differen runs

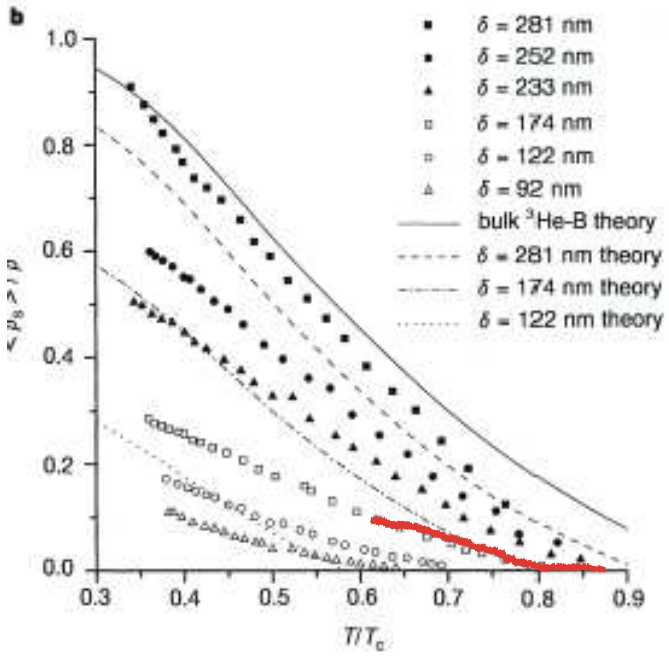

Figure 4.23: Superfluid densities as a function of temperature as measured by Schechter *et al.* [30]. Discrete points are experimental results whereas lines represent the Ginzburg-Landau predictions. Data from this work are plotted for comparison (red line).

and estimated a consistent error of up to $\sim 15\%$ in those measurements.

Comparing our results with the third sound experiment we see that for a film with a transition temperature of $T_c^f = 0.82T_c$ our data are in good agreement down to the coldest temperature we achieved. This can be seen in Figure 4.23, where we plot our superfluid density as a red line. Their nominal thickness for a film with $T_c^f/T_c = 0.82$ was 174 nm, whereas our nominal film thickness for the same transition temperature is 140 nm. Interestingly, there is a discrepancy between our Ginzburg-Landau calculated curves (see Figure 4.17) and the theoretical curves in Figure 4.23. Unfortunately, Schechter *et al.* did not report the source of the bulk superfluid data they used in their analysis.

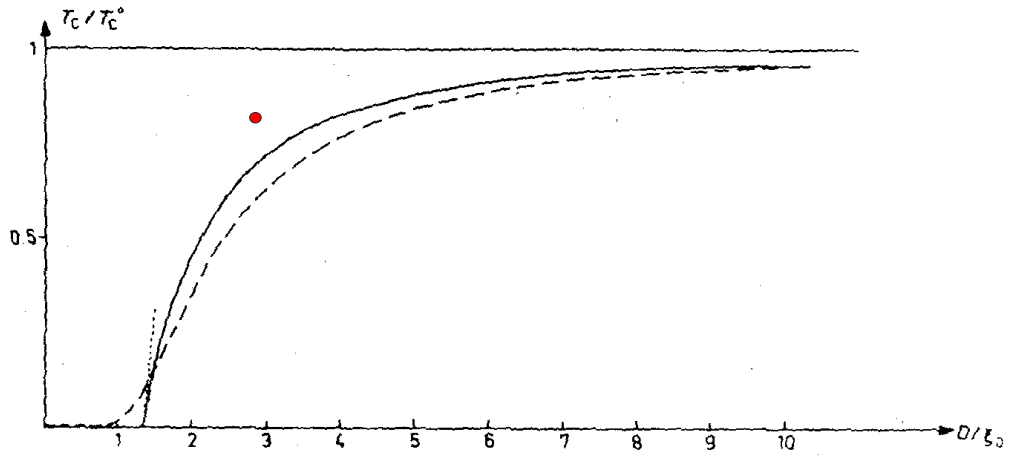

Figure 4.24: Theoretical dependence of the transition temperature with film thickness after Kjäldman *et al.* [25]. The red point represents this work, with the nominal film thickness multiplied by two to account for the free surface. See text for further explanation.

With regard to the existent theories, we observe a slight discrepancy with respect to the work from Kjäldman *et al.* [25]. This is shown in Figure 4.24. The red point represents our data after multiplying the nominal film thickness by two in order to account for the free surface of our film. According to that work, a transition temperature of $T_c^f/T_c = 0.82$ would correspond to a film of thickness 2×177 nm, in fairly good agreement with the third sound experiment. The theoretical work of Li and Ho [27] would attribute the same transition temperature to a slab of thickness 2×186 nm. Our nominal film thickness assumes an equal distribution of the sample between the top and the bottom of our cell but it well could be the case (see Section 3.4.2) that the bottom film is actually thicker than the top one. Actually, for a total

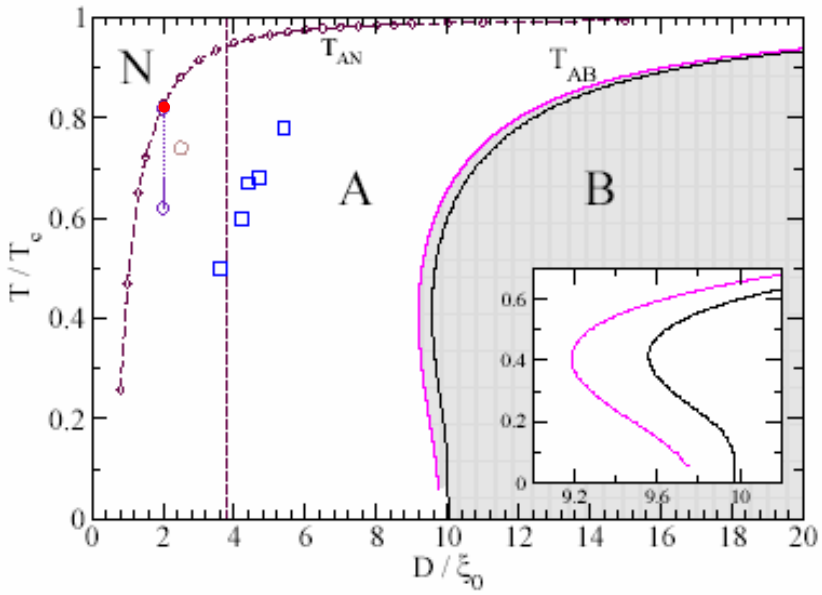

Figure 4.25: Theoretical dependence of the transition temperature with film thickness after Vorontsov and Sauls [28]. The red point represents this work. See text for further explanation.

thickness (top plus bottom) of 286 nm, our model predicts a $\sim$ 200 thick film at the bottom surface.

The most recent theoretical treatment of this kind of systems [28] (see Chapter 2) is in better agreement with our results, as shown in Figure 4.25. As stated in Chapter 2, this calculation refers to a film with one diffusive and one specular scattering surfaces, as it is our case. Our measurement is represented by the red point in Figure 4.25.

Another model which considers a film enclosed by a rough wall and a free surface [29] obtains the current density through quasi-classical Green's functions. This work reports a slightly higher superfluid fraction for a 174 nm sample than the measurements by Schechter *et al.* [30]. A comparison between this model, the third

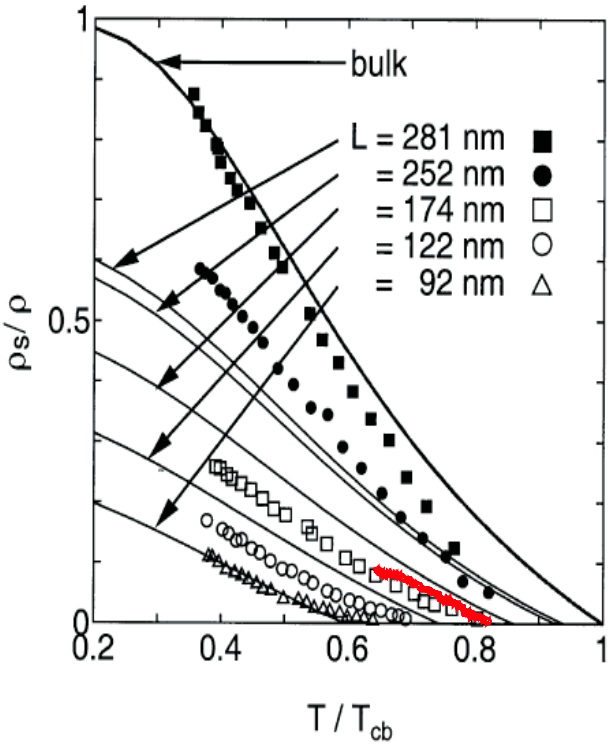

Figure 4.26: Temperature dependence of the superfluid density for various film thicknesses after Yamamoto *et al.* [29] (black lines). The symbols denote the work by Schechter *et al.* [30]. The red line represents our work.

sound data and our data is displayed in Figure 4.26. Data from our work would fall between their 122 nm and 174 nm calculations.

It is interesting to compare our experimental results with other work not necessarily involving restricted geometries such as superfluidity of ^{3}He in porous media. One of these porous media, extensively used in ^{3}He experiments is aerogel. Aerogel is a tenuous random solid network of SiO_2 particles of approximately 25 Å in radius with very low densities and large surface area. In the commonly accepted picture, it does not behave like a surface, since the silica diameter is smaller than the ^{3}He superfluid coherence length, but rather like a collection of impurities. However, qualitatively the effect of the aerogel on superfluid ^{3}He is the same as that of

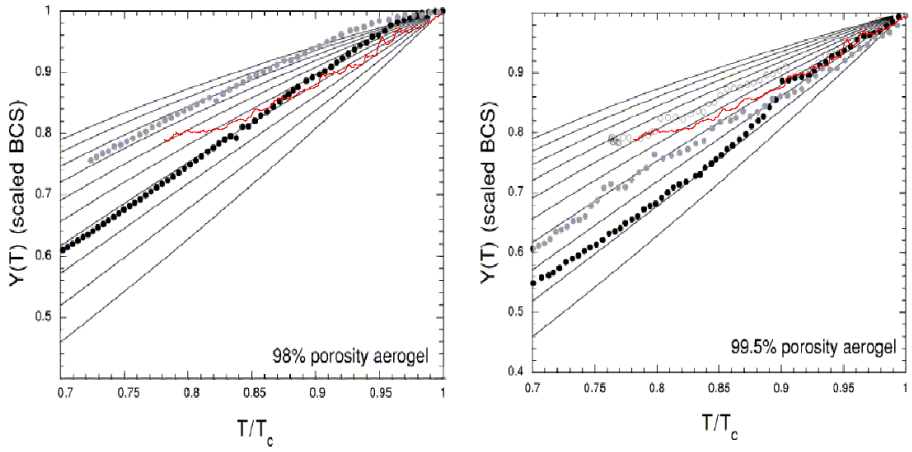

Figure 4.27: Temperature dependence of the bare normal fluid density in 98 % (left) and 99.5 % (right) aerogel after Lawes and Parpia [98]. The solid symbols are at 25 bars of pressure, the gray symbols at 10 bars and the open symbols at 2.5 bars. The red lines represent this work. The solid lines are the scaled BCS Yosida functions [98] with gap scaling factors of (from bottom to top) 1, 0.91, 0.83, 0.77, 0.71, 0.67, 0.63, 0.59, 0.56 and 0.53, showed for comparison.

confinement: both the superfluid density and the transition temperature are suppressed by the aerogel. Figure 4.27 shows a set of measurements done in 98 and 99.5 % open aerogels at several pressures [98]. It represents the bare normal fluid density versus the reduced temperature. The bare normal fluid density accounts for the pressure-dependent adjustment to the normal fluid density arising from Fermi liquid corrections to the effective quasiparticle mass. It is given by

$$\frac{\rho_{\mathrm{n}}^{\mathrm{b}}}{\rho} = \frac{\frac{\rho_{\mathrm{n}}}{\rho}}{1 + \left(\frac{F_1}{3}\right)\left(1 - \frac{\rho_{\mathrm{n}}}{\rho}\right)}$$

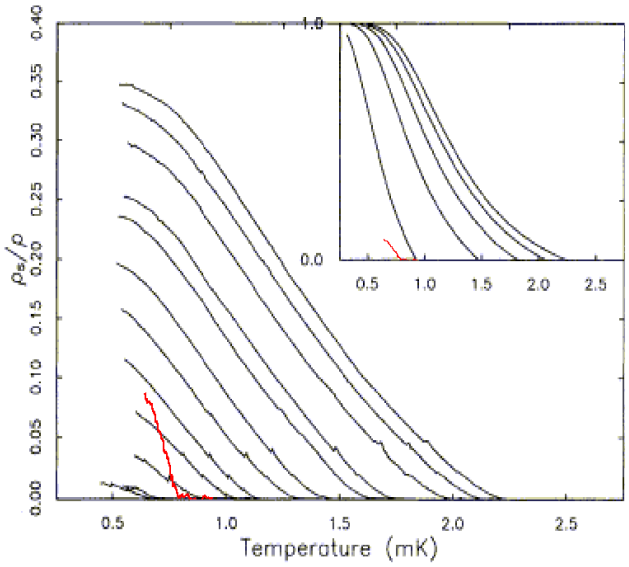

Figure 4.28: The superfluid fraction in 98 % open aerogel at various pressures as a function of temperature after Porto and Parpia [9]. The curves correspond to, from left to right, 3.4, 4.0, 5.0, 6.1, 7.0, 8.5, 10, 13, 15, 20, 25 and 29 bars. The inset shows the superfluid fraction in the bulk for 0.5, 10, 15 and 20 bars over the same temperature range. The red lines represent this work.

where F_1 is the pressure-dependent Landau parameter (5.27 at zero pressure) and ρ_n/ρ is the measured normal fluid density. From the figure we can see that our data displays a behaviour which does not correspond to any of the pressures displayed either in the 98 % or the 99.5 % aerogel. The slope of the bare normal fluid density versus temperature is smaller in our experiment than in the aerogel studies. Likewise, if we produce a plot equivalent to Figure 4.17 for a given aerogel density, as shown in Figure 4.28, we find that our superfluid density does not agree with the superfluid density in aerogel for a similar transition temperature. Figure 4.28 represents the superfluid fraction, ρ_s/ρ, at various pressures as a function of tem-

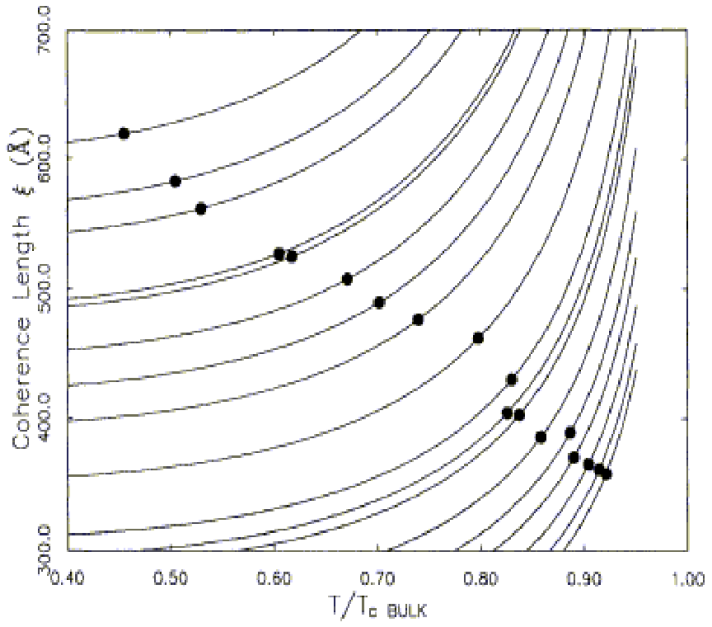

Figure 4.29: The bulk temperature dependent coherence length for different pressures plotted against the reduced temperature. The dots represent superfluid transitions in 98 % aerogel after Porto and Parpia [9]. Superfluidity does clearly not occur at a fixed value of the bulk temperature dependent coherence length.

perature for 98 % aerogel [9]. Whereas our superfluid fraction (red curve) is steeper than any of the aerogel curves, our superfluid transition temperature corresponds to a pressure somewhere between 4 and 5 bars in 98 % aerogel. This should not be surprising at all, since we should realize that there is a big difference in the physics of superfluid ^{3}He between confined geometries and aerogel. In the case of a regular slab geometry, such as the experiments reported in this work, the behaviour of the superfluid reflects the temperature and pressure dependence of the coherence length. In other words, the onset of superfluidity for all pressures occurs at a fixed $\xi(T)$ for a given film thickness. However, this is not the case for ^{3}He in aerogel [9]. Figure 4.29 displays the bulk temperature dependent coherence length for different pressures.

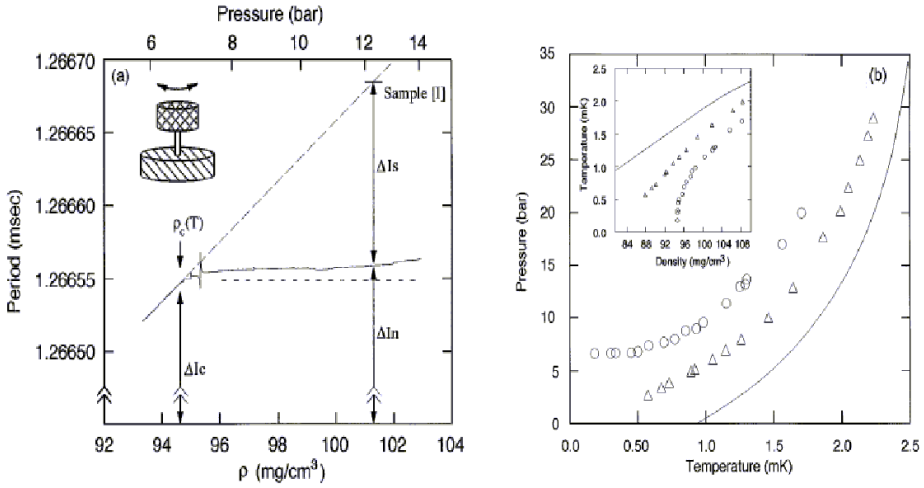

Figure 4.30: A pressure sweep from 14 to 5.6 bars at a fixed temperature $T = 0.295$ mK for ^{3}He in 98 % aerogel using a torsional oscillator, after Matsumoto *et al.* [99] (a). The measured period falls below a critical density (pressure) signaling the onset of superfluidity. Repeating that measurement over a range of temperatures, we can map out the phase diagram of ^{3}He on 98% aerogel (b). The solid line is ^{3}He in bulk, circles are data from Matsumoto *et al.* [99] and triangles are data from Porto and Parpia [9], also for 98% aerogel.

At each pressure the bulk coherence length at the transition temperature is shown as a dot. It is evident that the superfluidity is not manifested at a fixed value of the bulk $\xi(T)$.

The work in aerogel, nevertheless, could be taken as a starting point for finding evidences of Quantum Phase Transitions (QPT) in ^{3}He systems [99]. In the work by Matsumoto *et al.* they found, as Figure 4.30 shows, that there was a critical ^{3}He density (pressure) below which the system exhibits superfluidity for each fixed temperature. By changing that temperature, they could map out the Pressure-

Temperature phase diagram at low temperatures. Extrapolation of the data showed that the normal-superfluid phase boundary intersected the pressure axis. There was, therefore, a normal to superfluid *continuous* phase transition at $T = 0$ at a nonzero pressure. This results suggest that a similar effect could take place in ^{3}He in restricted geometries. For a film thickness smaller than one coherence length and at saturated vapour pressure, superfluidity would not be observed, even at zero temperature, according to Figure 4.25. In order to observe superfluidity in those conditions, pressure should be applied to diminish the zero temperature coherence length. Therefore, an experiment could be designed that would measure the superfluid density as a function of the film thickness at a fixed temperature. Since a continuous change of film thickness at constant temperature is not possible with our present setup, we could vary the pressure instead, and measure the superfluid density as done in Reference [99]. It is for this reason that the torsional oscillator experiment could also benefit from a confined cell such as the one described in Chapter 3. Changing the temperature for each measurement and then extrapolating in the same way as Matsumoto *et al.* would experimentally solve the low temperature region of the superfluid phase diagram as a function of film thickness. Of course, similar experiments could be done using the NMR technique.

4.5.4 Conclusions

Two different very sensitive torsional oscillators were used to measure the temperature response of films with different thicknesses. A superfluid state could never be seen in the first of our cells due to a decoupling of the liquid in the normal state. This effect could be explained by an interfacial friction model which supported a $1/T$ dependence of the film-substrate relaxation time.

A new decorated cell, to which silver particles were added to the substrate in order to lock the film, allowed us to observe superfluid transitions over a certain range of samples. For two of our samples, with nominal thicknesses of 112 and 143 nm, we observed a superfluid transition that agreed, in both cases, with the Ginzburg-Landau prediction for a slab of 173 nm and a transition temperature of $T_{\rm c}^{\rm film} = 0.82$ mK. That suggested that the two films actually had the same thickness and that the amount of capillary condensed bulk liquid at the edge of the cell was not constant over the samples.

Our results were in reasonable good agreement with some theoretical [25], [28], [27], [29] and experimental [30] works, whereas our measured superfluid film fraction presented a significant departure from the results of another torsional oscillator experiment [43].

A comparison between our experiment and other experiments dealing ^{3}He in porous media, like aerogel, was also done. We found that, although in both cases the order parameter of the superfluid was strongly affected by the media, the physics of confined ^{3}He is completely different from the physics of ^{3}He in aerogel, which is believed to be a disordered system.

Chapter 5

Conclusions and future work

Every saint has a past and every sinner has a future.

Oscar Wilde.

This work had as a purpose to study superfluid ^{3}He confined to a planar geometry of size of the order of the coherence length. Two main experimental techniques were used for this study: Nuclear Magnetic Resonance, which explored the magnetic features of the superfluid state and a torsional oscillator based on its flow properties. The NMR experiment was successful in observing superfluidity in samples of thicknesses ranging from about one to ten coherence lengths (93 to 1500 nm thick films), whereas the torsional oscillator experiment showed evidence of superfluidity in two samples. Although with different nominal thicknesses, 112 nm and 143 nm, these two samples exhibited a very similar response below 0.73 mK, suggesting that they were formed by films of similar thickness. We summarize in this Chapter the results obtained and suggest possible directions for future experiments which might stretch the limits of the current experimental capabilities.

5.1 NMR summary

The NMR cell design for this experiment was based on the previous work from Dyball [51]. In that work, the NMR cell consisted of a single silver surface enclosed in a stycast chamber. The ^{3}He samples within that cell were observed to be unstable at all temperatures, probably due to temperature gradients which made the liquid move towards the hotter part of the cell. By employing two silver discs we could obtain a similar thermal environment throughout the experimental substrate and there was no sign of signal decaying over a period of weeks. The cell fill line was also designed to avoid any space in which the liquid could allocate by capillary condensation.

In the NMR experiment we observed superfluid transitions on samples of different sizes. Most of our samples showed a positive frequency shift below the superfluid transition, which was inconsistent with a liquid film deposited on the cell substrate. They also had the same transition temperature independent of the sample size. Those facts, together with the results of the sample imaging using the magnet shim coils, suggested that our samples were imperfectly annealed and consisted of small droplets scattered over the silver plates. In thicker samples, consisting of a 1.8 μm thick film, we observed a signal splitting below the superfluid transition, always after a previous superfluid transition which we believed acted as a "superfluid anneal". The split was observed between 0.82 and 0.80 mK and further cooling would make the signal to snap into a single, positively shifted peak. We explained these results under the light of the spin wave theory. Also for this later sample, a transition into a superfluid B-phase, for which the magnetisation decreased as the temperature was lowered and the NMR signal remained at the Larmor frequency, was observed. This transition into the B-phase could not be reproduced again, even after reannealing

the sample following the same experimental steps. For an even thicker sample, equivalent to two films of 1500 nm on the top and bottom surfaces, but probably consisting of a single 3000 nm thick film in the bottom surface, we finally observed a negative frequency shift, also after a superfluid anneal, indicating the presence of an uniform and stable film within the cell. This was consistent with a supercooled A-like phase in a film. The transition temperature of this transition could not be precisely determined, though, due to the fact that it was observed on cooling and the thermometer could not reach thermal equilibrium with the sample during the demagnetization. The A-phase showed a sudden transition into the B-phase after about 20 hours. During the warm up of the B-phase, no subsequent observation of the A-phase was possible before the transition into the normal state.

These results proved how important was the sample annealing for obtaining a well characterized film. Our sample growth method probably suffered from imperfections. The samples were taken to 200 mK after the gas had been allowed into the cell. However, the vapour pressure of ^{3}He at 200 mK is of the order of 10^{-4} mbar and that was certainly not enough to properly anneal the samples. The reason for not going above 200 mK was that the experimental cell was the coldest part of the NMR system and at that temperature we observed inside it the total amount of spins added to the fill line.

5.2 Torsional oscillator summary

A previous torsional oscillator experiment on a similar cell showed that the liquid started to decouple at temperatures as high as 60 mK. This decoupling made impossible the observation of superfluidity. The frequency shift extrapolated to a value which was independent of the sample size. That suggested a model in which the

sample was formed by two films adsorbed on the top and bottom surfaces of the cell plus a sample independent capillary condensed ring around the edges of the cavity.

The normal fluid results were explained with the help of a facial friction model. In order to drag the normal fluid the model concluded that the quasiparticle-substrate relaxation time should be decreased. A new cell was designed and constructed which shared all the characteristics of the former one but was decorated with silver particles of 0.6 μm diameter on average. The particles, spaced about 10 μm from each other, acted as elastic scattering centres and the new cell was successful in keeping the normal fluid locked down to the superfluid transition temperature.

In a first attempt on the new cell a clear superfluid transition in the film could never be observed, due to the high level of noise in the oscillator's background. However, we observed an interesting feature in a 300 nm thick film. For this film both, the resonance frequency and dissipation below the superfluid transition, strongly resembled the real and imaginary part of a resonance. This was thought to be due to fourth sound coupling to the oscillator. Although it was not investigated further, this sound coupling could be used as a tool for obtaining the superfluid density in films over a certain range of thicknesses.

After making some changes in the anchoring of the electrodes wiring and running the experiment with the cryostat's air mounts down, which resulted in a much more stable and flat background, we could observe two clear superfluid transitions coming from a $\sim$ 140 nm thick film. These transitions came from samples of different nominal thicknesses, but they showed, after subtracting the empty cell background and the effect of the capillary condensed liquid in the corners of the cell, the same behaviour below 0.73 mK. This transition temperature was consistent with the work of Vorontsov and Sauls [28], but slightly discrepant with the work of Kjäldman *et al.* [25]. However, a balanced distribution of the liquid between the top and the bottom

surfaces of the cell was unlikely: the bottom film was expected to be thicker and, in this case, it could be as thick as 200 nm. Our results agreed with the work on third sound from the Cornell group [30] regarding superfluid density for a film with the same transition temperature, although their nominal thickness was about 35 nm larger than ours. The group at Purdue, however, reported much lower superfluid densities for similar thicknesses.

Comparing our results with work carried out in disordered systems, such as ^{3}He in aerogel, we found that, for similar transition temperatures, the slope of the superfluid density versus temperature of our films was steeper. A possible explanation for this could be that for a ^{3}He slab the superfluid transition takes place at a fixed temperature dependent coherence length $\xi(T)$ for all pressures, whereas this is not the case for ^{3}He in aerogel.

5.3 The road to the future

The study of superfluid ^{3}He films under confinement could benefit from several improvements in our experiments. First of all, for our current cells, a mechanism to obtain a direct measure of the film thickness like, for example, the inclusion of a parallel-plate capacitor could remove most of the uncertainty in our nominal film thickness.

The problem of capillary condensation on the edges of the cavity could be overcome by using a nanofabricated cell with a gap of the order of a few hundred nanometers. In such a cell, the spacing would be fixed and completely filled with ^{3}He. The coherence length, and therefore the reduced thickness, could be changed by applying pressure. The main problem with this kind of cell is that the coherence length has its maximum at saturated vapour pressure, so the reduced thickness could only be

increased for a given gap height. A gap small enough to allow the study of both, the very thin film regime and the A-B transition region of the phase diagram, would become necessary. This confined cell should be machined out of a material which could be polished to the desired level of flatness and, at the same time, be strong enough to stand the high pressures (several tens of bars) necessary to cover an appreciable region of the phase diagram. The main candidates are silicon and glass. A group in Cornell, led by Professor Jeevak Parpia, is already working on that project.

The NMR spectrometer could be also improved to have a lower noise temperature and, therefore, lower noise level. This could be achieved by using a SQUID without APF, since our measurements suggested that the inductive coupling between the APF and the input coil was the cause of our high noise temperature. Our group has achieved in the past noise temperatures of the order of 100 mK in similar spectrometers [51]. The use of SQUID arrays as a multistage amplifier has also been considered and it is currently being developed.

Regarding the measurements presented in this work, the current setup could certainly be exploited further. An effective sample growth method has only been learnt for the torsional oscillator cell, and further investigation is necessary in order to understand the way samples grow in the NMR cell.

In addition to the ideas stated above, one could consider adding ^{4}He to the substrate in order to obtain a specular boundary for the ^{3}He quasiparticles. This preplating would allow the study of the effect that the boundary conditions have on the order parameter of the confined superfluid.

5.4 Final remark

In summary, we have explored a small part of the phase diagram of superfluid ^{3}He under planar confinement. We have found the superfluid transition on two 140 nm thick films using the torsional oscillator technique. These results agreed with third sound experiments performed on similar systems. Using the NMR technique we were able to observe the transition from a supercooled A-like phase to a B-like phase on a 3 μm thick film. This is, to the best of our knowledge, the first observation of the A-B transition in a film under saturated vapour pressure.

Appendix A

Cryogenics and thermometry

Muchos años después, frente al pelotón de fusilamiento,
el coronel Aureliano Buendía había de recordar aquella
tarde remota en que su padre lo llevó a conocer el hielo.

Gabriel García Márquez. "Cien años de soledad"

^{3}He films need to be taken to temperatures well below 1 mK in order to observe superfluidity. This appendix describes the dilution refrigerator and the nuclear demagnetization stage with which those temperatures are achieved and the thermometers used to measure them.

A.1 The demagnetization cryostat

The ultra-low temperature apparatus used in these experiments consisted of an Oxford Instruments Kelvinox 400 dilution refrigerator with an attached nuclear demagnetization stage. The dilution unit was designed with the purpose of meeting

some custom requirements such as line of sight access ports and the incorporated demagnetization stage. We will provide here a brief description of all the parts involved in the cryogenic apparatus.

A.1.1 General overview of the cryogenic system

The cryostat hangs from a Dural table sat on four Newport I-2000 high performance laminar-flow air mounts. The air mounts are supported by several 30 cm thick sheets of wood which rest on concrete pillars. The purpose of the air mounts is to isolate the cryostat from potential vibrations which could induce eddy current heating by moving the nuclear stage with respect to the magnetic field. The vibration could also potentially affect the experimental results by making the ^{3}He films to move within the cells. Early measurements on the air mounts performance showed that the operation of the device reduced the magnitude of the vibrations, both horizontal and vertical, by a factor of 10 at the vibrational noise peaks. The highest transmissibility of the air mounts was found in the range 1-10 Hz. A more extensive study of these measurements and of the air mounts performance can be found elsewhere [100]. In order to further reduce the vibrations, the vacuum pumps are kept in a separate pump house outside the building and bolted to a large concrete block, isolated from the floor of the lab. Also, the pumping tubes are isolated using soft bellows sections.

The lower parts of the cryostat, where the lowest temperatures are achieved, are enclosed by a copper heat shield, which is bolted on to the continuous heat exchanger plate. In order to keep the nuclear stage still with respect to the heat shield, a small brass ring in contact with the nuclear stage is mechanically attached to a larger brass ring in contact with the shield by means of a network of cotton thread which does not provide any heat link. This device is called “spider”. Another

spider fixes the position of the heat shield with respect to the inner vacuum can, or IVC. The IVC, bolted to the 4 K flange and sealed with an indium o-ring, is made out of steel in its upper part. The lower part, inside the magnetic region, is made from brass. In order to keep the 4 K flange cold, a copper sheet about 40 cm long is rolled around the top section of the IVC. This helps to keep the 4 K flange at 4 K even when the bath level has decreased well bellow the top of the IVC. Covering the IVC there is a glass reinforced plastic sliding shield which allows the dewar to be lowered while still containing liquid helium. The vapour-shielded dewar is bolt to the refrigerator top plate and can be raised and lowered from a pit below the cryostat using a counter weight system. Inside the dewar are located the NMR and demagnetization magnets (see Section A.1.3). The insert top plate contains all the general refrigerator ports and services as well as various experimental and spare ports. Three of these ports, with a diameter of 40 cm, provide line of sight access down to the lower mixing chamber plate. One of them was used in this work for the DC SQUID amplifier used in the NMR experiment.

A.1.2 The dilution unit

As many other things, the possibility of achieving low temperatures by using a mixture of ^{3}He and ^{4}He was first suggested by Heinz London in 1951 at the Low Temperature Physics Conference held in Oxford. The first commercial ^{3}He-^{4}He dilution refrigerator was produced by Oxford Instruments in 1967. The physics and operation of the dilution unit has had an extensive treatment in the literature [101], [102], [103] and we will only give here a brief description. Figure A.1 shows a schematic of the dilution refrigerator with the nuclear stage incorporated. Below a ceratin critical temperature (0.87 K), the ^{3}He-^{4}He mixture separates into two phases:

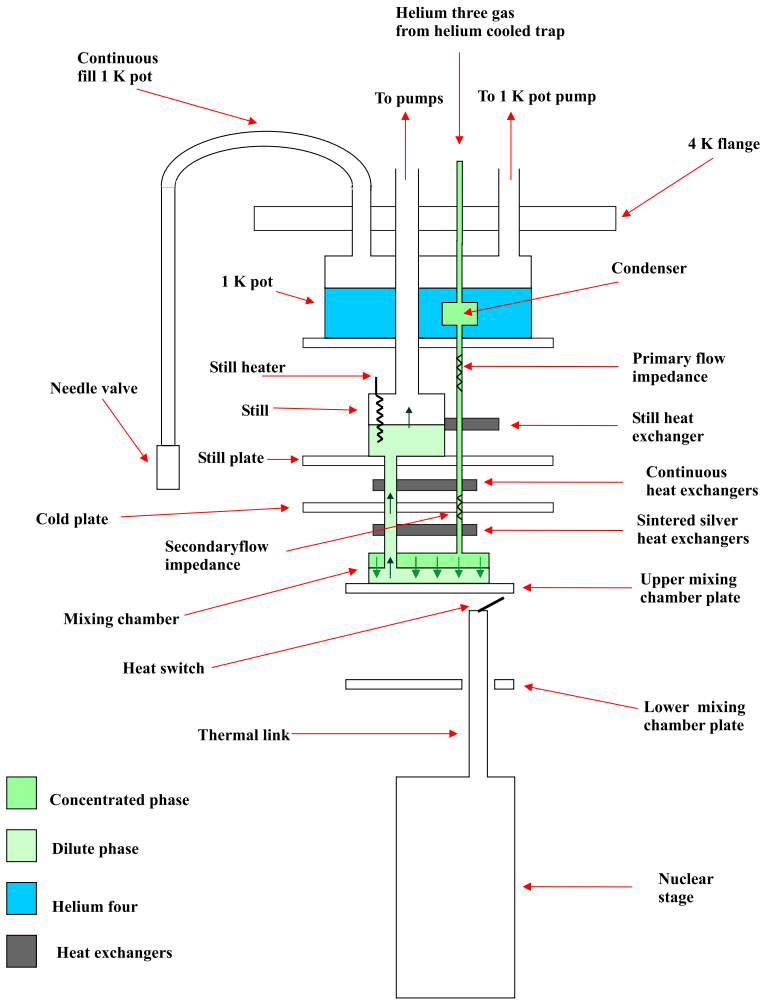

Figure A.1: Schematic of the dilution refrigerator (not to scale) showing the nuclear magnetisation stage.

a lighter "concentrated phase", rich in the isotope ^{3}He, and a heavier "dilute phase", rich in ^{4}He. A property of this mixtures is that the ^{3}He concentration in the dilute phase is finite even at absolute zero ($\sim 6.4\%$ at 0 K). The reason for this is that ^{3}He is lighter than ^{4}He and, therefore, has a higher zero-point energy. Consequently, a ^{3}He atom at zero temperature will find energetically more advantageous to be surrounded by ^{4}He atoms rather than ^{3}He atoms. The Pauli exclusion principle sets a limit for the number of ^{3}He atoms allowed in the dilute phase at each temperature (^{3}He is a

fermion). Of course, it will be also energetically advantageous for a ^{4}He atom to be surrounded by ^{4}He atoms for the same reasons. That makes the concentrated phase pure in ^{3}He at zero temperature.

Since the enthalpy of both phases is different, the expansion, or "evaporation" of ^{3}He into the dilute phase results in cooling. In other words, the concentrated phase acts as liquid ^{3}He whereas the dilute phase acts as ^{3}He gas. The ^{4}He background in the dilute phase acts as a high-quality vacuum. The theoretical cooling power is given by

$$\dot{Q} = 84\dot{n}_3 T_{\mathrm{mc}}^2$$

where $\dot{n}_3$ is the ^{3}He flow rate in moles per second and T_{mc} is the temperature of the mixing chamber.

The osmotic pressure between the still and the mixing chamber determines the concentration of ^{3}He in the still. This concentration is less than 1 % at the still operating temperature of 0.6 K. Between the mixing chamber and the still several heat exchangers transfer heat from the incoming concentrated phase into the dilute phase. When the refrigerator is first operated, the mixture is condensed by means of the 1 K pot, although phase boundary is not formed at that point, but at colder temperatures at the mixing chamber. As the mixture is circulated, the phase boundary descends to the mixing chamber, provided the concentration and the volume of the mixture is adequate. The unit will never achieve its base temperature if the phase boundary is located somewhere outside the mixing chamber. Thus is critical to preserve the balance of the mixture.

The primary flow impedance (see Figure A.1) is used to provide a high enough pressure for the incoming ^{3}He to condense at 1 K. The rest of the path down to the mixing chamber has to be designed such that a sufficiently high impedance remains

to compensate for the pressure drop in the liquid as the temperature decreases. Sometimes, a secondary flow impedance becomes necessary before the sintered silver heat exchangers.

The pumping system consists of two different pumps. The 1 K pot is pumped using a rotary pump (Leybold S25B) whereas the still is pumped on by a Leybold WSU 501 roots vacuum pump, backed by a helium sealed Leybold D65BH two stage rotary pump. Before entering the condenser, the returning ^{3}He goes through an oil mist filter, a liquid nitrogen cooled trap and a helium cooled trap. The 1 K pot is continuously filled from the bath through a needle valve which can be automatically adjusted.

The pumps and the circulation of the mixture are controlled by an Intelligent Gas Handling system (IGH), which is designed to automate many of the required operations using LabView software. Coupled to the IGH is the Intelligent Dilution Refrigerator Power Supply (IDR^{PS}) which monitors several temperature sensors on the refrigerator. The IDR^{PS} also controls the temperature of the exchange gas sorb and the heat supplied to the still and mixing chamber heaters. The temperature sensors at the cold plate, the still and the mixing chamber are monitored by a resistance bridge (AVS-47) and the information is continuously stored by the LabView software in the computer.

A.1.3 The magnet system

Two persistent superconducting magnets are located on their own support structure inside the dewar in the helium bath. The main magnet, capable of producing a magnetic field as high as 8 T, is used for nuclear demagnetization. This magnet is provided with cancellation coils to remove fringing fields from the centre of the

experimental region. The field/current ratio of the main magnet is specified by the manufacturer as 0.08104 T/A and the current decay in persistent mode is one part in 10^4 per hour. The main magnet has a bore diameter of 77 mm. The current is supplied by an Oxford Instruments Intelligent Superconducting Magnet power Supply, IPS^{1}20 − 10, which can provide up to 90 A.

The NMR magnet, used for providing the static field in the NMR experiment and the platinum NMR thermometer, can achieve fields of up to 3 T. The field/current ratio for this magnet is 0.08474 T/A and the field homogeneity is of $\sim$ 2 parts in 10^5 over a 15 mm diameter sphere. Its current decay in persistent mode is less than one part in 10^6 per hour. The bore diameter of this magnet is 103 mm. The NMR magnet obtains the electric current from a home-built 2 A protected current source.

A set of coils to provide magnetic field gradients is also located inside the dewar. They give 0.8 gauss/cm/A and were originally designed to improve the field homogeneity in the centre of the NMR magnet. This set of coils were used in the NMR experiment to image the experimental sample in the cell (see Chapter 3). Figure A.2 shows the magnetic field profile on the lower part of the cryostat. The stage plate and the lower mixing chamber plate are both in field cancellation regions.

A.1.4 The nuclear demagnetization stage

Adiabatic demagnetization of a paramagnet is the only known method of reaching temperatures lower than 1 mK. The idea of using nuclear magnetic moments for adiabatic demagnetization was first proposed by Gorter in 1934 [104] and the original experiments by Kurti in 1956 [105] reached temperatures of 20 μK. The nuclear magneton has a value of $\mu_{\rm n} = 5.1 \times 10^{-27}$ J/T as opposed to the Bohr magneton $\mu_{\rm B} = 9.3 \times 10^{-24}$ J/T. Therefore, the ordering temperature for nuclear moment is much

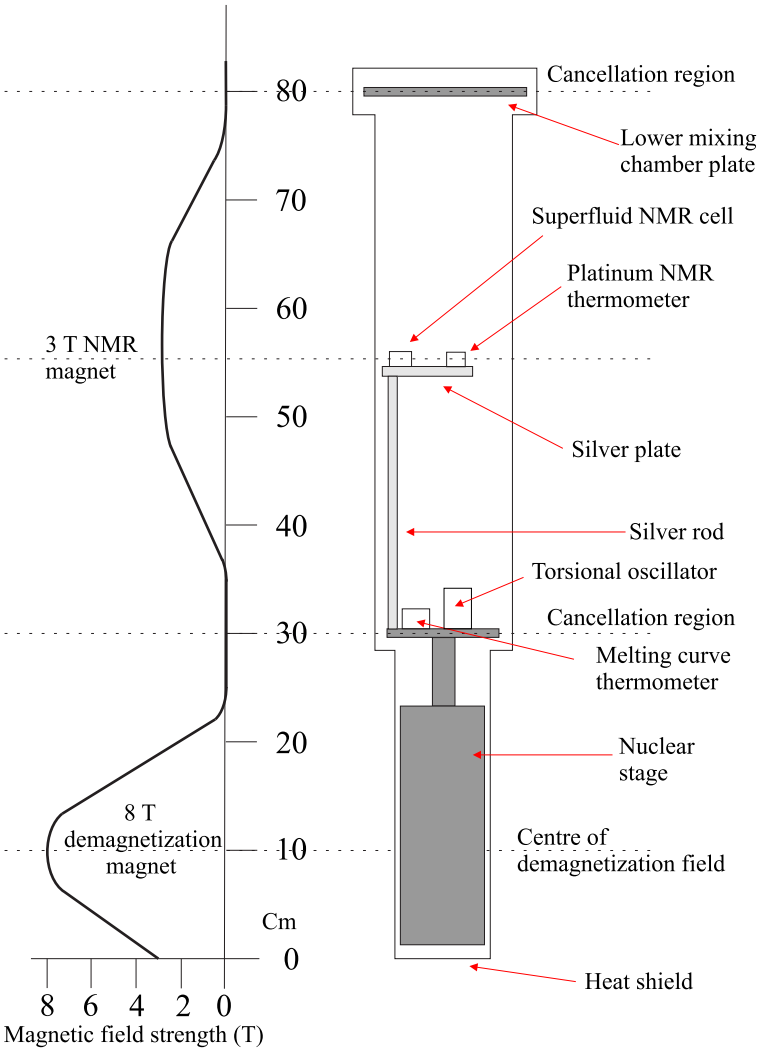

Figure A.2: The magnetic field profile of the nuclear stage and the experimental region. The position of the thermometers is shown as well as the position of the experimental cells. The field is cancelled at the lower mixing chamber plate and at the stage plate.

lower than that of electronic moments, making nuclear demagnetization much more convenient than electronic demagnetization for reaching ultra-low temperatures.

Our nuclear demagnetization stage, the thermal link and the heat switch were assembled by Dr. Nyéki and Dr. Dmitriev at the Kapitza Institute for Physical Problems in Moscow. The process used in its construction was similar in nature to

that described by Dmitriev [106]. The nuclear stage consists of several 1 mm thick copper sheets diffusion welded into a copper holder. It has a Residual Resistance Ratio (RRR) of ~ 400. The sheets help to reduce eddy current heating by providing more surface area and are separated by 50 μm thick teflon sheets and the whole bundle is held together rigidly with copper bolts inside teflon tubing. The dimensions of the stage, cylindrical in shape, are 54 mm in diameter and 280 mm in length. Applying different powers in a magnetic field and observing the subsequent warming up of the stage, the total number of copper moles can be calculated. This number was found to be [51], in the maximum field of the main magnet, 42.2 moles.

The nuclear stage is thermally connected to the mixing chamber through a thermal link and a superconducting heat switch. The thermal link is made from seven 0.5 mm thick 5N purity annealed copper strips which are diffusion welded at both ends into a copper comb shaped clamp terminating in a cone joint. It has a total length of 660 mm and a RRR of ~ 1400. The upper end of the thermal link is connected to the heat switch plate, a 1 cm thick copper plate, which, in turn, is connected to the mixing chamber plate through an aluminium superconducting heat switch. This heat switch is made from five 0.32 mm thick, 5 cm long, 5N purity aluminium strips. Both ends of the heat switch are diffusion welded into copper rods, of which one is attached to the heat switch plate and the other to the mixing chamber plate. To operate the switch, a magnetic field is produced in a superconducting solenoid made out of multi-filamentary NbTi wire in a CuNi matrix. The required field is of 10 mT. Before, during and after ramping up the main magnetic field prior to a demagnetization process, the heat switch is in its normal state (closed) thus allowing the refrigerator to take up the heat resulting from the ramp up and thermally connecting the mixing chamber and the nuclear stage during the precooling. Typical precooling periods are of about 60 hours, after which the temperature of the nuclear

stage is, generally, $\sim$ 12 mK in 7.29 T. The heat switch is opened at this point by removing the 10 mT field, leaving the nuclear stage thermally isolated from the rest of the refrigerator. The main field is then reduced adiabatically in steps. The final temperature follows the expression

$$\frac{B_{\mathrm{i}}}{T_{\mathrm{i}}} = \frac{B_{\mathrm{f}}}{T_{\mathrm{f}}}$$

where the subindexes i and f refer to initial and final states, respectively.

A.2 Thermometry

The temperatures at different points of the refrigerator are measured with several types of thermometers. The 4 K flange, the 1 K pot, the cold plate, the still and the mixing chamber, all have carbon resistance thermometers. A melting curve thermometer (MCT) is situated in the nuclear stage and a platinum NMR thermometer is mounted on the silver experimental plate. These two later thermometers are used in the data acquisition and we will briefly describe them here.

A.2.1 The melting curve thermometer

A melting curve thermometer measures the pressure of a ^{3}He sample which is in its liquid-solid coexistence curve. Since this curve is experimentally known, the temperature can be extracted from the pressure measurement. This kind of thermometer is useful down to about 1 mK. Below that temperature the pressure flattens out and higher pressure sensitivity would be required. The MCT cell constitutes a pressure transducer where the pressure is obtained by measuring a capacitance . The distance between the capacitor plates is decreased when the ^{3}He pressure increases.

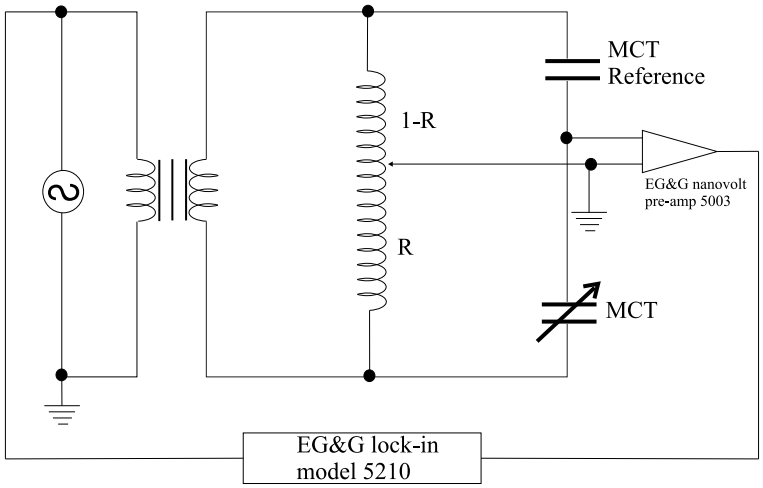

Figure A.3: The capacitance bridge used to measure the MCT capacitance.

The capacitance is measured using a standard capacitance bridge, as shown in Figure A.3. The reference capacitor is located at the 1 K plate. This set up gives us a pressure resolution better than 10 μbar at 35 bar. This corresponds to a temperature resolution of 0.25 μK. Our MCT, on loan from PTB, is mounted in a cone joint on the nuclear stage. Since the ^{3}He melting curve is sensitive to magnetic field, the MCT cell has to be located in a field cancellation region, as shown in Figure A.2. The method for calibrating the pressure versus capacitance is the same as the one described in Richardson and Smith [107]. This pressure calibration is carried out at above 1 K using a Paroscientific Digiquartz gauge. Prior to the calibration the diaphragm is exercised at 1 K in order to reduce hysteresis. The ^{3}He A-transition is then measured and the entire pressure range shifted so the measurement corresponds with that given by the Provisional Low Temperature Scale, 0.9 to 1 K: PLTS-2000. We found, after this procedure, that the pressure at which the solid ordering transition occurred agreed with the PLTS-2000 scale to within 0.5 mbar.

A second MCT, obtained from Sussex, was mounted on to the mixing chamber plate. This MCT was, however, never used in the experiments reported in this work.

A.2.2 The platinum NMR thermometer

Platinum follows Curie's Law (Equation 3.3) down to the lowest temperatures we can achieve with our cryostat and hence the platinum NMR thermometer was used as our main thermometer for the sub-millikelvin range of temperatures. It consists of a bundle of approximately 2000 25 μm thick platinum wires welded to a thick silver wire. The silver wire is clamped to a silver post which is thermally connected to the nuclear stage. The platinum thermometer is placed in the experimental region of the refrigerator, just at the centre of the NMR magnet (see Figure A.2). A Kapton former sliding over the platinum bundle provides support for a copper coil which acts as both, transmitter and receiver. This copper coil consists of about 5000 turns of 25 μm thick copper wire. A PLM-4 pulsed NMR system [108] operated at 263 kHz was used to measure the platinum susceptibility

The thermometer was calibrated against the MCT at several temperatures between 50 mK and 1 mK and then extrapolated to the lowest temperatures according to Curie's Law. Each temperature was stabilized using a PID temperature controller. The applied pulse size depended on the working range of temperatures, the 90^{o} pulse being applied only at the higher temperatures to avoid saturation of the amplifiers. At the lowest temperatures, the pulse size was reduced by a factor of 16 and we used a couple of more pulse sizes in between in order to cross-calibrate the small pulse against the large pulse. Also, at these low temperatures the signal to noise ratio was large enough that a single shot was used to measure the magnetic susceptibility. Pulses were applied every 5 minutes in order to allow the spins to recover ($T_1 \sim 300$ for platinum).

Figure A.4 shows the temperature of the stage as measured by the PLM thermometer during a typical cooling as a function of the magnetic field. It can be

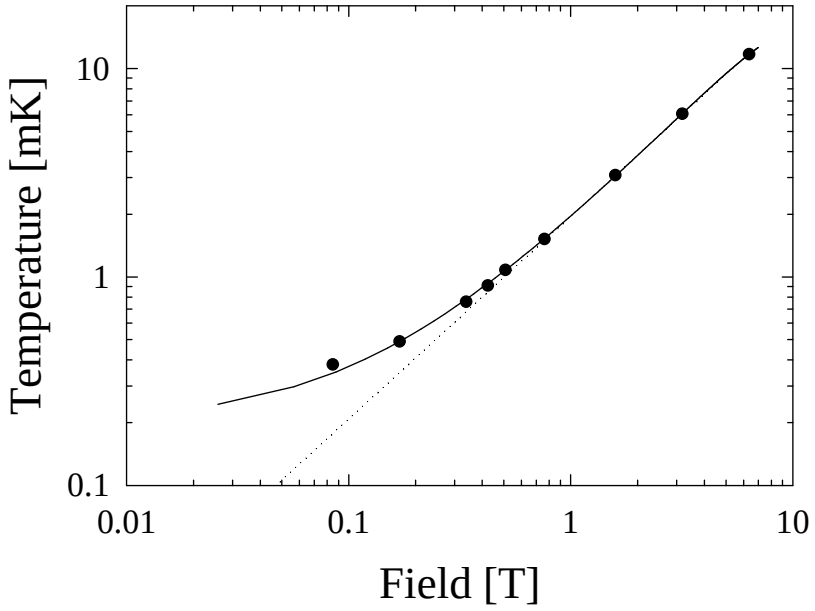

Figure A.4: The temperature of the nuclear stage as a function of the magnetic field.

seen that the demagnetization is adiabatic down to about 0.8 mK. At lower temperatures, the thermal time constant of the PLM thermometer is increased by the parasitic nuclear heat capacity of the silver rod which provides the thermal contact between the thermometer and the stage.

Appendix B

Data analysis techniques

If we knew what it was we were doing,

it would not be called research, would it?

Albert Einstein.

B.1 Digital Fourier transform in the NMR experiment

In the NMR experiment the data are obtained in the time domain. In order to obtain a NMR signal in the frequency domain it is needed to perform a Fourier transform of the original data. Since computers can only work with information that is both *discrete* and *finite* in time, we need to use the digital Fourier transform (DFT) analysis.

For a signal $f(t)$ defined over a continuous and infinite time domain, the Fourier

transform is given by

$$\mathcal{F}[f(t)](\omega) = \int_{-\infty}^{\infty} f(t)e^{-j\omega t}dt$$

When the time variable is discrete and $f(t)$ is sampled N times with a sampling interval of Δ the Fourier transform can be expressed as

$$\mathcal{F}(\omega_n) \approx \Delta \sum_{k=0}^{N-1} f_k e^{-j\omega_n t_k} \tag{B.1}$$

where $f_k = f(t_k)$ with $k = 0, 1...N-1$ and $\omega_n = 2\pi n/N\Delta$ with $n = -N/2...N/2$. According to the *Nyquist Sampling Theorem*, in order to avoid aliasing occurring in the sampling of a signal the sampling rate, $1/\Delta$, should be greater than or equal to twice the highest frequency present in the signal. Therefore, the components of the time-domain signal with frequencies higher than the critical frequency (also called Nyquist frequency) $f_c = 1/2\Delta$ will be aliased to lower frequencies. Aliasing can be avoided by using a low-pass filter which effectively cuts off frequencies higher than about half the Nyquist frequency. This means that some prior knowledge of the nature of the spectrum is often required before the exact sampling rate is determined. The filter must be employed *before* the signal is digitized, for the aliasing effects occur because of the sampling process.

We can now apply the DFT treatment to a free induction decay signal. This signal is given by

$$f(t) = \begin{cases} 0 & \text{for } t < 0, \\ Ae^{-t/T_2^*}\sin(\omega_o t + \delta) & \text{for } t \geq 0 \end{cases}$$

and its Fourier transform is

$$\mathcal{F}(\omega) = \int_0^\infty A e^{-t/T_2^*} \sin(\omega_\mathrm{o} t + \delta) e^{-j\omega t} dt =$$
$$= \frac{A}{2j} \int_0^\infty e^{-t/T_2^*} \left[e^{-j(\omega-\omega_\mathrm{o})t-\delta} - e^{-j(\omega+\omega_\mathrm{o})t+\delta} \right] dt$$

Integrating, we obtain

$$\mathcal{F}(\omega) = \frac{A}{2j} \left[\frac{T_2^* e^{-j\delta}}{1 - jT_2^*(\omega - \omega_\mathrm{o})} - \frac{T_2^* e^{j\delta}}{1 - jT_2^*(\omega + \omega_\mathrm{o})} \right]$$

The resonance peak at ω_o is the one we are interested in. The amplitude of that complex number gives us the magnitude of the peak

$$\mid \mathcal{F}(\omega) \mid = \frac{A}{2} \left[\frac{(T_2^*)^2}{1 + (T_2^*(\omega - \omega_\mathrm{o})^2)} \right]^{1/2}$$

At the resonance peak, this magnitude is simply

$$\mid \mathcal{F}(\omega) \mid_\mathrm{p} = \frac{AT_2^*}{2}$$

Since the LabVIEW routine returns $|\mathcal{F}_\mathrm{n}| = |\mathcal{F}(\omega_\mathrm{n})|/\Delta$ after the DFT, the obtained magnitude of the peak is

$$S_\mathrm{p} = \frac{AT_2^*}{2\Delta}$$

Along with the Free Induction Decay, the measured signal contains a certain level of noise, which is also affected by the Fourier transform routine. Let us consider a noise power $< P_\mathrm{N} > (t)$ per unit bandwidth in the time domain arising for the noise signal $n(t)$. We can then make use of the Parseval's theorem, which states that the

power computed in either domain equals the power in the other

$$\int_{-\infty}^{\infty} n^2(t)dt = \int_{-\infty}^{\infty} (|\mathcal{N}(\omega)|)^2 d\omega$$

where $\mathcal{N}(\omega)$ is the Fourier transform of $n(t)$. For white noise, this theorem gives

$$|\mathcal{N}|^2 = N|n_k|^2 = \frac{T_{\rm capture} B < N >}{\Delta}$$

where $|n_k|^2 = B < P_{\rm N} >$ is the noise level sampled at intervals of Δ and B is the bandwidth of the working time interval. Therefore, we conclude that the rms noise level is

$$(\mathcal{N})_{\rm rms} = \sqrt{\frac{T_{\rm capture}}{\Delta}} B^{1/2} < P_{\rm N} >^{1/2}$$

and, choosing the bandwidth to be equal to the Nyquist frequency, $B = 1/2\Delta$,

$$(\mathcal{N})_{\rm rms} = \frac{1}{\Delta}\sqrt{\frac{T_{\rm capture}}{2}} < P_{\rm N} >^{1/2}$$

Of course, this result is also valid for frequency-dependent noise, since the functional dependence is the same after the Fourier transform. Finally, in order to compare the measured noise level at the peak to the magnitude of the signal at the peak we have to include the ratio of peak noise to rms noise, $K_{\rm N}^{\rm f}$, obtaining the final expression for the noise level at the peak

$$N_{\rm P} = K_{\rm N}^{\rm f}(\mathcal{N})_{\rm rms} = \frac{K_{\rm N}^{\rm f}}{\Delta}\sqrt{\frac{T_{\rm capture}}{2}} < P_{\rm N} >^{1/2}$$

B.2 Inferred resonance frequency and dissipation in the torsional oscillator experiment

At a fixed temperature, one could measure the resonance frequency and the dissipation of the torsional oscillator by doing a frequency sweep and obtaining the resonance curve, i.e. the energy developed in the oscillator by the driving force versus frequency. That curve would be centered at the resonance frequency and its width at half height would be related to the dissipation by $1/Q = \gamma/\omega_o$, where $1/Q$ is the dissipation, ω_o is the resonance frequency and γ is the peak width at half height.

In a practical experiment, however, the temperature is usually not fixed and that kind of measurement is not feasible, since the resonance frequency and dissipation are temperature dependent. Instead, the in-phase and quadrature components of the output signal are continuously monitored and used to infer the parameters of physical interest.

Considering the one-dimensional forced and damped harmonic oscillator, the real (quadrature) and imaginary (in-phase) parts of the steady-state solution are respectively given by

$$Y(\omega) = \frac{\hat{F}(\omega_o^2 - \omega^2)}{m[(\omega_o^2 - \omega^2)^2 + \gamma^2\omega^2]}$$

$$X(\omega) = \frac{\hat{F}\gamma\omega}{m[(\omega_o^2 - \omega^2)^2 + \gamma^2\omega^2]}$$

where $\hat{F}$ is the (complex) amplitude of the driving force. We can now obtain an expression for the resonance frequency by simply dividing one part of the solution by the other, which gives

$$\frac{Y(\omega)}{X(\omega)} = \frac{Q(\omega_o^2 - \omega^2)}{\omega_o\omega}$$

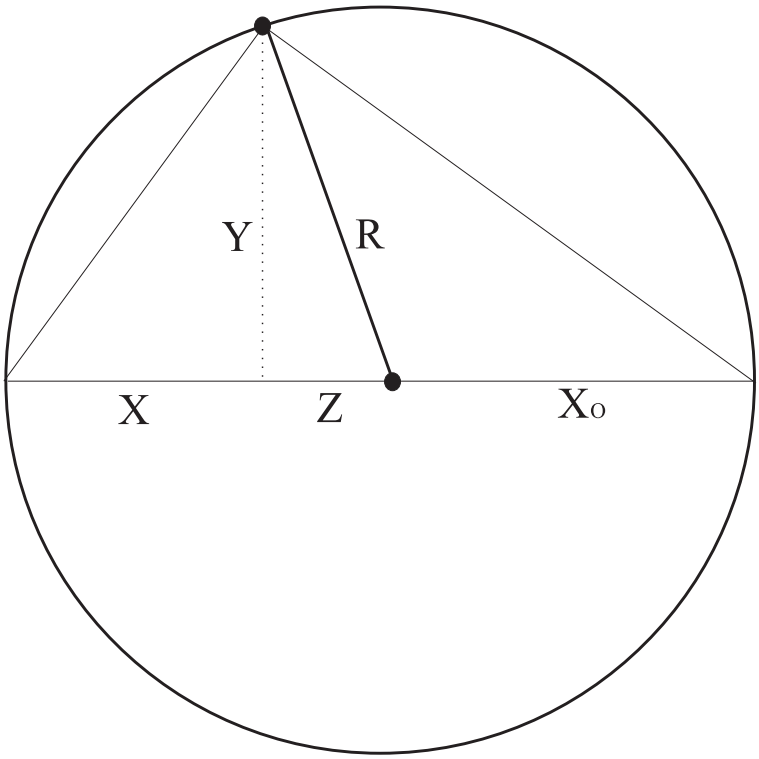

Figure B.1: The Nyquist circle used to obtain an expression relating $Q(T)$ with $X(T)$ and $Y(T)$.

using the definition $\gamma = \omega_o/Q$. This equation has the following solution for ω_o

$$\omega_o = \frac{\omega Y(\omega)}{2QX(\omega)} + \omega\sqrt{1 + \frac{Y^2(\omega)}{4Q^2X^2(\omega)}}$$

Near resonance, $Y^2/X^2 \ll 1$ and the square root can be approximated by $(1 + Y^2/8Q^2X^2)$, giving the (temperature-dependent) inferred frequency

$$\omega_o(T) = \omega(1 + \frac{Y(T)}{2QX(T)} + \frac{Y^2(T)}{8Q^2Y^2(T)}) \approx \omega(1 + \frac{Y(T)}{2QX(T)})$$

for a driving frequency ω.

The Q factor can be obtained in a similar way. At resonance, the amplitude of

the movement is given by just the in-phase component of the solution

$$A(\omega_o) = \sqrt{Y^2(\omega_o) + X^2(\omega_o)} = X(\omega_o) = X_o$$

and, therefore, Q/X_o is temperature independent. We can relate X_o to the measured X and Y values by considering the Nyquist circle showed in Figure B.1. The circle is centered at $X_o/2$ and has a diameter of X_o. For a given point (X, Y) in the circle, $Z^2 + Y^2 = R^2$ with $Z = R - X$. Therefore, $R = (X^2 + Y^2)/2X$ and hence

$$X_o = \frac{X^2 + Y^2}{X}$$

If we measure Q and X_o at some fixed temperature T_o and define $K(T_o) = Q(T_o)/X_o(T_o)$ we finally have

$$Q(T) = K(T_o)X_o(T) = K(T_o)\frac{X^2(T) + Y^2(T)}{2X(T)}$$

and a value of Q can be obtained at any temperature by measuring the in-phase and quadrature components of the oscillator's response at that temperature.

Bibliography

[1] J. Bardeen, L. N. Cooper, and J. R. Schrieffer. Theory of Superconductivity. *Phys. Rev.*, 108:1175–1204, 1957.

[2] L. P. Pitaevskii. Superfluidity of helium-3. *Sov. Phys.- JETP*, 10:1267, 1960.

[3] V. P. Peshkov. Properties of helium-3 and its solutions in helium-4. *Zh. Eksp. Teor. Fiz.*, 46:1510, 1964.

[4] D. D. Osheroff, W. J. Gully, R. C. Richardson, and D. M. Lee. New magnetic phenomena in liquid ^{3}He below 3 mk. *Phys. Rev. Lett.*, 29:920, 1972.

[5] V. Ambegaokar, P. G. deGennes, and D. Rainer. Landau-ginzburg equations for an anisotropic superfluid. *Phys. Rev. A*, 9:2676–2685, 1974.

[6] J. M. Kosterlitz and D. J. Thouless. Long range order and metastability in two dimensional solids and superfluids. *J. Phys. C.*, 5:124–126, 1972.

[7] J. Corson, R. Mallozzi, J. Orenstein, J. N. Eckstein, and I. Bozovic. Vanishing of phase coherence in underdoped $Bi_2Sr_2CaCu_2O_{8+\delta}$. *Nature*, 398(6724):221–223, 1999.

[8] A. Hosseini, D. M. Broun, D. E. Sheehy, T. P. Davis, M. Franz, W. N. Hardy, R. Liang, and D. A. Bonn. Survival of the d-wave superconducting state near

the edge of antiferromagnetism in the cuprate phase diagram. *Phys. Rev. Lett.*, 93:107003, 2004.

[9] J. V. Porto and J. M. Parpia. Superfluid ^{3}He in aerogel. *Phys. Rev. Lett.*, 74(23):4667–4670, 1995.

[10] T. A. Jacobson and G. E. Volovik. Event horizons and ergoregions in ^{3}He. *Phys. Rev. D*, 58:064021, 1998.

[11] T. A. Jacobson and G. E. Volovik. Effective spacetime and Hawking radiation from moving domain wall in thin film of ^{3}He-A. *Pisma Zh. Eksp. Teor. Fiz.*, 68:833–838, 1998.

[12] T. Jacobson and T. Koike. *Black hole and baby universe in a thin film of ^{3}He-A*. World Scientific, 2002. Chapter for book "Artificial black holes".

[13] R. Balian and N. R. Werthamer. Superconductivity with pairs in a relative p wave. *Phys. Rev.*, 131(4):1553–1564, 1963.

[14] P. W. Anderson and W. F. Brinkman. Anisotropic superfluidity in ^{3}He: a possible interpretation of its stability as a spin-fluctuation effect. *Phys. Rev. Lett.*, 30(22):1108–1111, 1973.

[15] P. W. Anderson and P. Morel. Generalized Bardeen-Cooper-Schrieffer states and the proposed low-temperature phase of liquid ^{3}He. *Phys. Rev.*, 131(6):1911–1934, 1961.

[16] T. J. Greytak, R. T. Johnson, D. N. Paulson, and J. C. Wheatley. Heat flow in the extraordinary phases of liquid ^{3}He. *Phys. Rev. Lett.*, 31:452–455, 1973.

[17] A. I. Ahonen, M. T. Haikala, M. Krusius, and O. V. Lounasmaa. Phase diagram of liquid ^{3}He between 0.7 and 2.5 mK. *Phys. Rev. Lett.*, 33:628–631, 1974.

[18] L. D. Landau. The theory of the Fermi liquid. *Zh. Eksp. Teor. Fiz.*, 30:1058, 1956.

[19] L. D. Landau. *Collected papers of L. D. Landau.* Pergamon, Oxford, 1965, Pg. 193.

[20] A. J. Leggett. A theoretical description of the new phases of liquid ^{3}He. *Rev. Mod. Phys.*, 47(2):331–414, 1975.

[21] K. H. Bennemann and J. B. Ketterson. *The physics of liquid and solid Helium, part II.* Wiley, New York, 1978, Pg. 287.

[22] N. D. Mermin and C. Stare. Ginzburg-Landau approach to L $\neq$ 0 pairing. *Phys. Rev. Lett.*, 30:1135–1138, 1973.

[23] G. Barton and M. A. Moore. *Journal of Low Temperature Physics*, 21:489, 1975.

[24] D. M. Lee. The extraordinary phases of liquid ^{3}He. *Rev. Mod. Phys.*, 69(3):645–665, 1997.

[25] L. H. Kjäldman, J. Kurkijärvi, and D. Rainer. Suppression of p-wave superfluidity in long, narrow pores. *Journal of Low Temperature Physics*, 33(5/6):577–586, 1978.

[26] A. L. Fetter and S. Ullah. Superfluid density and critical current of ^{3}He in confined geometries. *Journal of Low Temperature Physics*, 70:515, 1988.

[27] Y. H. Li and T. L. Ho. Superfluid ^{3}He in very confined regular geometries. *Phys. Rev. B*, 38(4):2362–2370, 1988.

[28] A. B. Vorontsov and J. A. Sauls. Thermodynamic properties of thin films of superfluid ^{3}He-A. *Phys. Rev. B.*, 68:064508, 2003.

[29] M. Yamamoto, S. Higashitani, Y. Nagato, and K. Nagai. Superfluid density in ^{3}He film. *Physica B*, 284-288:271–272, 2000.

[30] A. M. R. Schechter, R. W. Simmonds, R. E. Packard, and J. C. Davis. Observation of third sound in superfluid ^{3}He. *Nature*, 396:554–556, 1998.

[31] D. L. Stein and M. C. Cross. Phase transitions in two-dimensional superfluid ^{3}He. *Phys. Rev. Lett.*, 42(8):504–507, 1979.

[32] H. Kawamura. Successive transitions and intermediate chiral phase in a superfluid ^{3}He film. *Phys. Rev. Lett.*, 82:964–967, 1999.

[33] V. Kotsubo, K. D. Hahn, and J. M. Parpia. Supperssion of superfluidity of ^{3}He in cylindrical channels. *Phys. Rev. Lett.*, 58:804–807, 1987.

[34] M. T. Manninen and J. P. Pekola. Flow of ^{3}He-B through narrow channels. *Phys. Rev. Lett.*, 48:1369, 1982.

[35] Z. Tešanović and O. T. Valls. Quantum size effects in superfluid ^{3}He films. *Phys. Rev. B*, 33(5):3139–3145, 1986.

[36] Z. Tešanović. The orientational effects in the two-dimensional superfluid ^{3}He. *Phys. Lett.*, 100A(3):158–160, 1984.

[37] Z. Tešanović and O. T. Valls. Nuclear magnetic resonance in two-dimensional superfluid ^{3}He. *Phys. Rev. B*, 31(3):1374–1387, 1985.

[38] A. Sachrajda, R. F. Harris-Lowe, J. P. Harrison, R. R. Turkington, and J. G. Daunt. ^{3}He film flow: two-dimensional superfluidity. *Phys. Rev. Lett.*, 55(15):1023, 1985.

[39] S. C. Steel, J. P. Harrison, P. Zawadzki, and A. Sachrajda. ^{3}He film flow on a round rim beaker. *Journal of Low Temperature Physics*, 95:759–787, 1994.

[40] J. G. Daunt, R. F. Harris-Lowe, J. P. Harrison, A. Sachrajda, S. Steel, R. R. Turkington, and P. S. Zawadski. Critical temperature and critical current of thin-film superfluid ^{3}He. *Journal of Low Temperature Physics*, 70(5/6):547–568, 1988.

[41] J. C. Davis, A. Amar, J. P. Pekola, and R. E. Packard. Superfluidity of ^{3}He films. *Phys. Rev. Lett.*, 60(4):302–304, 1988.

[42] M. R. Freeman and R. C. Richardson. Size effects in superfluid ^{3}He films. *Phys. Rev. B*, 41(16):11011–11028, 1990.

[43] J. Xu and B. C. Crooker. Very thin films of ^{3}He: a new phase? *Phys. Rev. Lett.*, 65(24):3005–3008, 1990.

[44] A. M. R. Schechter. *Third sound in superfluid ^{3}He.* PhD thesis, University of California at Berkeley, 1999. Unpublished.

[45] T. Kawae, M. Kubota, Y. Ishimoto, S. Miyawaki, O. Ishikawa, T. Hata, and T. Kodama. A-B transition of superfluid ^{3}He with a film geometry. *Journal of Low Temperature Physics*, 3(5/6):917–935, 1998.

[46] K. Kawasaki, Y. Tomohiro, M. Tarui, H. Nakagawa, H. Yano, O. Ishikawa, and T. Hata. Phase-transition phenomena of 0.8 μm superfluid ^{3}He slab. *Phys. Rev. Lett.*, 93(10):105301, 2004.

[47] Miyawaki, K. S. Kawasaki, H. Inaba, A. Matsubara, O. Ishikawa, T. Hata, and T. Kodama. Pressure dependence of the A-B phase transition temperature in superfluid ^{3}He in 1.1 μm slab geometry. *Phys. Rev. B.*, 62(9):5855–5863, 2000.

[48] A. Abragam. *The principles of nuclear magnetism.* Oxford University Press, 1961.

[49] E. R. Andrew. *Nuclear magnetic resonance.* Cambridge University Press, 1955.

[50] B. P. Cowan. *Nuclear magnetic resonance and relaxation.* Cambridge University Press, 1997.

[51] H. J. Dyball. *A study of ^{3}He films using SQUID NMR.* PhD thesis, Royal Holloway University of London, 2001. Unpublished.

[52] C. P. Lusher, J. Li, M. E. Digby, R. P. Reed, B. Cowan, J. Saunders, D. Drung, and T. Schurig. Broadband nuclear magnetic resonance using DC SQUID amplifiers. *Applied Superconductivity*, 6(10-12):591, 1998.

[53] D. Drung. DC SQUID systems overview. *Supercond. Sci. Technol.*, 4:377–385, 1991.

[54] D. Drung. Advanced SQUID read-out electronics. *SQUID Sensors: Fundamentals, Fabrication and Applications*, 1996.

[55] D. I. Hoult and R. E. Richards. The signal to noise ratio of the nuclear magnetic resonance experiment. *J. Magn. Resonance*, 24:71, 1976.

[56] D. Drung, H. Matz, and H. Koch. A 5-MHz bandwidth SQUID magnetometer with additional positive feedback. *Rev. Sci. Instrum.*, 67:3008, 1995.

[57] R. Stoll. *The analysis of Eddy Currents*. Clarendon Press, Oxford, 1974.

[58] E. Fukushima and S. B. W. Roeder. *Experimental Pulse NMR: A Nuts and Bolts Approach*. Addison-wesley, 1981.

[59] E. Cheng and M. W. Cole. Retardation and many-body effects in multilayer-film adsorption. *Phys. Rev. B*, 38:987–995, 1988.

[60] D. D. Osheroff and L. R. Corruccini. Pulsed NMR frequency shifts in ^{3}He-B. *Proceedings of the 14th International Conference on Low Temperature Physics*, 1:100, 1975.

[61] W. F. Brinkman and H. Smith. Frequency shifts in pulsed NMR for the A- and B-phases of superfluid ^{3}He. *Proceedings of the 14th International Conference on Low Temperature Physics*, 1:45, 1975.

[62] P. Schiffer, M. T. O'Keefe, M. D. Hildreth, H. Fukuyama, and D. D. Osheroff. Strong supercooling and stimulation of the A-B transition in superfluid ^{3}He. *Phys. Rev. Lett.*, 69:120–123, 1992.

[63] P. Schiffer, D. D. Osheroff, and A. J. Leggett. *Progress in Low Temperature Physics*. Elsevier Science, 1995. Chapter 3: Nucleation of the AB transition in superfluid ^{3}He: experimental and theoretical considerations, Pg. 159-211.

[64] P. J. Hakonen, K. K. Nummila, J. T. Simola, L. Skrbek, and G. Mamniashvili. Surface spin waves in ^{3}He-A, a probe for vortex phenomena in narrow gaps. *Phys, Rev. Lett.*, 58(7):678–681, 1987.

[65] K. Maki and P. Jumar. Planar l textures and magnetic resonances in superfluid ^{3}He-A. *Phys. Rev. B*, 16:174, 1977.

[66] A. J. Leggett and S. K. Yip. *Superfluid ^{3}He.* North Holland, 1989.

[67] A. J. Leggett. Nucleation of ^{3}He-B from the A phase: A cosmic-ray effect? *Phys. Rev. Lett.*, 53:1096–1099, 1984.

[68] D. S. Buchanan, G. W. Swift, and J. C. Wheatley. Velocity of propagation of the ^{3}He A-B interface in hypercooled ^{3}He-A. *Phys. Rev. Lett.*, 57:341–344, 1986.

[69] S. T. P. Body and G. W. Swift. *Journal of Low Temperature Physics*, 87:35, 1992.

[70] A. J. Leggett. Interpretation of recent results on ^{3}He below 3 mk: a new liquid phase? *Phys. Rev. Lett.*, 29:1227, 1972.

[71] P. Schiffer, M. T. O'Keefe, H. Fukuyama, and D. D. Osheroff. Low-temperature studies of the NMR frequency shift in superfluid ^{3}He-A. *Phys. Rev. Lett.*, 69(21):3096–3099, 1992.

[72] R. F. Berg, B. N. Engel, and G. G. Ihas. NMR in bulk ^{3}He-A: pressure dependence and thermometry. *Proceedings of the 17th International Conference on Low Temperature Physics*, page 1171, 1984.

[73] R. A. Webb, R. E. Sager, and J. C. Wheatley. Relationship between the linear ringing frequencies in ^{3}He-A and ^{3}He-B near the polycritical point. *Phys. Rev. Lett.*, 35:615, 1975.

[74] D. D. Osheroff and P. W. Anderson. Nuclear magnetic resonance of superfluid ^{3}He near T_c in high magnetic fields. *Phys. Rev. Lett.*, 33:686, 1974.

[75] A. I. Ahonen, M. Krusius, and M. A. Paalanen. NMR experiments on the superfluid phases of ^{3}He in restricted geometries. *Journal of Low Temperature Physics*, 25:421, 1976.

[76] E. L. Andronikashvili. Direct observation of two types of motion in Helium II. *Zhur. Ekxp. Theor. Fiz.*, 16:780–785, 1946.

[77] J. C. Long, H. W. Chan, A. B. Churnside, E. A. Gulbis, M. C. M. Varney, and J. C. Price. Upper limits to submillimetre-range forces from extra space-time dimensions. *Nature*, 421:922, 2003.

[78] E. Kim and M. H. W. Chan. Probable observation of a supersolid helium phase. *Nature*, 427:225, 2004.

[79] G. W. Morley, A. Casey, C. P. Lusher, B. Cowan, J. Saunders, and J. M. Parpia. Torsion pendulum for the study of thin ^{3}He films. *Journal of Low Temperature Physics*, 126(1-2):557–562, 2002.

[80] A. Casey, J. Papia, R. Schanen, B. Cowan, and J. Saunders. Interfacial friction of thin ^{3}He slabs in the knudsen limit. *Phys. Rev. Let.*, 92(25):255301–1,255301–4, 2004.

[81] J. V. Porto and J. M. Parpia. Diffusion welds between copper and silver alloys. *Physica B*, 194-196:857, 1994.

[82] L. D. Landau and E. M. Lifshitz. *Course of Theoretical Physics*, volume 6. 1959.

[83] E. Cheng and M. W. Cole. Physical adsorption near an oblique corner. *Phys. Rev. B*, 41(14):9650–9653, 1990.

[84] L. D. Landau. On the theory of superfluidity of Helium II. *J. Phys.*, 5:71, 1941.

[85] L. Tisza. The theory of liquid helium. *Phys. Rev.*, 72:838–854, 1947.

[86] D. Sawkey and J. P. Harrison. Volume flow in liquid He-3 in the Knudsen and Poiseuille regions. *Physica (Amsterdam)*, 329B-333B:133, 2003.

[87] Roger M. Bowley. Private communication.

[88] D. T. Lawson, W. J. Gully, S. Goldstein, R. C. Richardson, and D. M. Lee. Attenuation of zero sound and the low-temperature transitions in liquid ^{3}He. *Phys. Rev. Lett.*, 30:541–544, 1973.

[89] I. M. Khalatnikov. *An introduction to the theory of superfluidity*, volume 1. Benjamin, New York, 1965. Chapter 1.

[90] K. R. Atkins. Third and fourth sound in liquid Helium II. *Phys. Rev.*, 113:962–965, 1959.

[91] K. A. Shapiro and I. Rudnick. Fourth sound in He II. *Phys. Rev. Lett.*, 9:191–193, 1962.

[92] M. R. Freeman. *Size effects in ^{3}He films.* PhD thesis, Cornell University, 1988. Unpublished.

[93] J. M. Parpia, D. G. Wildes, J. Saunders, E. K. Zeise, J. D. Reppy, and R. C. Richardson. The temperature and pressure dependence of the normal fraction of superfluid ^{3}He-B. *Journal of Low Temperature Physics*, 61(5/6):337–361, 1985.

[94] K. W. Jacobsen and H. Smith. Critical current for the flow of superfluid ^{3}He in a confined geometry. *Journal of Low Temperature Physics*, 67:83, 1987.

[95] T. Fujita, M. Nakahara, T. Ohmi, and T. Tsuneto. A-B transition in superfluid ^{3}He film. *Prog. Theor. Phys.*, 64:396, 1980.

[96] L. V. Kiknadze and Y. G. Mamaladze. Thermodynamic stability of a helium II film and dependence of mean density of a superfluid component on temperature and film thickness. *Fiz. Nizk.Temp.*, 1:219, 1975.

[97] J. Xu. *Superfluidity in thin ^{3}He films*. PhD thesis, Purdue University, 1991. Unpublished.

[98] G. Lawes and M. Parpia. Estimate of the gap parameter for superfluid ^{3}He in aerogel. *Phys. Rev. B*, 65:0925111–4, 2002.

[99] K. Matsumoto, J. V. Porto, L. Pollack, E. N. Smith, T. L. Ho, and J. M. Parpia. Quantum phase transition of ^{3}He in aerogel at a nonzero pressure. *Phys. Rev. Lett.*, 79(2):253–256, 1997.

[100] A. J. Casey. *Two dimensional ^{3}He adsorbed on grafoil plated with a bilayer of HD*. PhD thesis, Royal Holloway University of London, 2001. Unpublished.

[101] O. V. Lounasmaa. *Experimental principles and methods below 1 K*. Academic Press, 1974.

[102] F. Pobell. *Mathers and methods at low temperatures*. Springer-Verlag, Berlin, 1992.

[103] G. K. White and P. J. Meeson. *Experimental techniques in low-temperature physics*. Oxford University Press, 2002.

[104] C. J. Gorter. Experiments on cooling of nuclear spins. *Phys. Z.*, 35:923, 1934.

[105] N. Kurti, F. N. Robinson, F. Simon, and D. A. Spohr. Nuclear cooling. *Nature (London)*, 178:450, 1956.

[106] V. V. Dmitriev, I. V. Kosarev, D. V. Ponanin, and R. Scheibel. Simple nuclear demagnetization stage. *Journal of Low Temperature Physics*, 113(5/6):945, 1009.

[107] R. C. Richardson and E. N. Smith. *Experimental techniques in condensed matter physics at low temperatures.* Addison-Wesley Publishing Company, Inc., 1988. Pg. 292.

[108] Model PLM-4, RV Elektroniikka Oy Picowatt, Vantaa, Finland.